NASA CONTRACTOR REPORT

AN EXPERIMENTAL STUDY OF ELECTRON TRANSMISSION AND BREMSSTRAHLUNG PRODUCTION

by D. H. Rester

Prepared by
LING-TEMCO-VOUGHT INC.
Dallas, Texas
for George C. Marshall Space Flight Center

NATIONAL AERONAUTICS AND SPACE ADMINISTRATION • WASHINGTON, D. C. • AUGUST 1969

AN EXPERIMENTAL STUDY OF ELECTRON TRANSMISSION AND BREMSSTRAHLUNG PRODUCTION

By D. H. Rester

Issued by Originator as Report No. 0-71100/9R-1

Prepared under Contract No. NAS 8-21055 by
LING-TEMCO-VOUGHT INC.
Dallas, Texas

for George C. Marshall Space Flight Center

NATIONAL AERONAUTICS AND SPACE ADMINISTRATION

For sale by the Clearinghouse for Federal Scientific and Technical Information
Springfield, Virginia 22151 – CFSTI price $3.00

PREFACE

The experiments described in this report are somewhat unrelated to each other; therefore, for the convenience of the reader the report has been divided into four parts. In Part I measurements of electron-bremsstrahlung cross sections at an incident electron energy of 50 keV with a Ge(Li) spectrometer are reported. Part II reports a determination of electron-electron bremsstrahlung yields from cross-section measurements on Be, for which the electron-electron component of the total bremsstrahlung yield is large. In Part III measurements of electron transmission of Al and Au targets for normal incidence of the electron beam at a bombarding energy of 2.5 MeV are described. Part IV includes studies of electron transmission for a cosine-law source and measurements of electron-bremsstrahlung production for non-normal incidence.

Reference is made to previously reported experiments published as NASA Contractor's Reports, in which experimental techniques have been described in detail. The early experiments included measurements of thick target bremsstrahlung production in the electron energy range from 0.2 to 2.8 MeV for materials ranging in atomic number from 13 to 79. Electron-bremsstrahlung cross sections have also been reported in the same energy range for materials representing a wide range of atomic numbers. Previous studies of electron transmission and backscattering for normal and non-normal incidence have also been published as NASA reports. The experiments reported in the present volume represent the final experimental efforts in this electron energy range. Collectively, the published experiments adequately describe the electron interactions in matter in the low to intermediate energy range considered to be of importance for comparison to computations of electron transport and bremsstrahlung production.

TABLE OF CONTENTS

PART I

MEASUREMENT OF ELECTRON-BREMSSTRAHLUNG CROSS SECTIONS FOR Al AND Au AT AN ELECTRON ENERGY OF 50 keV

MEASUREMENT OF ELECTRON-BREMSSTRAHLUNG CROSS SECTIONS FOR Al AND Au AT AN ELECTRON ENERGY OF 50 keV

INTRODUCTION

Measurements of electron-bremsstrahlung cross sections at an incident electron energy of 50 keV for targets of Al and Au have been reported by Motz.[1] The bremsstrahlung spectra reported in this previous study were obtained with a NaI scintillation spectrometer. The present experiment is similar to the experiment described by Motz. Bremsstrahlung production due to electrons of an incident energy of 50 keV bombarding targets of Al and Au was studied. However, in the present experiment a Ge(Li) spectrometer rather than a scintillation detector was used to measure the bremsstrahlung distributions. The resolution of the Ge(Li) spectrometer employed in the experiment was less than 1 keV below a photon energy of 50 keV and the response of the system was such that very little distortion of the continuous spectra was introduced by the measurement process. Therefore, it was not necessary to apply large correction factors to remove the effects of measurement even in the region near the endpoints of the spectra as is necessary when the measurements are made with a scintillation spectrometer. In addition, the Ge spectrometer allowed the measurements to be extended to lower photon energies, and in the case of the Au data the characteristic lines were resolved and the intensity of the underlying continuum was determined by removing the lines.

The experimental values of the cross section are compared to the cross sections computed by Kirkpatrick and Wiedmann,[2] using the theory of Sommerfeld, but corrected for relativistic effects as described in the article by Motz.[1] A complete discussion of the Sommerfeld theory and the relativistic correction applied to the values computed by Kirkpatrick and Wiedmann is given by Motz.

EXPERIMENTAL PROCEDURE

The 50-keV electron beam was obtained from a Cockcroft-Walton accelerator and directed to the target position of an aluminum scattering chamber. Precise positioning of the electron beam was achieved with three ZnS viewing screens which could be positioned remotely into and out of the beam. Adequate magnetic shielding of the accelerator tube and scattering chamber was provided to insure that the beam path was linear, i.e., not visibly deflected by stray magnetic fields.

Pulse height distributions were obtained with a Ge(Li) spectrometer. The Ge detector was of the planar type, 5 mm in thickness and 10 mm in diameter. The entrance window to the spectrometer system consisted of a 0.125 mm thick Be foil. The exit window of the vacuum chamber in which the target was positioned consisted of a single layer of 0.125 mm thick mylar. The observed photon flux was collimated outside the vacuum chamber by a precision collimator system which could be rotated at fixed radius around the axis of the chamber. The collimator aperture defining the experimental solid angle of the spectrometer was 4 mm in diameter. The solid angle thus defined was adequate to obtain a useable count rate for an incident electron beam of 10^{-9} to 10^{-8} A. On the other hand, it was small enough to prevent the incident photons from interacting near the edge of the Ge crystal, where photo electrons might escape the crystal. Electrons which escape contribute to the region of the response below full energy absorption, thereby complicating the response of the spectrometer.

The characteristics of the spectrometer were determined from measurements with radioactive sources and with beam-produced activities. A Hg^{203} source provided an adequate number of x-ray lines to establish the energy calibration of the system. The K_α and K_β lines were well resolved, as were lines due to transitions from the M and N shells to the L-shell vacancies created by internal conversion. The

actual response of the spectrometer was obtained by use of a LiF crystal x-ray diffraction system, which served as a monochromator. The source for the diffraction system was a continuous bremsstrahlung flux produced by bombarding a thick Fe target. The monochromator provided lines in the photon energy region from 10 keV to 50 keV. Measurements of lines in this region with the Ge(Li) spectrometer demonstrated that the response of the system to a monochromatic source is largely Gaussian from full energy absorption. The portion of the response represented by less than full energy events was found to be only a few percent of the total. The response resulted in negligible distortion of the continuous spectra observed in the present experiment.

Correction curves for photon absorption in the mylar window of the vacuum chamber and the Be window of spectrometer were determined experimentally as a function of photon energy. Additional pieces of both materials, equivalent to the thicknesses used in the experimental arrangement, were positioned in the photon flux from a thick target bombarded by the beam. Measurements with and without the additional materials were used to derive the attenuation coefficients. Attenuation in the air path of 5 cm between the mylar chamber window and the Be foil of the spectrometer was calculated for the photon energy region greater than 10 keV. Below this energy the effect of attenuation was estimated by extending the computed values above 10 keV with a shape similar to the shapes determined for mylar and Be.

Self-supporting Al targets of thicknesses of about 20 $\mu g/cm^2$ were used in the experiment. These were made by the vacuum evaporation technique and were essentially hole-free over the beam spot region. Au targets of about 20-$\mu g/cm^2$ thicknesses were evaporated on VYNS backings of 5 $\mu g/cm^2$. Target thickness determinations were made in the case of Al by measurements of Mott scattering at 200 keV incident electron energy, and by direct weighing of known areas of the foils. Thickness determination of the Au targets were made by measurements of the Mott scattering cross sections at 200 keV.

EXPERIMENTAL RESULTS

Pulse height distributions due to detection of the bremsstrahlung emitted by electrons of incident energy of 50 keV scattered by Al and Au targets were obtained with a Ge(Li) spectrometer. A previous experiment which reported similar measurements on Al and Au targets at 50 keV incident energy was reported by Motz.[1] The earlier experimental measurement was made with a NaI scintillation detector. NaI spectrometers characteristically have resolutions at 50 keV of 25-30%. The effect of resolution of this order is that the measured continuous spectra, over the photon energy interval from 10-50 keV, suffer large distortions which must be removed before accurate cross-section values can be obtained. In principle this can be done, but the accuracy of the corrected spectra is in question where large corrections are made. Furthermore, the particular corrections required vary with the shape of the incident photon distribution, which in turn depend on the target material and the angle of photon emission. Only if the detected shape is constant are the correction factors constant. The use of a Ge(Li) spectrometer of the type employed in the present experiment eliminates the necessity of applying large response corrections to the pulse height distributions. The resolution of the system in the photon energy region below 50 keV was less than 1 keV. The full energy absorption efficiency was nearly 100% from 50 keV down to 20 keV, where attenuation in the windows became detectable. A correction for attenuation in both windows of 10% was required at a photon energy of 10 keV. Measurements are reported down to 6 keV where correction of a factor of two due to attenuation was made. The uncertainty in the correction factors below this energy is quite large. Corrections applied to pulse height distributions taken with a scintillation detector, on the other hand, are about a factor of 1.8 at the 50-keV end point to compensate for response distortion. At the low energy end, corrections for attenuation and response are required which are comparable. Only in the mid-spectrum region is the correction small.

The experimental values from the present measurements at angles less than 90 deg are shown in Fig. 1 for Al and in Fig. 2 for Au. The values are normalized to the Sommerfeld theory, computed by Kirkpatrick and Wiedmann,[2] but corrected for relativistic effects in the manner indicated in the article by Motz.[1] The values used to normalize the measurements can be obtained by evaluating eq 5. 8-9 of the article by Kirkpatrick and Wiedmann[2] and correcting by the relativistic correction factor $(1-\beta_o \cos\theta)^{-2}$.

The solid circles in Figs. 1-2 are points taken from the article by Motz.[1] In Fig. 1 at 20 and 60 deg for Al the two experiments are in good agreement. The trends of the data as a function of angle are similar for both experiments, so that for Al the experiments are well within the quoted experimental errors from 10 keV to 50 keV photon energy. For Au, Fig. 2, it is seen that the comparison of the two experiments can be made only in the photon region above 30 keV, because of the interference in the scintillation data from the discrete lines due to L-shell ionization at lower photon energy. In the region from 30 to 50 keV photon energy the two experiments are in agreement.

Below 30 keV in the spectra obtained with the Ge spectrometer the lines due to transitions of significant intensity from M,N and higher shells to L-shell vacancies which were unresolved in the scintillation data are resolved from the underlying continuum. The values in Fig. 2 from the present experiment in the photon energy region from 6 to 15 keV were obtained by stripping the lines from the spectra. The cross-section values measured at 20, 30, 45, and 60 deg in this region and in the region up to 50 keV are given in Table I for Al and Table II for Au.

The experimental cross sections, differential in energy and solid angle, at an emission angle of 120 deg are shown in Fig. 3. In this figure the line spectrum was not removed so that the prominence of the lines compared with the continuum could be seen. The

yield represented by the line spectrum gives a cross section of 2.65×10^{1} barns/sr or 3.35×10^{2} barns after integration over angle. The measurements at other angles verified that the lines are isotropic in intensity as expected. The cross section for ionization of the L-shell cannot be obtained until the correction for other decay modes are known.

Errors in the experimental values of the present experiment are estimated to total $\pm$ 5% in the photon region above 10 keV. Below 10 keV additional error arises because of corrections for absorption in the Be and mylar windows and in air. At 6 keV the estimated error is 25%. The values taken from the paper of Motz are assigned an error of about 10% by him, but as shown in the figure additional error may have been introduced in determining the values from the original paper.

REFERENCES

1. J. W. Motz and R. C. Placious, Phys. Rev. 109, 235(1958).

2. P. Kirkpatrick and L. Wiedmann, Phys. Rev. 67, 321(1945).

TABLE I

Experimental Electron-Bremsstrahlung Cross Sections for Al at T_o = 50 keV in barns per steradian - MeV

k(keV)	θ = 20°	θ = 30°	θ = 45°	θ = 60°
6	1.83(2)	1.48(2)	1.22(2)	1.89(2)
8	1.77(2)	1.48(2)	1.20(2)	1.38(2)
10	1.44(2)	1.24(2)	1.04(2)	9.40(1)
12	9.58(1)	8.82(1)	7.61(1)	6.20(1)
14	7.88(1)	6.99(1)	6.26(1)	5.55(1)
16	6.62(1)	6.30(1)	5.37(1)	4.81(1)
18	5.38(1)	5.33(1)	4.84(1)	4.21(1)
20	4.57(1)	4.51(1)	4.40(1)	3.66(1)
22	4.10(1)	4.09(1)	3.83(1)	3.42(1)
24	3.55(1)	3.44(1)	3.48(1)	2.98(1)
26	2.90(1)	3.04(1)	3.07(1)	2.84(1)
28	2.53(1)	2.81(1)	2.78(1)	2.50(1)
30	2.32(1)	2.41(1)	2.48(1)	2.35(1)
32	1.92(1)	2.13(1)	2.37(1)	2.09(1)
34	1.65(1)	1.87(1)	2.17(1)	2.09(1)
36	1.52(1)	1.75(1)	1.85(1)	1.82(1)
38	1.25(1)	1.66(1)	1.81(1)	1.62(1)
40	1.05(1)	1.42(1)	1.71(1)	1.48(1)
42	9.10(0)	1.30(1)	1.51(1)	1.39(1)
44	8.00(0)	1.07(1)	1.38(1)	1.32(1)
46	7.00(0)	1.00(1)	1.30(1)	1.29(1)
48	5.40(0)	9.60(0)	1.14(1)	1.17(1)
50	4.55(0)	8.84(0)	1.10(1)	1.04(1)

TABLE II

Experimental Electron-Bremsstrahlung Cross Sections for Au at T_o = 50 keV in barns per steradian - MeV

k(keV)	θ = 20°	θ = 30°	θ = 45°	θ = 60°
6	6.40(3)	5.63(3)	5.19(3)	4.85(3)
8	4.24(3)	3.91(3)	3.44(3)	3.40(3)
10	2.95(3)	2.88(3)	2.72(3)	2.67(3)
12	2.31(3)	2.32(3)	2.16(3)	2.12(3)
14	1.88(3)	2.00(3)	1.84(3)	1.80(3)
16	1.65(3)	1.69(3)	1.68(3)	1.65(3)
18	1.45(3)	1.51(3)	1.54(3)	1.45(3)
20	1.33(3)	1.35(3)	1.43(3)	1.33(3)
22	1.17(3)	1.25(3)	1.28(3)	1.22(3)
24	1.04(3)	1.10(3)	1.21(3)	1.11(3)
26	9.35(2)	1.01(3)	1.14(3)	1.03(3)
28	8.70(2)	9.25(2)	1.02(3)	9.65(2)
30	7.90(2)	8.55(2)	9.81(2)	9.25(2)
32	7.25(2)	7.88(2)	9.10(2)	8.21(2)
34	6.61(2)	7.42(2)	7.68(2)	7.68(2)
36	5.97(2)	6.64(2)	7.40(2)	7.42(2)
38	5.54(2)	6.66(2)	7.00(2)	6.78(2)
40	5.24(2)	6.15(2)	6.77(2)	6.45(2)
42	4.82(2)	5.61(2)	6.40(2)	6.01(2)
44	4.42(2)	5.19(2)	5.92(2)	5.47(2)
46	4.30(2)	4.76(2)	5.87(2)	5.10(2)
48	3.62(2)	4.30(2)	5.42(2)	4.53(2)
50	3.04(2)	4.00(2)	4.82(2)	4.00(2)

FIGURE CAPTIONS

Fig. 1 Normalized differential cross sections for electron-bremsstrahlung production by Al at an incident electron energy of 0.05 MeV.

Fig. 2 Normalized differential cross sections for electron-bremsstrahlung production by Au at an incident electron energy of 0.05 MeV.

Fig. 3 Comparison of measured and theoretical differential cross sections at 120° for Au (top) and Al (bottom). Prominent line structure is seen in the Au spectrum due to ionization of the L-shell of the atom.

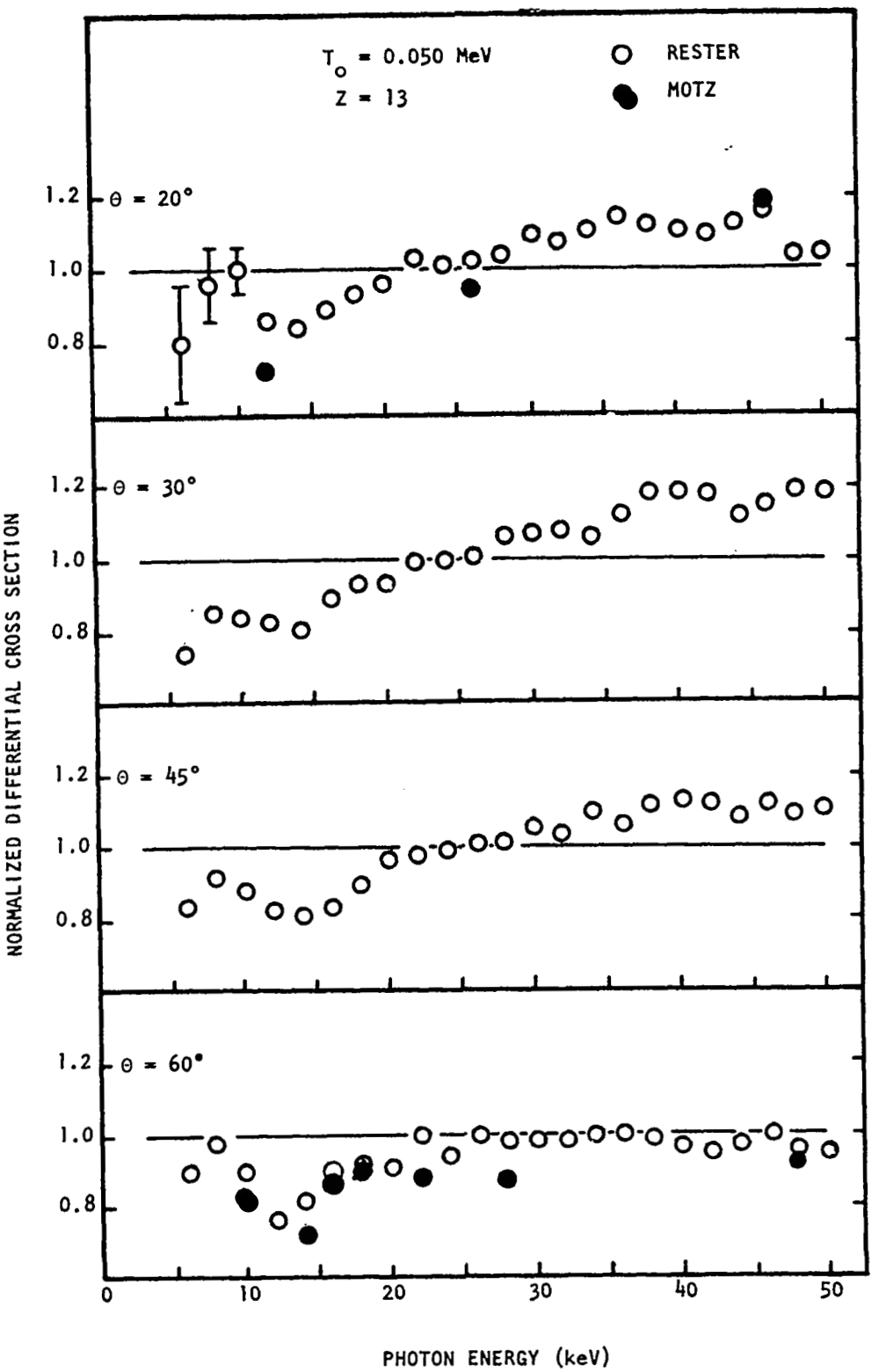
T_o = 0.050 MeV
Z = 13
RESTER
MOTZ
θ = 20°
θ = 30°
θ = 45°
θ = 60°
1.2
1.0
0.8
0
10
20
30
40
50
NORMALIZED DIFFERENTIAL CROSS SECTION
PHOTON ENERGY (keV)

FIGURE 1.

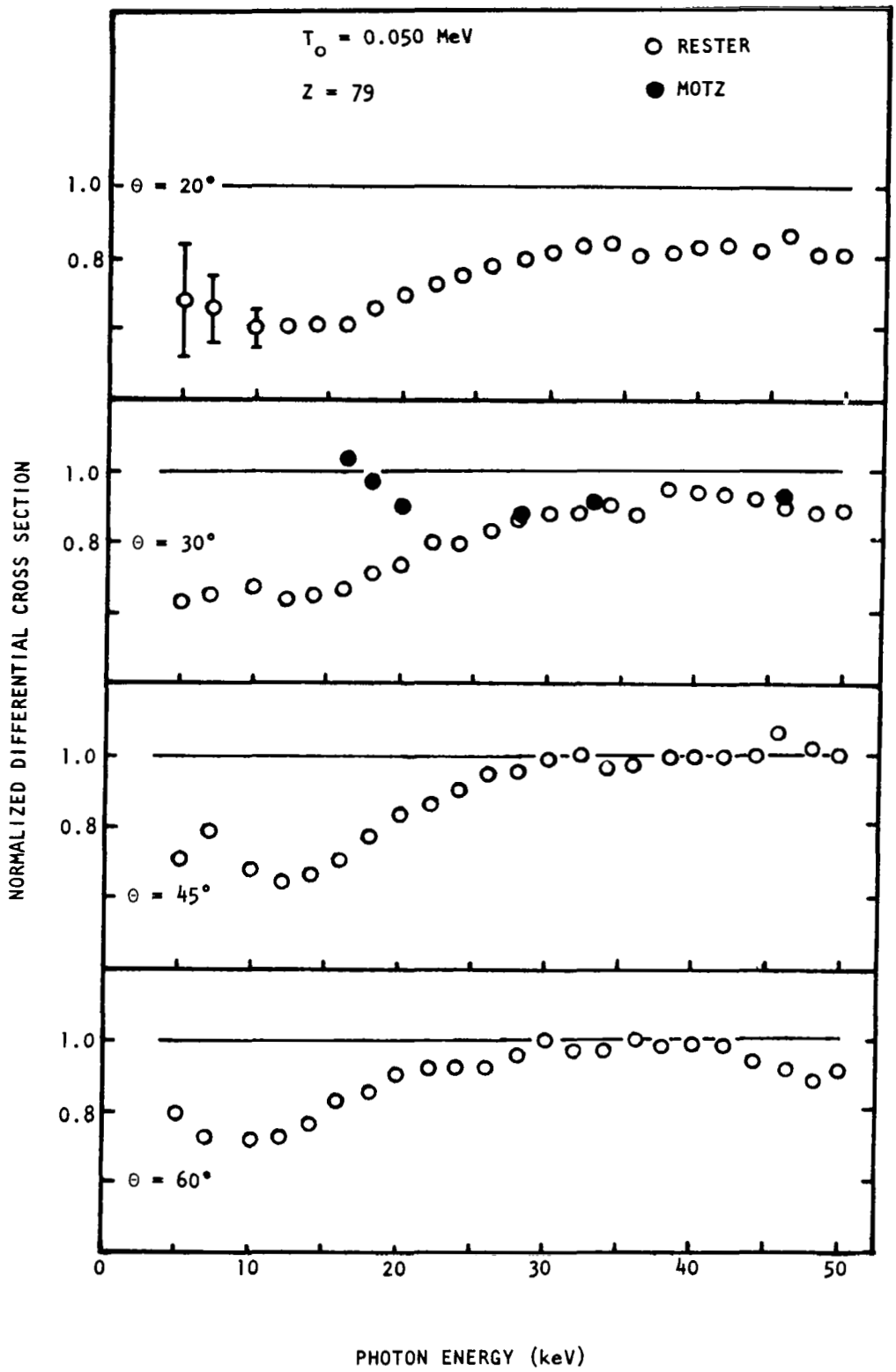
T_o = 0.050 MeV
Z = 79
RESTER
MOTZ
1.0
0.8
Θ = 20°
Θ = 30°
Θ = 45°
Θ = 60°
0
10
20
30
40
50
NORMALIZED DIFFERENTIAL CROSS SECTION
PHOTON ENERGY (keV)

FIGURE 2

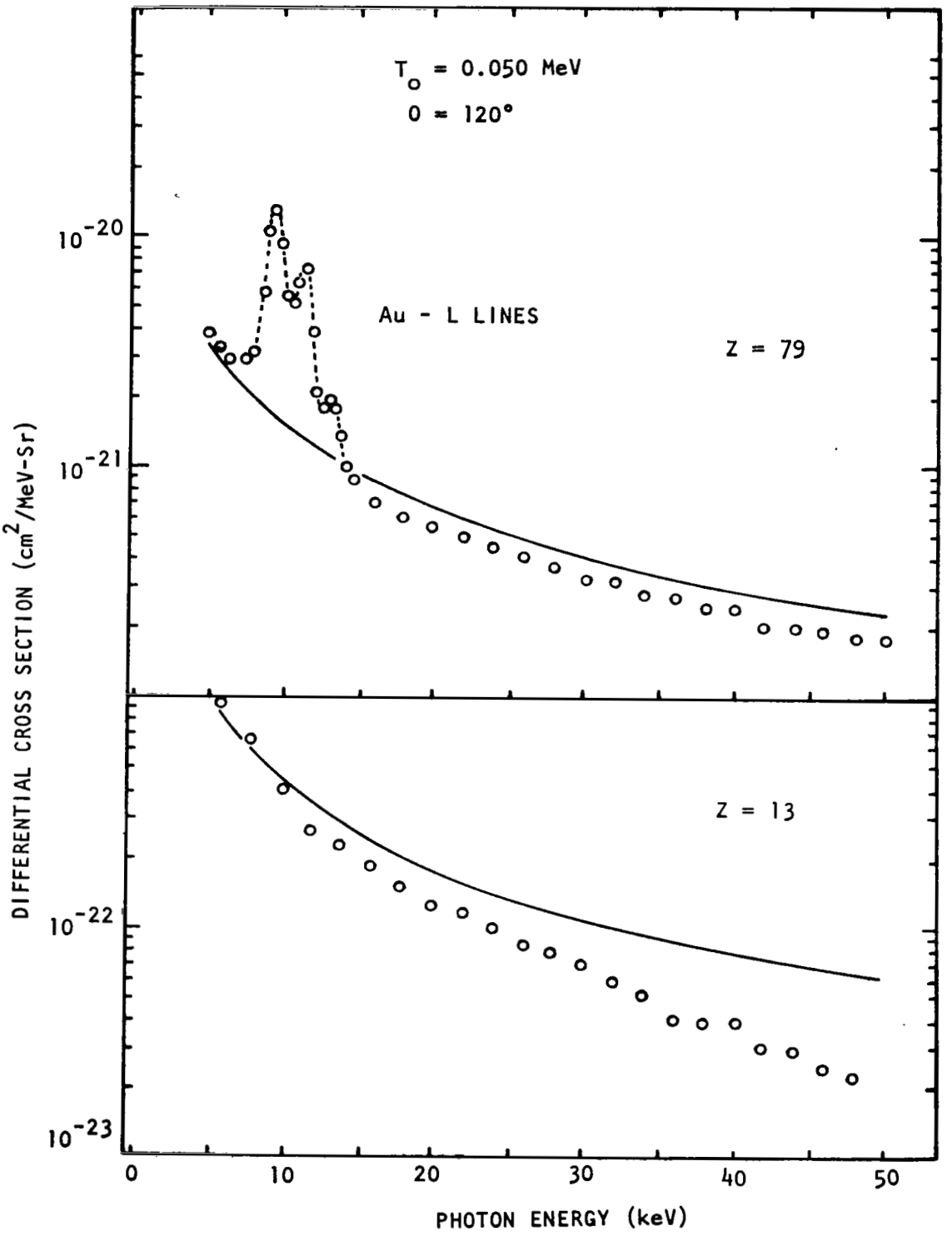
T_o = 0.050 MeV
θ = 120°
Au - L LINES
Z = 79
Z = 13
10^{-20}
10^{-21}
10^{-22}
10^{-23}
DIFFERENTIAL CROSS SECTION (cm^2/MeV-Sr)
0
10
20
30
40
50
PHOTON ENERGY (keV)

FIGURE 3

PART II

BREMSSTRAHLUNG CROSS-SECTION MEASUREMENTS ON Be AT INCIDENT ELECTRON ENERGIES OF 1.0 AND 2.0 MeV

BREMSSTRAHLUNG CROSS-SECTION MEASUREMENTS ON Be AT INCIDENT ELECTRON ENERGIES OF 1.0 AND 2.0 MeV

INTRODUCTION

Cross sections for production of bremsstrahlung due to electron bombardment of Al, Cu, Sn, and Au targets at 0.2, 1.0, 1.7, and 2.5 MeV incident electron energies have been previously reported.[1,2] Similar measurements at 2.72, 4.54, and 9.66 MeV were reported on Be, Al, and Au by Starfelt and Koch.[3] The results of the two experiments are compatible and provide cross-section values for a wide range of incident electron energies. They are particularly important since they provide the only available accurate values for the cross sections in this energy region. The data which has been reported, however, does not unambiguously differentiate between the bremsstrahlung production due to electron scattering in the nuclear charge field and that due to electron scattering in the orbital electron field.

Electron-bremsstrahlung production cross sections due to interactions of the electron with the charge of the nucleus are derived by the Born-approximation method in this electron energy range. They are not generally accurate for all photon energies and atomic numbers. Exact calculations of electron-electron bremsstrahlung cross sections are also quite complex; therefore, they have not been carried out. Cross-section formulas for the nuclear charge interaction for heavy elements, where the contribution due to the atomic electrons is expected to be relatively small, are usually corrected to account for the electron-electron component by replacing Z^2 by $(Z^2 + Z)$. For the light elements, on the other hand, the contribution is significantly large compared to the nuclear charge component and this simple correction is not adequate.

This section of the report describes the measurements of the bremsstrahlung cross sections due to bombardment of a Be target with 1.0 and 2.0-MeV electrons and the identification of the electron-electron portions of the total spectra. The predicted contribution of the electron-electron component due to all four atomic electrons to the total spectrum is about 20%. This is a large enough contribution that an accurate determination of the effect can be made with the same experimental system as was used for the previous measurements. Measurements on Be are reported at 0, 10, 20, 30, and 45 deg at 1.0 MeV incident electron energy and at 0, 10, and 20 deg at 2.0 MeV.

At each incident electron energy the electron-electron bremsstrahlung spectrum is distributed up to a maximum value less than the incident energy, but dependent on the angle of observation. To isolate the contribution of the electron-electron component, the experimental cross sections are normalized to values which represent the bremsstrahlung due to the interaction of the incident electron and the nuclear charge. In the region of the spectrum where the electron-electron bremsstrahlung yield is detectable, the normalized value is greater than one but should drop to the value one at, or near, the end-point. There are effects discussed below, which limit the accuracy of determining the end-point energy. The end-point values can be determined theoretically from kinematic considerations and reasonable agreement of the experiment with the predicted values is expected.

The results of this experiment have been published in Nuclear Physics.[4]

EXPERIMENTAL PROCEDURE

The experimental procedure and the method of data reduction used in the present experiment are the same as that used in earlier work and described in a previous report.[2] The problem of statistical accuracy of the data in the photon energy region near the incident electron energy, which was a serious problem in the previous measurements on other targets, was even more serious for the measurements on the 1.86-mg/cm^2 Be target of the present experiment. To improve the statistical accuracy, two spectra were run for each data point. The first measurement was made with the spectrometer viewing the target with the photon flux transmitting only the 5-mil mylar chamber window and the air path to the detector. The second, however, was made with an attenuator, or beam hardener, inserted between the target and the detector. The attenuator thickness was chosen to reduce the count rate at 75% of the high-energy limit by 10-15%, but to reduce the count rate due to the portion of the spectrum below this energy by several orders of magnitude. Increased beam current was used for the runs with the attenuator to obtain good statistical accuracy without spectral distortion from pulse pile-up. The end-point values are of particular interest generally, but they are of increased importance in the case of the Be measurements because of the desirability of pinpointing the electron-electron bremsstrahlung end-points, also in this region. Each spectrum in Figs. 1-2 is a composite of a spectrum taken without the attenuator and a spectrum taken with the attenuator, but corrected for absorption. The joining energies for the pairs of spectra are 0.75 and 1.5 MeV for the 1.0 and 2.0 MeV incident energies.

EXPERIMENTAL ERRORS

The experimental errors associated with the measurement of a continuous spectrum can be conveniently separated into two categories. Errors which fall into the first category produce a distortion of the spectrum. Errors of the second type uniformily affect the entire spectrum. The errors of the first type in the present case vary with the incident energy and with the angle at each incident energy. They are:

(1) Error in the angle of photon emission of ȯ.3 deg. Little uncertainty is introduced by this error at 0 deg at both energies. At 1.0 MeV at larger angles this angular uncertainty results in an error of 6%. At 2.0 MeV, 10%.

(2) Statistical uncertainty. Statistical uncertainty is greatest in the photon energy region near the spectral end points. At 0 deg the uncertainty is less than 3% for photon energies less than 80% of the end point. At the largest angles the uncertainty is estimated to be less than 6% below 50% of the end point.

(3) Error from spectrometer response removal. The error after corrections for spectrometer response from incomplete response removal is estimated to be less than 3% for photon energies less than 80% of the end point. In the region above 80% of the end point the error increases to a maximum of 30% at the end-point energy.

(4) Error in background removal. Spectral distortion due to background removal is estimated to be less than 1% below photon energies of 2.0 MeV.

Errors which fall into the second category include $\pm$ 2% for beam current integration and $\pm$ 2% for target thickness and uniformity.

DISCUSSION OF RESULTS

At 1.0 MeV for Al targets, the previously reported measurements showed discrepancies when compared to the unscreened Born-approximation values which were less than 10%, except near the end-point where the approximation is not valid and at low photon energies where departures from the theory were ascribed to the effect of screening of the nuclear charge by the atomic electrons. A reduction in yield by about 20-30% due to screening was observed at forward angles. At 1.7 MeV the measured cross sections for Al were quite close to the theory except in the low and high photon energy regions, as expected. The measurements on the Be target at 1.0 and 2.0 MeV incident energy are shown in Figs. 1-2. The Born-approximation theory is given in the figure as solid lines for comparison to the experiment. The experimental values appear to be considerably above the theory in the photon energy region between 30% and 70% of the end-point energies, which is the photon energy region where good agreement is expected and was observed for Al. The increase in the cross sections above the Born-approximation values apparent in the plots is due to a significant admixture of electron-electron bremsstrahlung.

The ratio of the reduced cross sections of Be and Al at 1.0 MeV incident energy at angles of 0, 10, 20, and 30 deg are shown in Fig. 3. Normalization of the Be cross sections by use of the Al values rather than the Born-approximation values at 1.0 MeV is desirable since the Al cross-section values are more characteristic of the actual nuclear charge part of the spectra than the unscreened Born-approximation cross sections. They include the effect of screening and the Coulomb effect, although to a somewhat greater degree than is expected for Be. The maximum photon energies of the electron-electron bremsstrahlung for emission angles of 0, 10, 20, and 30 deg are 0.852, 0.822, 0.745, and 0.646 MeV, respectively. These values are indicated by arrows in Fig. 3. Within the experi-

mental uncertainty, the ratios show an enhancement below the predicted values of the end-point energies because of the electron-electron contribution. Above these energies the ratios drop below 1.0 rather than to 1.0 due to the relatively larger Coulomb effect for Al. The data for Al was obtained at the same time as the data for Be by remotely interchanging the Al and Be targets. The experimental errors described above due to response removal, background removal, and angular uncertainty essentially do not apply to the ratio values. Fluctuations due to statistical accuracy, however, tend to smear the electron-electron bremsstrahlung end-point. In addition, the difference in the Coulomb effect for the two elements shifts the point where the ratio is 1.0 to slightly lower photon energy. Nevertheless, the experimental end-points are discernible and in agreement with the predictions of the kinematics.

At 2.0 MeV the measured Be cross sections, normalized to the unscreened Born-approximation values, are shown in Fig. 4. At this energy the Born approximation is accurate for most photon energies for low atomic numbers. The predicted end-points of the electron-electron bremsstrahlung spectra for 0, 10, and 20 deg are 1.814, 1.701, and 1.436 MeV. These values are indicated by the arrows in Fig. 4. As at 1.0 MeV the measured end-points agree with the predictions within the estimated accuracy of the experimental determinations. At both energies the maximum enhancement due to the electron-electron component appears to be about 30% of the value of the electron-nucleus bremsstrahlung. At 2.0 MeV incident energy the normalized values at low photon energy also cross the value 1.0. This is not a real effect but occurs because the theory without screening over-predicts the nuclear charge component of the spectrum in the low photon energy region. A comparison at 2.0 MeV of the reduced cross sections at 0 deg for Al and Be, similar to those at 1.0 MeV is shown in Fig. 5. The values are close to those in Fig. 4 for 0 deg, except the ratio goes considerably below 1.0 above the electron-electron bremsstrahlung end-point and it continues to increase at low photon energy with decreasing energy.

Previous measurements in this energy range on Be have been reported by Motz[5] and by Starfelt and Koch.[3] The measurements of Starfelt and Koch on Al and Au agree with previous measurements by the present author. Those of Motz do not; therefore, his measurements are not considered here. On the other hand, the data of Starfelt and Koch on Be at 2.72 MeV is inconclusive due to rather large fluctuations of the data-points, presumably as a result of poor statistics. Their results do indicate the presence of electron-electron bremsstrahlung inasmuch as they average significantly above the Born-approximation theory. However, a determination of the end-points and the cross sections is not possible from their data due to the fluctuations.

REFERENCES

1. D. H. Rester and W. E. Dance, Phys. Rev. 161, 85(1967).
2. W. E. Dance, W. J. Rainwater, Jr., and D. H. Rester, "Investigation of Electron Interaction in Matter", NASA CR-1194, October 1968.
3. N. Starfelt and H. W. Koch, Phys. Rev. 102, 1598(1956).
4. D. H. Rester, Nucl. Phys. A118, 129(1968).
5. J. W. Motz, Phys. Rev. 100, 1560(1955).

FIGURE CAPTIONS

Fig. 1 Comparisons of experimental electron-bremsstrahlung cross sections to the Born-approximation values for an unscreened Be nucleus at 1.0 MeV bombarding energy. Experimental values in the mid-spectrum region exceed the theoretical estimates significantly, indicating an enhancement of yield due to electron-electron interactions.

Fig. 2 Comparisons of experimental electron-bremsstrahlung cross sections to the Born-approximation values for an unscreened Be nucleus at 2.0 MeV bombarding energy. As at 1.0 MeV bombarding energy, the experimental values exceed the predicted values.

Fig. 3 Reduced cross sections due to electron bombardment of a Be target at 1.0 MeV divided by the reduced cross sections for Al. Both sets of values are experimental. Spectra at each angle were obtained for each target without otherwise changing the experimental arrangement, thereby reducing experimental error as discussed in the text. The arrows indicate the energies predicted from kinematics for the electron-electron bremsstrahlung end-points.

Fig. 4 Experimental cross sections at 2.0 MeV incident energy, normalized to the unscreened Born-approximation values for Be. The arrows indicate the predicted energies of the electron-electron bremsstrahlung end-points.

Fig. 5 Ratio of the reduced cross sections of Be and Al at 0 deg for 2.0 MeV bombarding energy. The shape in the low photon energy region differs from the shape in Fig. 4 at this angle, because the reduced cross section for Al, in effect, includes a screening correction. At high photon energy the ratio crosses the value 1.0 because of the larger Coulomb effect for $Z = 13$.

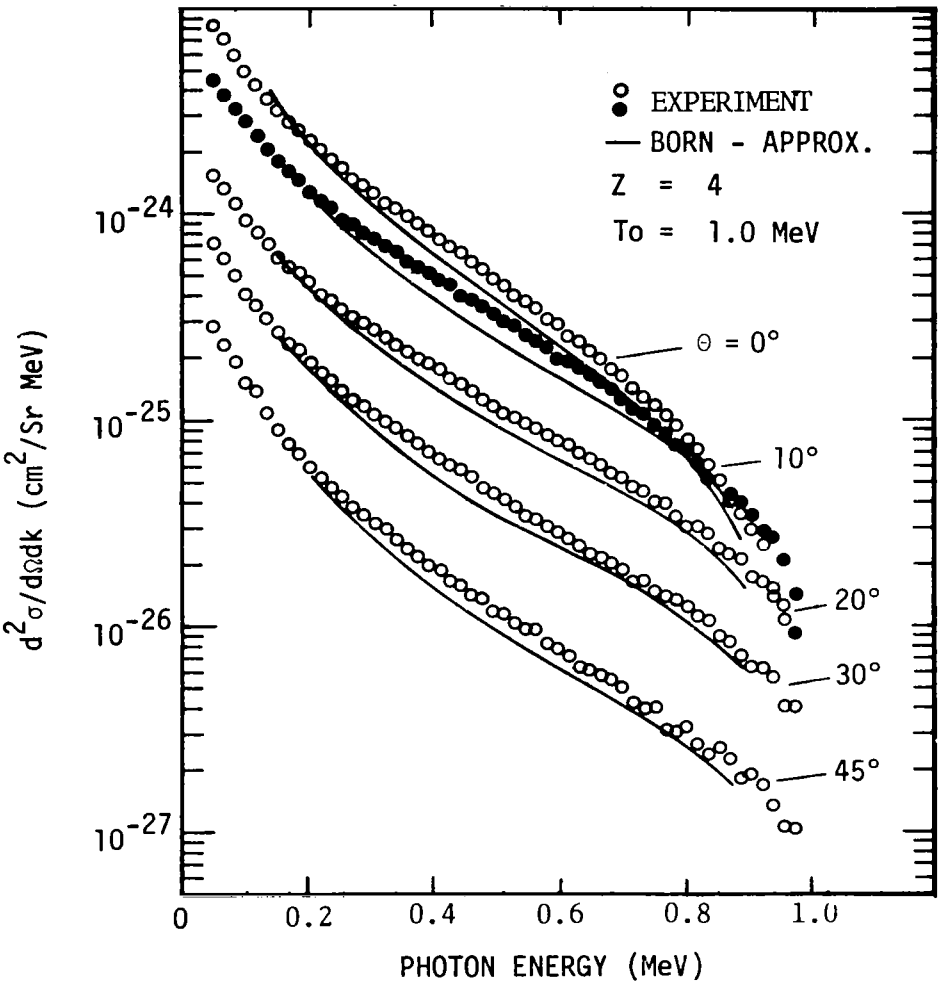
EXPERIMENT
BORN - APPROX.
Z = 4
To = 1.0 MeV
Θ = 0°
10°
20°
30°
45°
10^{-24}
10^{-25}
10^{-26}
10^{-27}
$d^2\sigma/d\Omega dk$ (cm^2/Sr MeV)
0
0.2
0.4
0.6
0.8
1.0
PHOTON ENERGY (MeV)

FIGURE 1

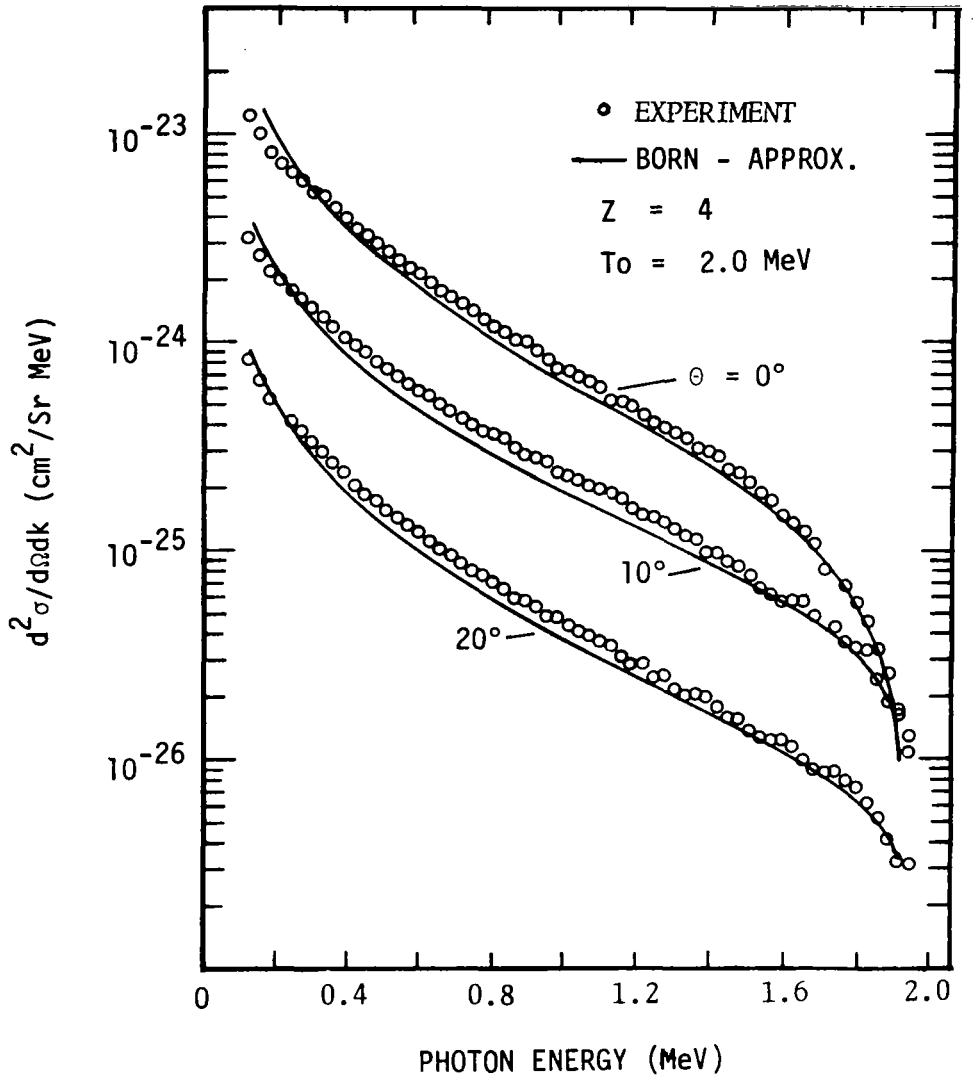
EXPERIMENT
BORN - APPROX.
Z = 4
To = 2.0 MeV
Θ = 0°
10°
20°
10^{-23}
10^{-24}
10^{-25}
10^{-26}
$d^2\sigma/d\Omega dk$ (cm^2/Sr MeV)
0
0.4
0.8
1.2
1.6
2.0
PHOTON ENERGY (MeV)

FIGURE 2

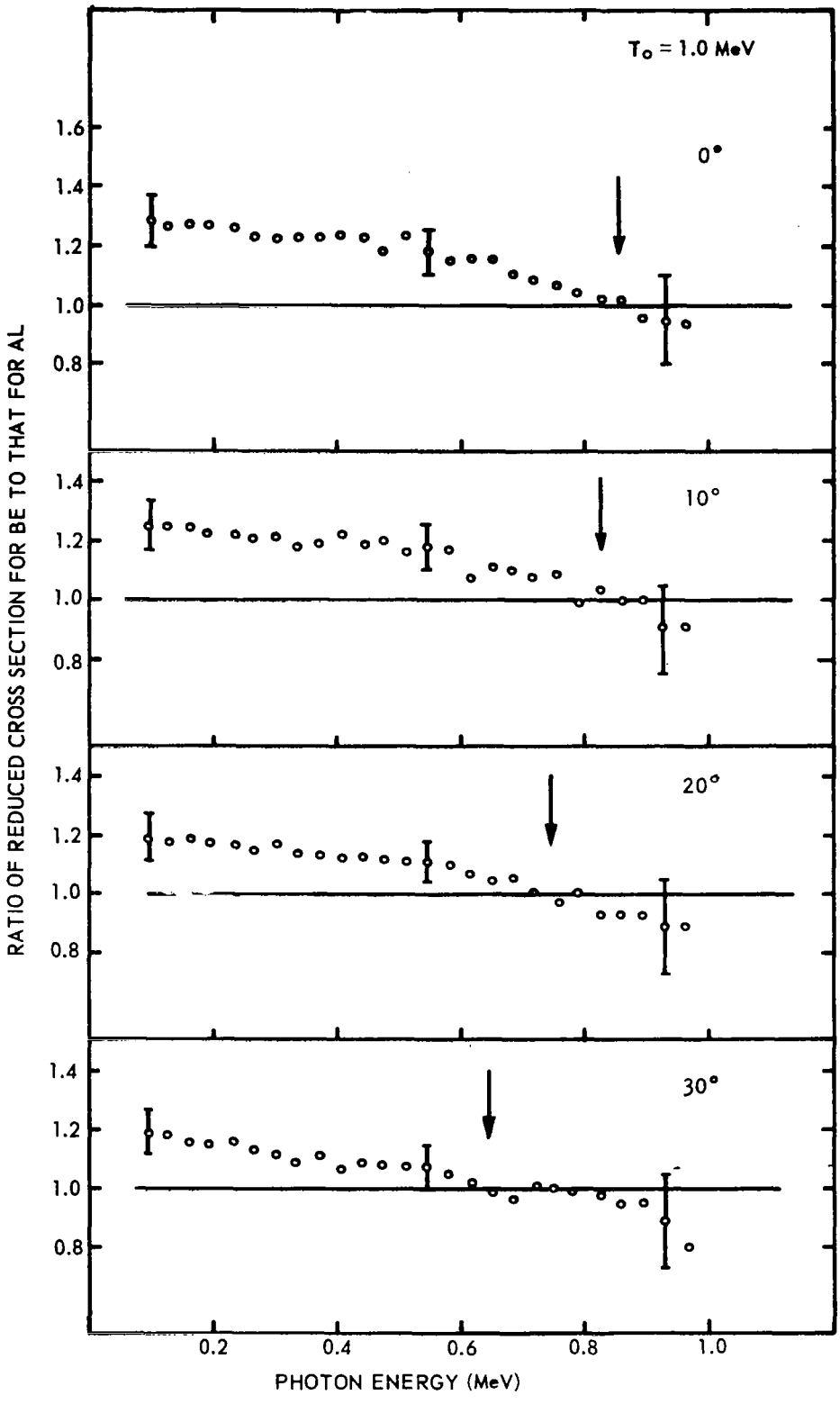
T_o = 1.0 MeV
0°
10°
20°
30°
1.6
1.4
1.2
1.0
0.8
0.2
0.4
0.6
0.8
1.0
RATIO OF REDUCED CROSS SECTION FOR BE TO THAT FOR AL
PHOTON ENERGY (MeV)

FIGURE 3

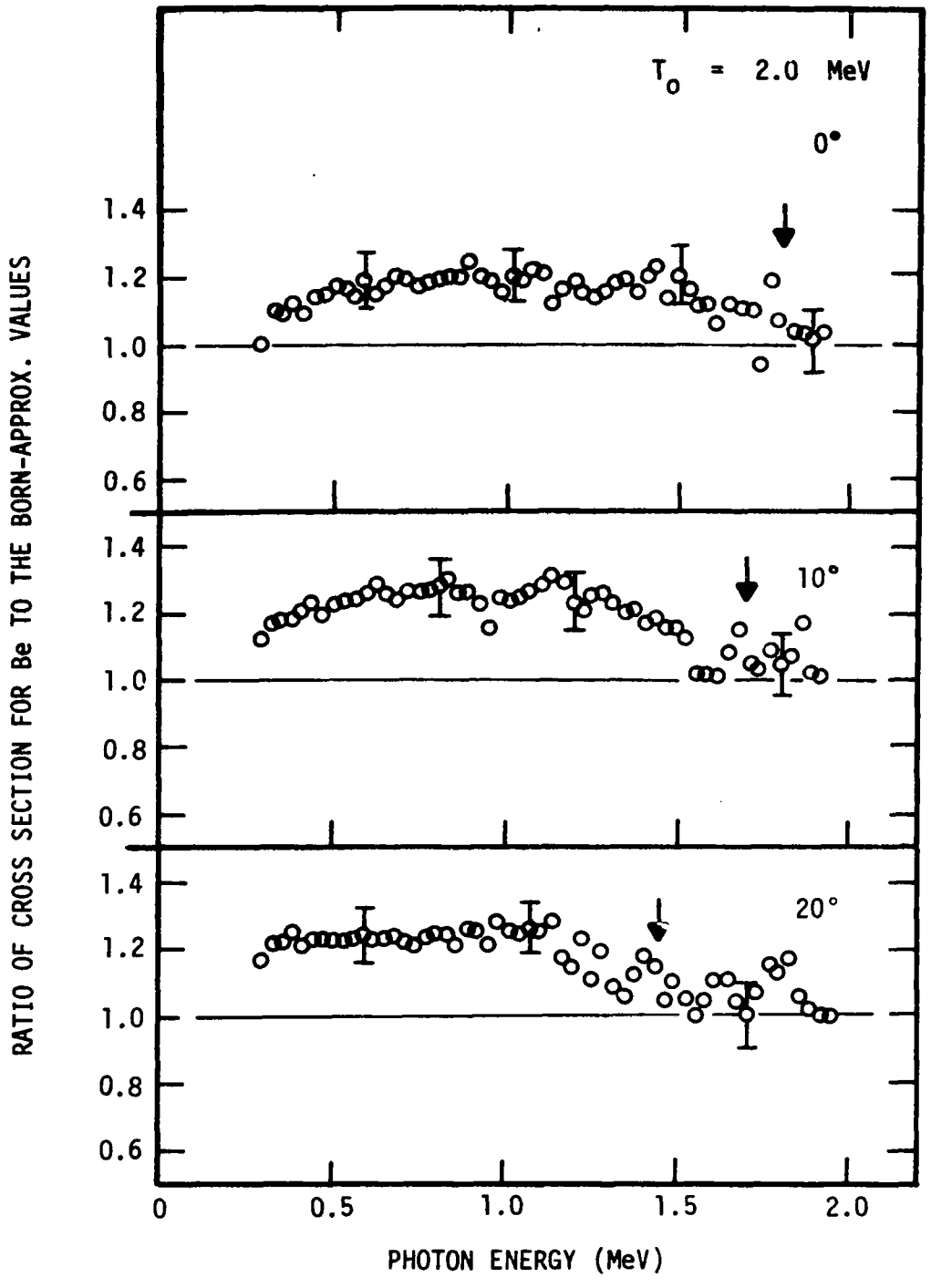
T_o = 2.0 MeV
0°
10°
20°
1.4
1.2
1.0
0.8
0.6
0
0.5
1.0
1.5
2.0
PHOTON ENERGY (MeV)
RATIO OF CROSS SECTION FOR Be TO THE BORN-APPROX. VALUES

FIGURE 4

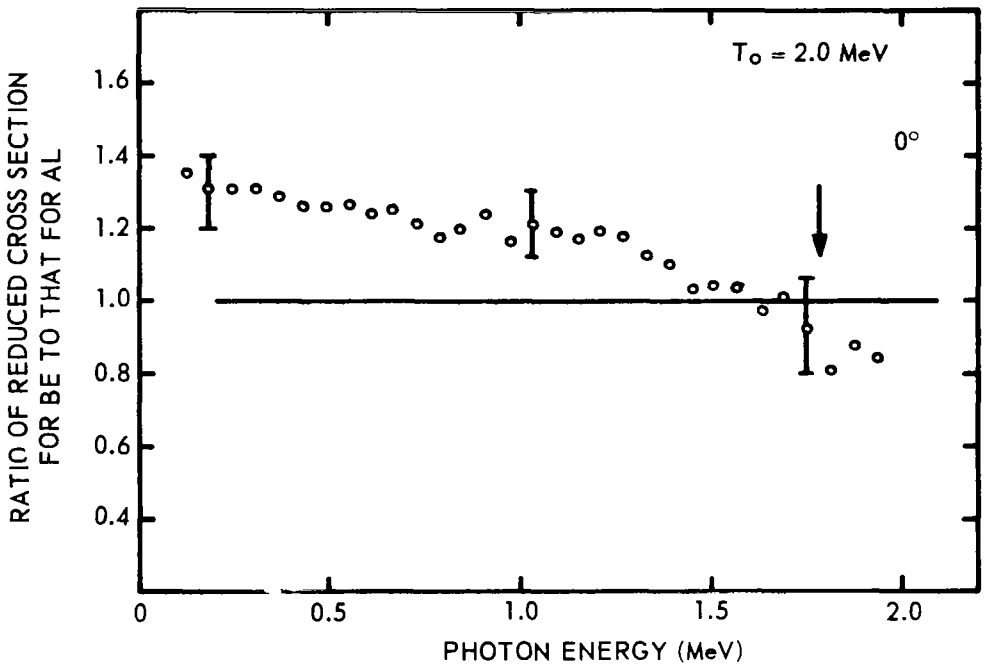
T_o = 2.0 MeV
0°
RATIO OF REDUCED CROSS SECTION FOR BE TO THAT FOR AL
1.6
1.4
1.2
1.0
0.8
0.6
0.4
0
0.5
1.0
1.5
2.0
PHOTON ENERGY (MeV)

FIGURE 5

PART III

ELECTRON TRANSMISSION OF Al AND Au TARGETS FOR AN INCIDENT ELECTRON ENERGY OF 2.5 MeV

ELECTRON TRANSMISSION OF Al AND Au TARGETS FOR AN INCIDENT ELECTRON ENERGY OF 2.5 MeV

INTRODUCTION

Previous measurements of electron penetration of Al and Au targets for normal incidence of a 1.0-MeV electron beam were reported in NASA Contractor's Reports, NASA CR 334[1] and 759.[2] The data consisted of energy distributions of transmitted electrons as a function of angle with respect to the direction of the incident particle beam. From the data a total transmission spectrum was constructed for each target. Angular distributions of the number of transmitted particles integrated over energy and the transmitted fractions of the incident beam were also derived. In the case of the Al targets comparisons for three thicknesses, corresponding to 0.2, 0.4, and 0.6 the range in Al at 1.0 MeV, were made to the Monte Carlo spectra of M. J. Berger. The comparisons showed good agreement for the two thickest targets, but a somewhat less satisfactory comparison was observed for the thinnest target. No comparisons were made between experiment and computation for the case of electron diffusion in Au.

The more recent experiments described here are measurements similar to those reported earlier, but at an incident electron energy of 2.5 MeV. Target thicknesses of Al and Au corresponding to about 0.2 and 0.4 the range in the materials at 2.5 MeV were used. The incident beam direction, as at 1.0 MeV, was normal to the target plane.

Measurements for an incident energy of 2.5 MeV were considered important for several reasons. Primarily, however, data at this energy provided a tie-on to the measurements performed at Gulf General Atomic at higher energies. In as much as the G.A. linac can be operated at low energy only with difficulty the use of the LTV Van de Graaff near the upper limit of its range provided a much more

efficient means of obtaining the data. The energy step from 1.0 MeV to 2.5 MeV is significantly large, on the other hand, because of the energy dependence of the scattering process to justify making the measurements. The same experimental arrangement was used at the higher energy as had been used earlier at 1.0 MeV.

Comparisons of the Monte Carlo spectra and the experimental spectra are made below for both Al and Au targets for an incident energy of 2.5 MeV. For completeness, comparisons of the measurements on Au targets for an incident energy of 1.0 MeV to the computations are also included so that the quality of the comparisons for both Al and Au can be seen as a function of energy.

EXPERIMENTAL RESULTS

Measurements of electron penetration of two targets of Al and of Au were carried out for normal incidence of a 2.5-MeV electron beam from the LTV Van de Graaff accelerator. The experimental arrangement used in making the measurements was the same as that described in NASA CR 334.[1] However, for the measurements at 2.5 MeV incident energy a 5-mm thick Si(Li) detector was employed. This thickness is sufficient to stop electrons of energies up to 2.5 MeV. The resolution of the detector in the energy range of interest was 22 keV f.w.h.m. The response of the detector was determined from measurements of internal conversion spectra from radioactive sources and of mono-energetic particles from the accelerator. The technique for converting pulse height distributions to energy spectra was described in the above-mentioned report.

The angular distributions of transmitted electrons for the four targets are shown in Fig. 1. Calculated and experimental values are given. The calculated values were obtained from Seltzer and Berger's Code ETRAN 15, although the values shown were actually provided from runs made at the Marshall Space Flight Center. A total of 15,000 histories were followed in the computation for both Al and Au. The agreement between the experiment and the computation is good for the case of the Al targets. At angles less than 20 deg the two are nearly identical for both targets. At larger angles for the thicker Al target the agreement is also good. In this region for the thinner Al target, the two are not as close but within experimental and statistical error. The comparison for Au shows good agreement between the two distributions for the thinner target. A significant difference between experiment and computation is seen for the thicker target. However, in the latter comparison the computed values are for a slightly thicker target than the one actually used in the experiment. The total transmission coefficient for a thickness corresponding to 0.4 the range is less than 0.10. The target used in the experiment

was 0.753 g/cm^2, or .39 the range in Au at 2.5 MeV. The computed values were obtained for a target thickness of slightly more than 0.40 the range. Although the difference is small it does make about a 20% difference in the transmitted fraction of the beam, since the slope of the transmission curve plotted as a function of thickness is steep in this region. The effect of poor statistics is also apparent in the plot of the computed values and probably accounts for the apparent decrease in the yield, or lobe, near 0 deg.

The experimental energy distributions for Al are shown in Figs. 2-8. Those for Au are shown in Figs. 9-15. The average experimental uncertainty of these distributions is 10% at angles less than 45 deg and 15% at larger angles. However, for distributions like these, in the electron energy regions where the yield is 10% or less of the peak value, additional uncertainty exists in the data due to response removal and statistical error. The accuracy of the measurements on Al was unaffected by the presence of bremsstrahlung background. Background subtraction was simplified for the Al studies because of the large electron transmission coefficients and the relatively low bremsstrahlung production efficiency, as well as the low sensitivity of the detector to x-rays. For the measurements on the Au targets, however, low transmission and the presence of more bremsstrahlung resulted in additional difficulty in obtaining accurate electron spectra. For measurements on the thinner Au target possible error was eliminated by increasing the solid angle to electrons, thereby reducing the relative magnitude of the large background. For measurements on the thicker Au target a background of about 60% of the net electron count was measured. The effect of a background of this magnitude was to increase the uncertainty in the region of the electron distribution below the peak by about a factor of two. Therefore, the estimated error in the electron energy region below 0.75 MeV is about 20%.

Comparisons of the experimental total transmission spectra, derived by numerical integration over solid angle, to the computed

spectra are shown in Figs. 16-19. In Fig. 16 the two transmission spectra are shown for the Al target of thickness corresponding to 0.2 the range in Al at 2.5 MeV. The computed spectrum is shifted relative to the experimental spectrum toward higher energy by about 25 keV, or by about 1% of the incident energy. The integration of these curves over energy from 0.25 MeV gives an experimental transmission coefficient of 0.89 and a computed transmission coefficient of 0.98. In Fig. 17 the comparison of the experimental and Monte Carlo spectra shows good agreement between the shapes of the two distributions for the thicker Al targets. The experimental and computed transmission coefficients are 0.68 and 0.74, respectively. The comparisons for Al targets at 2.5 MeV are very similar to those at 1.0 MeV for spectra from ETRAN 5, except that somewhat better agreement is actually observed between experiment and computation at 2.5 MeV for the target corresponding to 0.2 the range. The transmission spectra for Au for a target thickness of 0.2 the range, Fig. 18, also shows good agreement between the shapes of the distributions. The experimental and computed transmission coefficients are 0.48 and 0.51, respectively. The spectra for 0.4 the range are shown in Fig. 19. There is a small difference in the target thicknesses for the two sets of data. As discussed above the difference is almost enough to account for the observed discrepancy in the transmission coefficients, 0.09 for the experiment and 0.06 for the computation. The statistical uncertainty in the computed spectrum is apparent from the fluctuations of the bins. A significant improvement in the statistical accuracy would require more than five times the number of histories as were recorded for the data shown here. The comparisons of the total transmitted spectra at 1.0 MeV are shown in Figs. 20-21 for Au. The disagreement between the two in Fig. 20 in total intensity is apparent from the drawing. In addition, the shapes of the two distributions are different. At 2.5 MeV spectral shapes for the corresponding thickness were in better agreement. At 1.0 MeV the computed spectrum actually exhibits more straggling

than is shown by the experiment to exist. The comparison for the thicker target reveals little quantitatively because of the large statistical fluctuations of the calculated spectrum, which was generated from following 15,000 histories.

Comparisons of various spectra at individual angles are shown in Figs. 22-26. Two computed spectra are given in each figure which bracket the experimental spectrum. The difficulty of comparing the experimental and computed spectra at most angles is due to the poor statistics of the computed spectra, as can be seen by the fluctuations. From the experiment, however, it was observed that the energy spectra vary with angle only slightly. The larger variations occur at large angles, typically at angles greater than 60 deg. The yield in this region is relatively low, on the other hand, so that the comparisons of the angular distributions and total transmission spectra are sufficient to determine the extent to which the computations predict the experiment. A somewhat disappointing feature of the Monte Carlo program in its present form is the computing time required to obtain valid data for materials of thicknesses which result in 5% transmission or less. Good data for low transmission thicknesses may prove to be very valuable for shielding calculations.

REFERENCES

1. D. H. Rester and W. J. Rainwater, Jr., "Investigations of Electron Interactions in Matter", Part 2. Electron Scattering in Aluminum, NASA CR-334, December 1965.

2. D. H. Rester and W. E. Dance, "Electron Scattering and Bremsstrahlung Cross-Section Measurements", NASA CR-759, April 1967.

FIGURE CAPTIONS

Fig. 1 Experimental and computed angular distributions of transmitted electrons for two targets of Al and Au. For Al the targets used in the experiment and computation corresponded to 0.2 and 0.4 the range in Al (ρ = 0.2 and ρ = 0.4) at an incident energy of 2.5 MeV. For Au the thinner target also corresponded to ρ = 0.2 for both the experiment and computation. However, the actual thickness of the other Au target used in the experiment was ρ = 0.39, while the thickness assumed in the computation was ρ = 0.40. The difference in thickness accounts in part for higher experimental transmission value.

Fig. 2 Transmission spectrum of electrons of incident kinetic energy of 2.5 MeV, bombarding an Al target of thickness ρ = 0.2, observed at an angle of 0 deg with respect to the incident beam direction.

Fig. 3 Transmission spectrum of electrons of incident kinetic energy of 2.5 MeV, bombarding an Al target of thickness ρ = 0.2, observed at an angle of 10 deg with respect to the incident beam direction.

Fig. 4 Transmission spectra of electrons of incident kinetic energy of 2.5 MeV, bombarding an Al target of thickness ρ = 0.2, observed at angles of 20, 30, and 45 deg with respect to the incident beam direction.

Fig. 5 Transmission spectra of electrons of incident kinetic energy of 2.5 MeV, bombarding an Al target of thickness ρ = 0.2, observed at angles of 60 and 75 deg with respect to the incident beam direction.

Fig. 6 Transmission spectrum of electrons of incident kinetic energy of 2.5 MeV, bombarding an Al target of thickness $\rho = 0.4$, observed at an angle of 0 deg with respect to the incident beam direction.

Fig. 7 Transmission spectrum of electrons of incident kinetic energy of 2.5 MeV, bombarding an Al target of thickness $\rho = 0.4$, observed at an angle of 10 deg with respect to the incident beam direction.

Fig. 8 Transmission spectra of electrons of incident kinetic energy of 2.5 MeV, bombarding an Al target of thickness $\rho = 0.4$, observed at angles of 20, 30, 45, 60, and 75 deg with respect to the incident beam direction.

Fig. 9 Transmission spectrum of electrons of incident kinetic energy of 2.5 MeV, bombarding a Au target of thickness $\rho = 0.2$, observed at an angle of 10 deg with respect to the incident beam direction.

Fig. 10 Transmission spectra of electrons of incident kinetic energy of 2.5 MeV, bombarding a Au target of thickness $\rho = 0.2$, observed at angles of 20, 30, 45, 60, and 75 deg with respect to the incident beam direction.

Fig. 11 Transmission spectrum of electrons of incident kinetic energy of 2.5 MeV, bombarding a Au target of thickness $\rho = 0.39$, observed at an angle of 0 deg with respect to the incident beam direction.

Fig. 12 Transmission spectrum of electrons of incident kinetic energy of 2.5 MeV, bombarding a Au target of thickness $\rho = 0.39$, observed at an angle of 10 deg with respect to the incident beam direction.

Fig. 13 Transmission spectrum of electrons of incident kinetic energy of 2.5 MeV, bombarding a Au target of thickness $\rho = 0.39$, observed at an angle of 20 deg with respect to the incident beam direction.

Fig. 14 Transmission spectrum of electrons of incident kinetic energy of 2.5 MeV, bombarding a Au target of thickness $\rho = 0.39$, observed at an angle of 30 deg with respect to the incident beam direction.

Fig. 15 Transmission spectra of electrons of incident kinetic energy of 2.5 MeV, bombarding a Au target of thickness $\rho = 0.39$, observed at angles of 45, 60, and 75 deg with respect to the incident beam direction.

Fig. 16 Comparison of computed and experimental transmission spectra for the Al target of thickness $\rho = 0.2$ for an incident kinetic energy of 2.5 MeV.

Fig. 17 Comparison of computed and experimental transmission spectra for the Al target of thickness $\rho = 0.4$ for an incident kinetic energy of 2.5 MeV.

Fig. 18 Comparison of computed and experimental transmission spectra for the Au target of thickness $\rho = 0.2$ for an incident kinetic energy of 2.5 MeV.

Fig. 19 Comparison of computed spectrum for a Au target of thickness $\rho = 0.4$ to an experimental spectrum for a Au target of thickness $\rho = 0.39$ for an incident kinetic energy of 2.5 MeV.

Fig. 20 Comparison of computed and experimental transmission spectra for a Au target of thickness $\rho = 0.2$ for an incident kinetic energy of 1.0 MeV.

Fig. 21 Comparison of computed and experimental transmission spectra for a Au target of thickness $\rho = 0.4$ for an incident kinetic energy of 1.0 MeV.

Fig. 22 Comparisons of computed and experimental transmitted spectra at an experimental angle of observation $\delta = 0$ deg and for $\rho = 0.2$ and $Z = 13$.

Fig. 23 Comparisons of computed and experimental transmitted spectra at an experimental angle of observation $\delta = 20$ deg and for $\rho = 0.2$ and $Z = 13$.

Fig. 24 Comparisons of computed and experimental transmitted spectra at an experimental angle of observation $\delta = 45$ deg and for $\rho = 0.2$ and $Z = 13$.

Fig. 25 Comparisons of computed and experimental transmitted spectra at an experimental angle of observation $\delta = 10$ deg and for $\rho = 0.4$ and $Z = 13$.

Fig. 26 Comparisons of computed and experimental transmitted spectra at an experimental angle of observation $\delta = 20$ deg and for $\rho = 0.4$ and $Z = 13$.

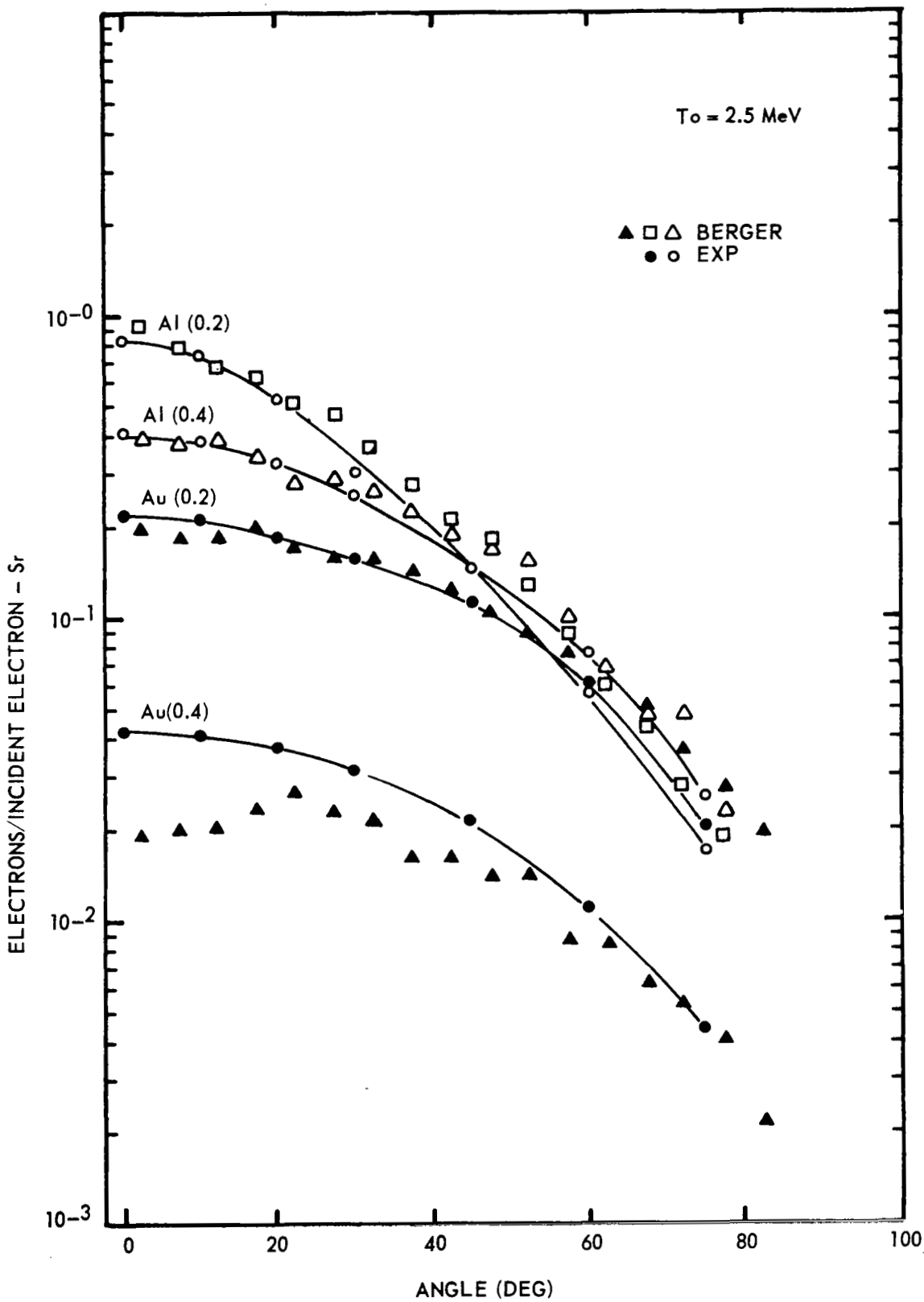
To = 2.5 MeV
▲ □ △ BERGER
● o EXP
Al (0.2)
Al (0.4)
Au (0.2)
Au(0.4)
10−0
10−1
10−2
10−3
ELECTRONS/INCIDENT ELECTRON - Sr
0
20
40
60
80
100
ANGLE (DEG)

FIGURE 1

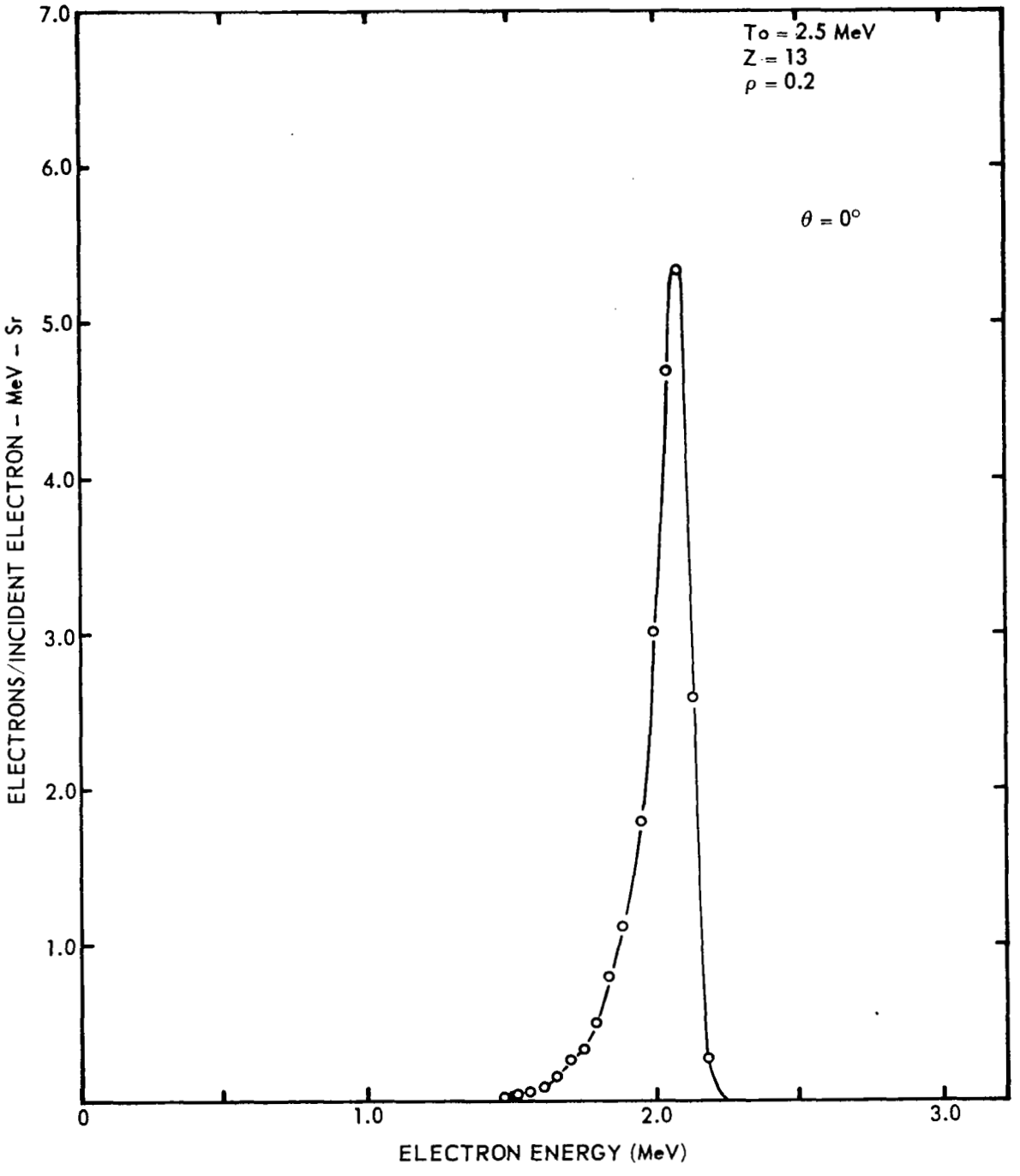
To = 2.5 MeV
Z = 13
ρ = 0.2
θ = 0°
ELECTRONS/INCIDENT ELECTRON - MeV - Sr
ELECTRON ENERGY (MeV)
7.0
6.0
5.0
4.0
3.0
2.0
1.0
0
1.0
2.0
3.0

FIGURE 2

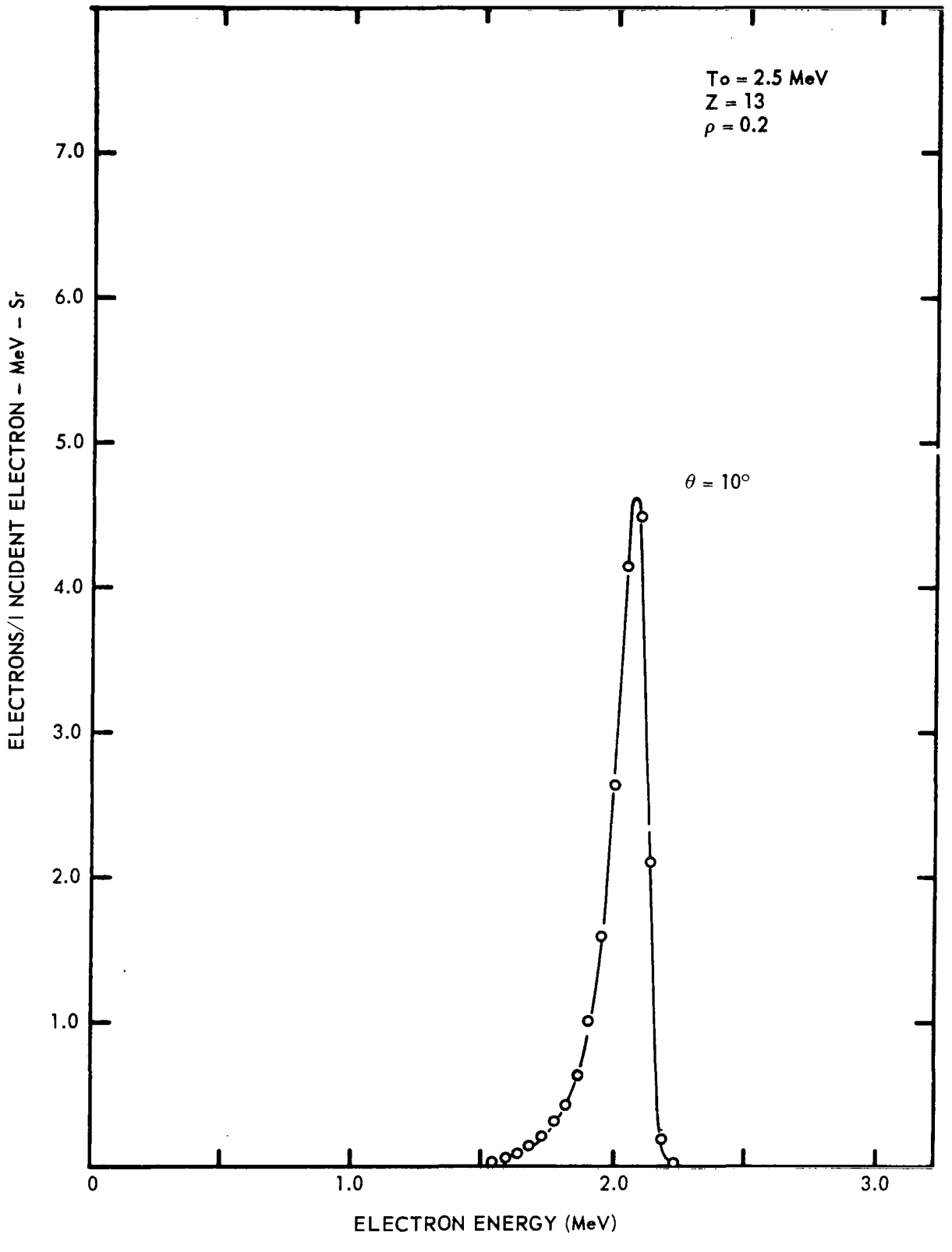
To = 2.5 MeV
Z = 13
ρ = 0.2
θ = 10°
ELECTRONS/INCIDENT ELECTRON - MeV - Sr
7.0
6.0
5.0
4.0
3.0
2.0
1.0
0
1.0
2.0
3.0
ELECTRON ENERGY (MeV)

FIGURE 3

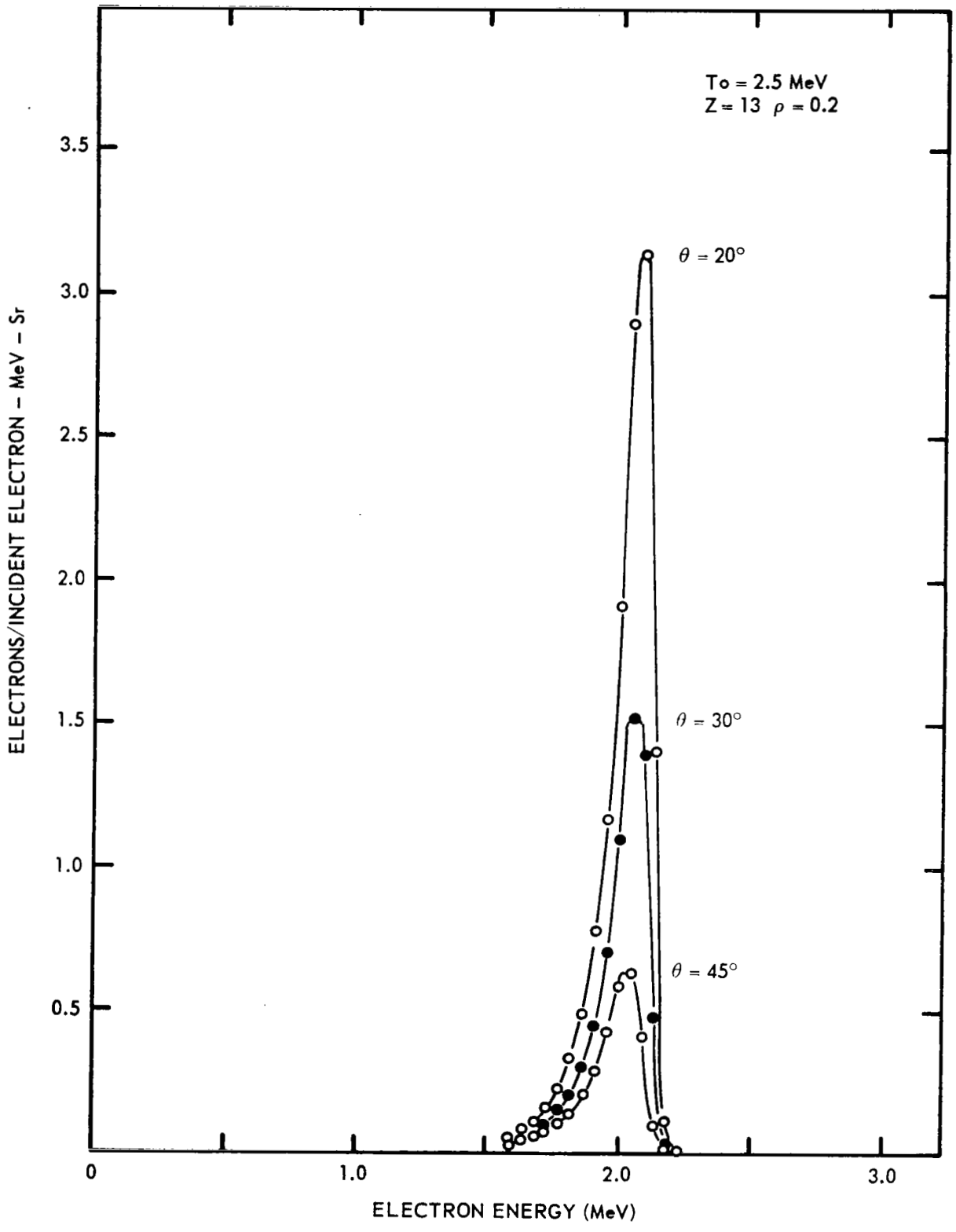
To = 2.5 MeV
Z = 13 ρ = 0.2
θ = 20°
θ = 30°
θ = 45°
ELECTRONS/INCIDENT ELECTRON - MeV - Sr
ELECTRON ENERGY (MeV)
0
0.5
1.0
1.5
2.0
2.5
3.0
3.5
1.0
2.0
3.0

FIGURE 4

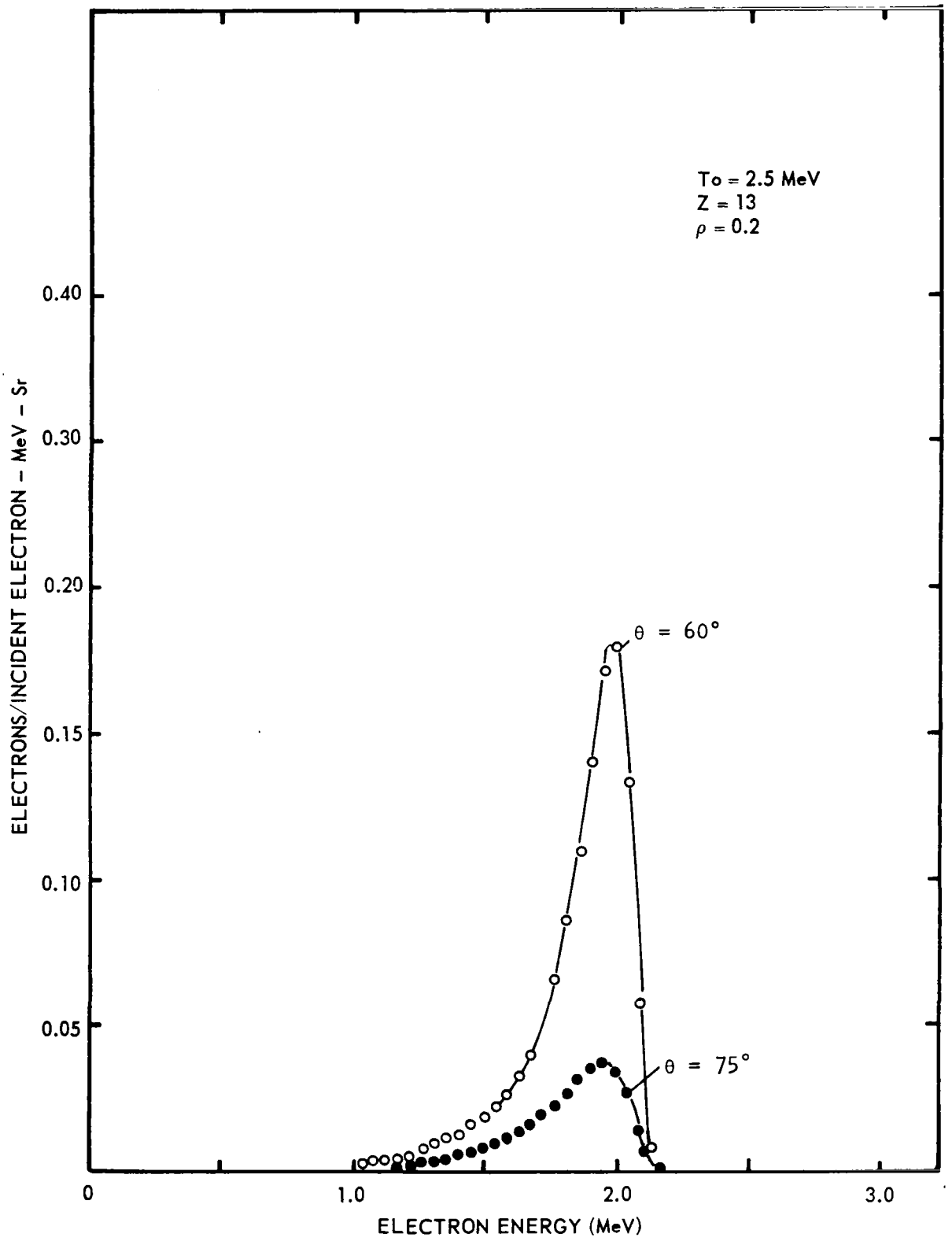
To = 2.5 MeV
Z = 13
ρ = 0.2
θ = 60°
θ = 75°
ELECTRONS/INCIDENT ELECTRON – MeV – Sr
0.40
0.30
0.20
0.15
0.10
0.05
0
1.0
2.0
3.0
ELECTRON ENERGY (MeV)

FIGURE 5

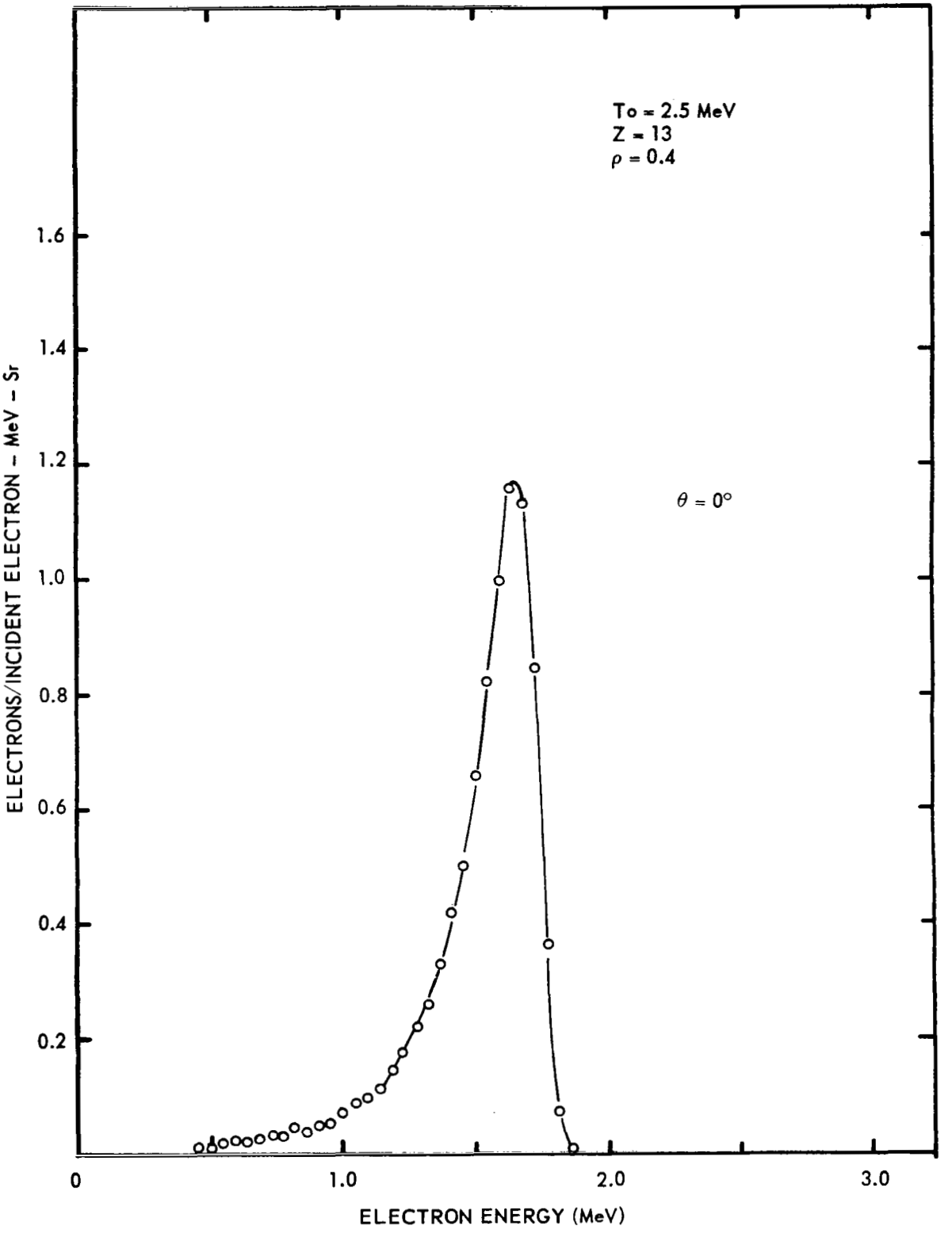
To = 2.5 MeV
Z = 13
ρ = 0.4
θ = 0°
ELECTRONS/INCIDENT ELECTRON - MeV - Sr
1.6
1.4
1.2
1.0
0.8
0.6
0.4
0.2
0
1.0
2.0
3.0
ELECTRON ENERGY (MeV)

FIGURE 6

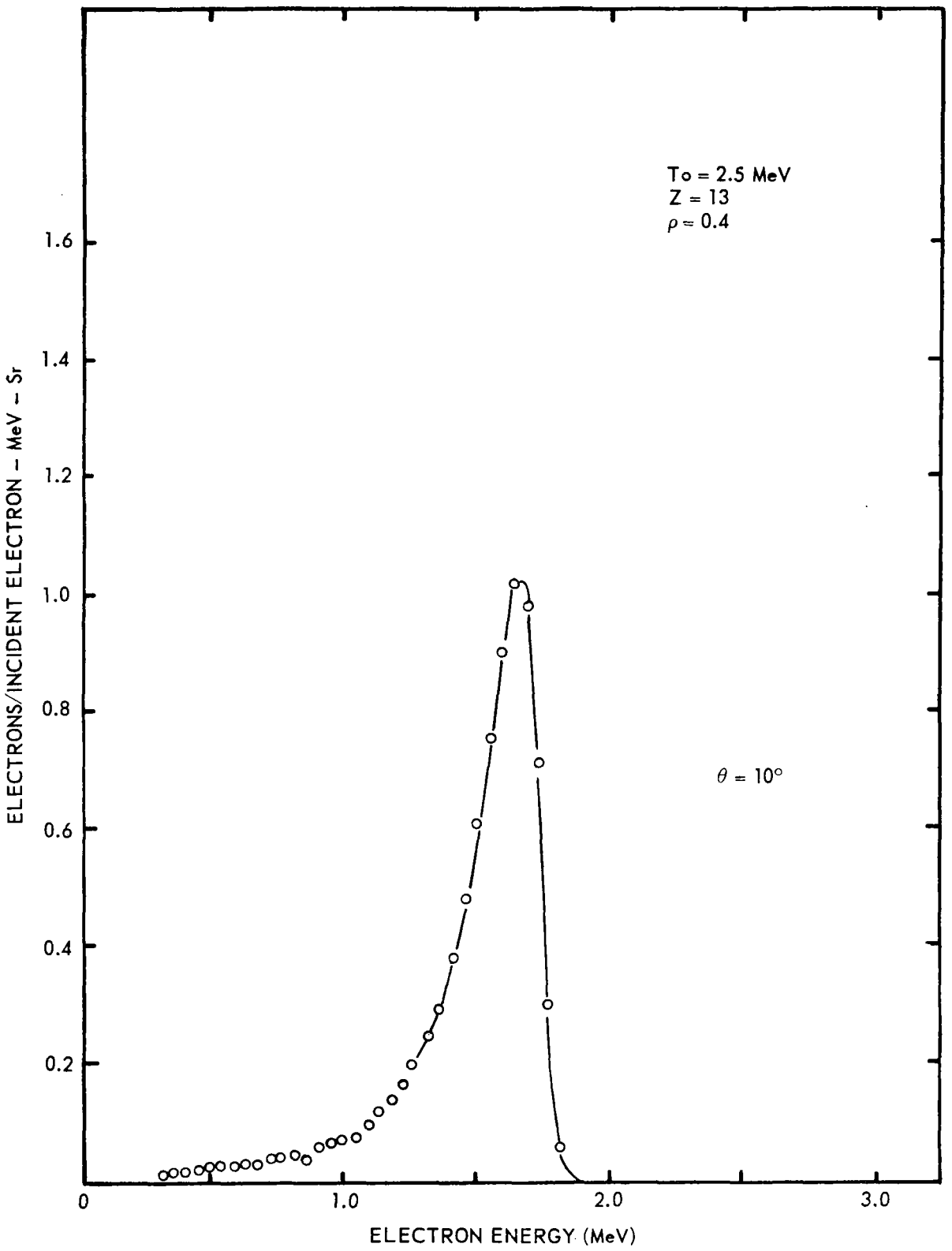
To = 2.5 MeV
Z = 13
ρ = 0.4
θ = 10°
ELECTRONS/INCIDENT ELECTRON – MeV – Sr
ELECTRON ENERGY (MeV)
0
1.0
2.0
3.0
0.2
0.4
0.6
0.8
1.0
1.2
1.4
1.6

FIGURE 7

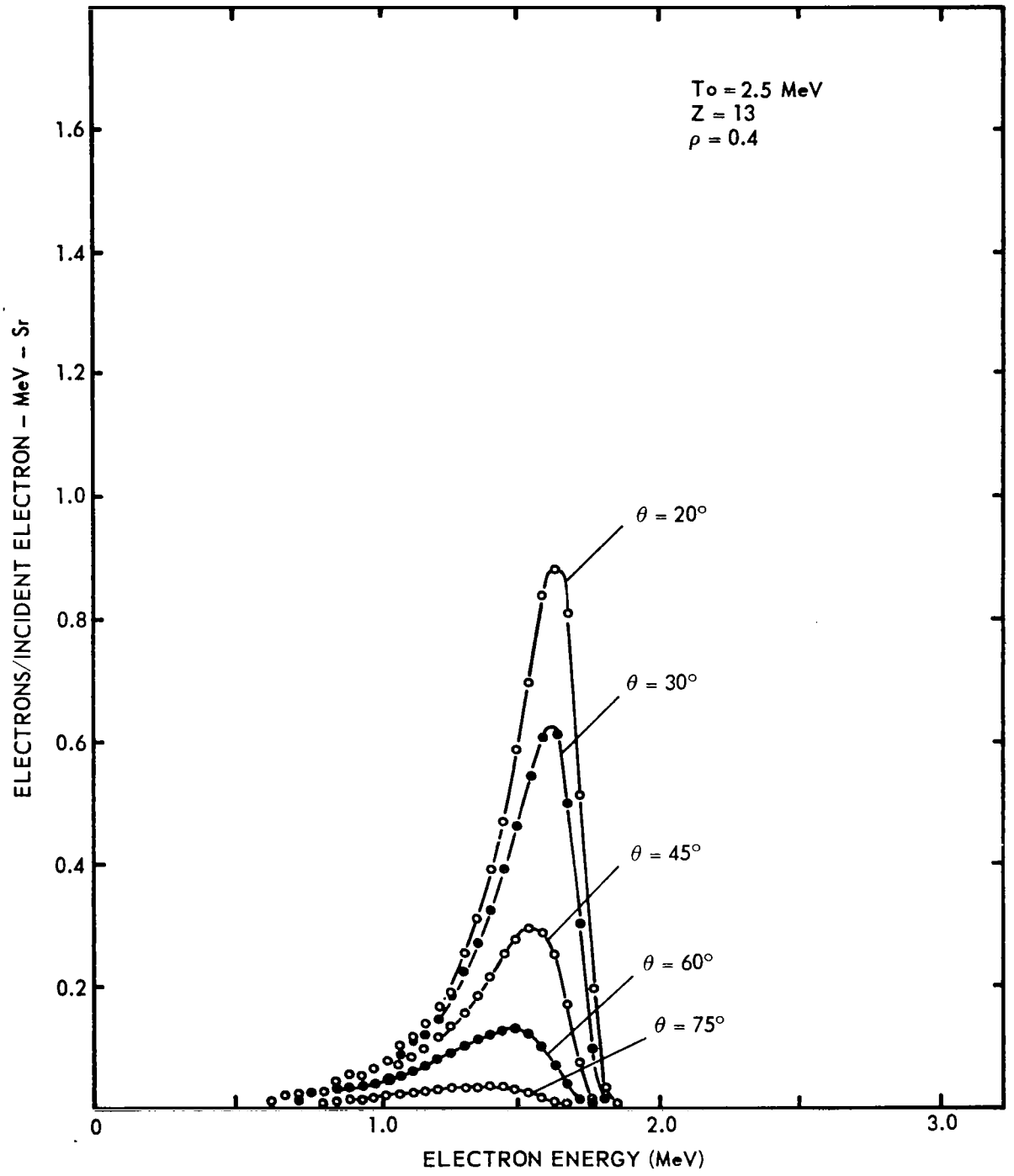
To = 2.5 MeV
Z = 13
ρ = 0.4
θ = 20°
θ = 30°
θ = 45°
θ = 60°
θ = 75°
ELECTRONS/INCIDENT ELECTRON – MeV – Sr
ELECTRON ENERGY (MeV)
0
1.0
2.0
3.0
0.2
0.4
0.6
0.8
1.0
1.2
1.4
1.6

FIGURE 8

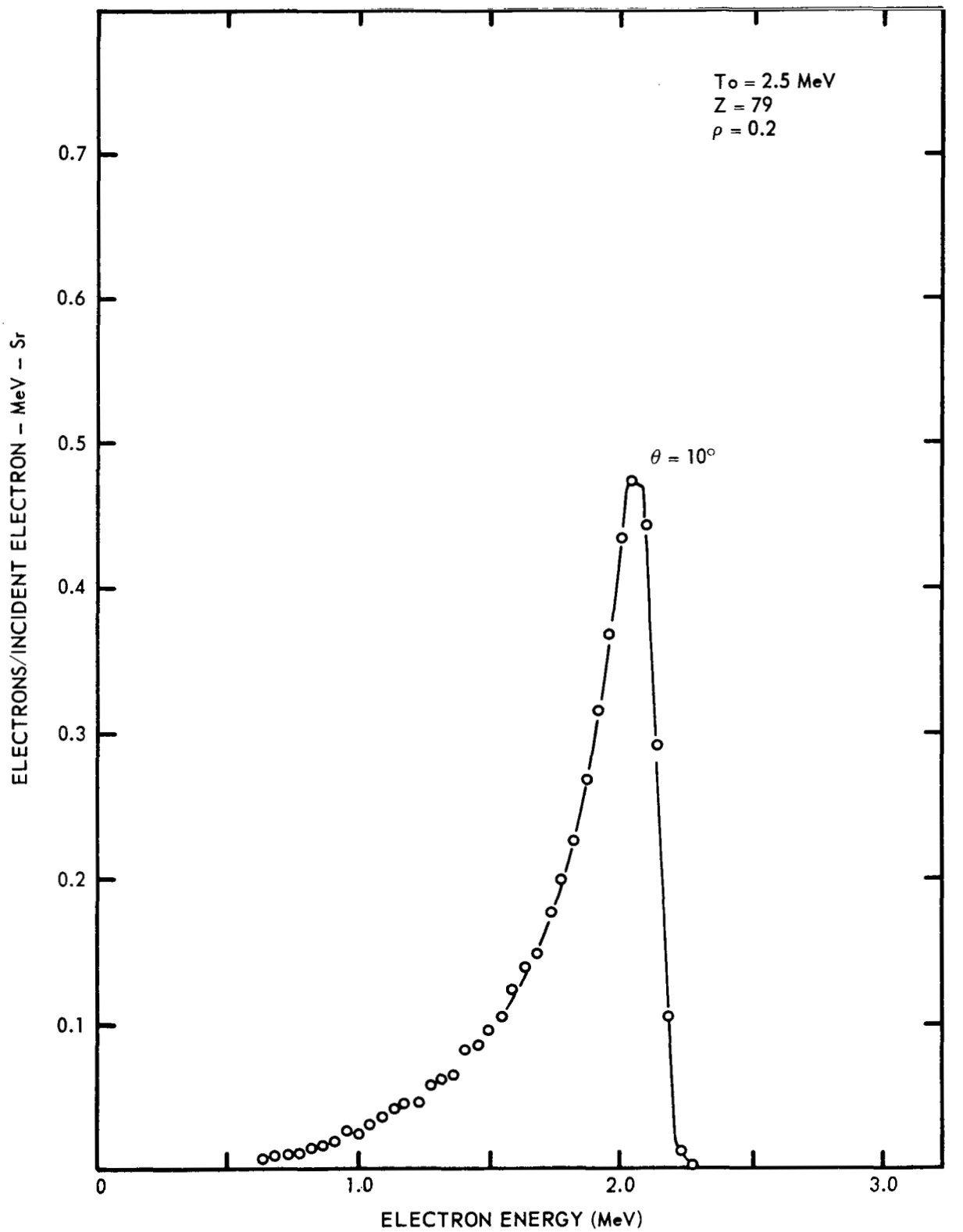
To = 2.5 MeV
Z = 79
ρ = 0.2
θ = 10°
ELECTRONS/INCIDENT ELECTRON – MeV – Sr
0.7
0.6
0.5
0.4
0.3
0.2
0.1
0
1.0
2.0
3.0
ELECTRON ENERGY (MeV)

FIGURE 9

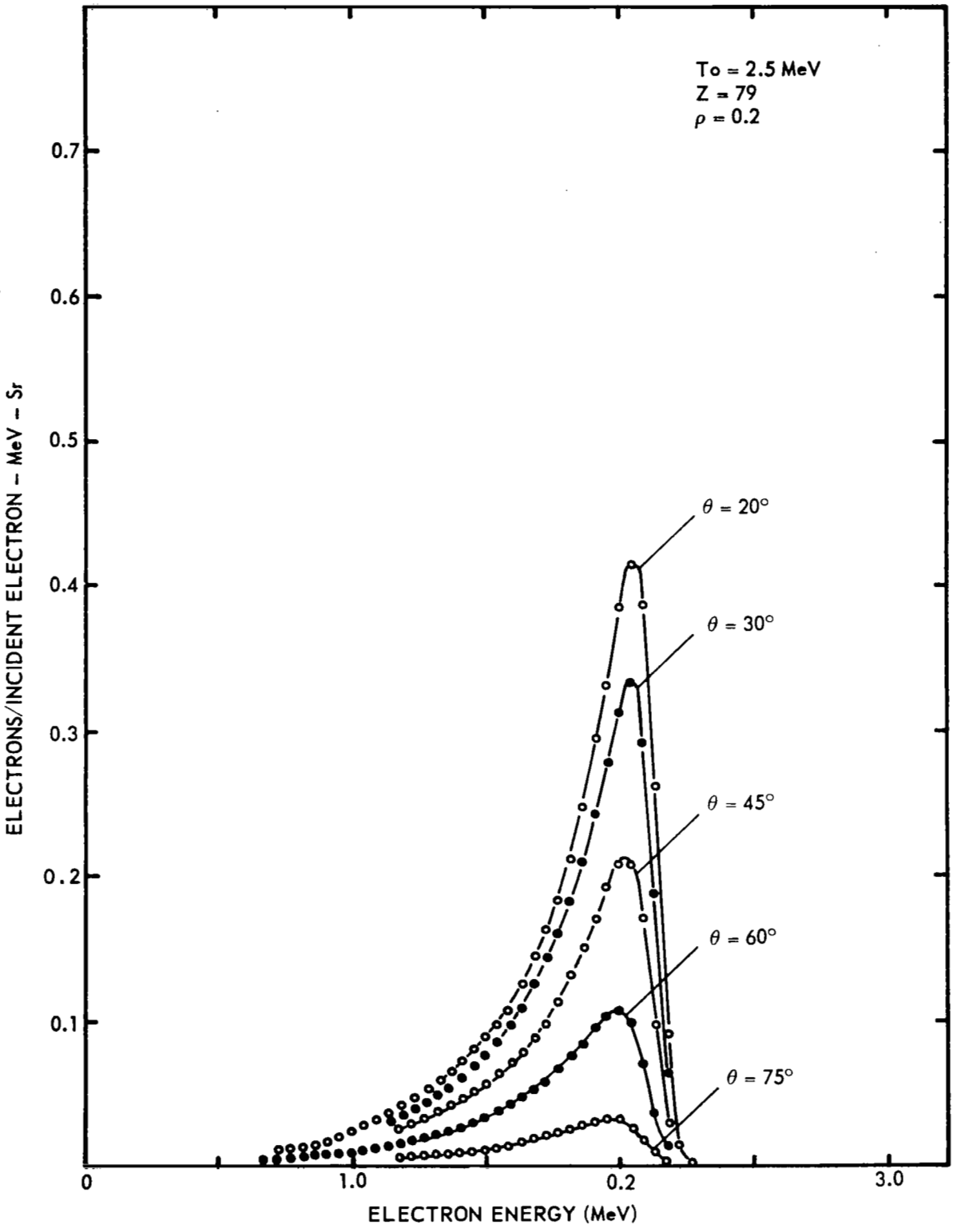
To = 2.5 MeV
Z = 79
ρ = 0.2
θ = 20°
θ = 30°
θ = 45°
θ = 60°
θ = 75°
ELECTRONS/INCIDENT ELECTRON - MeV - Sr
0.7
0.6
0.5
0.4
0.3
0.2
0.1
0
1.0
0.2
3.0
ELECTRON ENERGY (MeV)

FIGURE 10

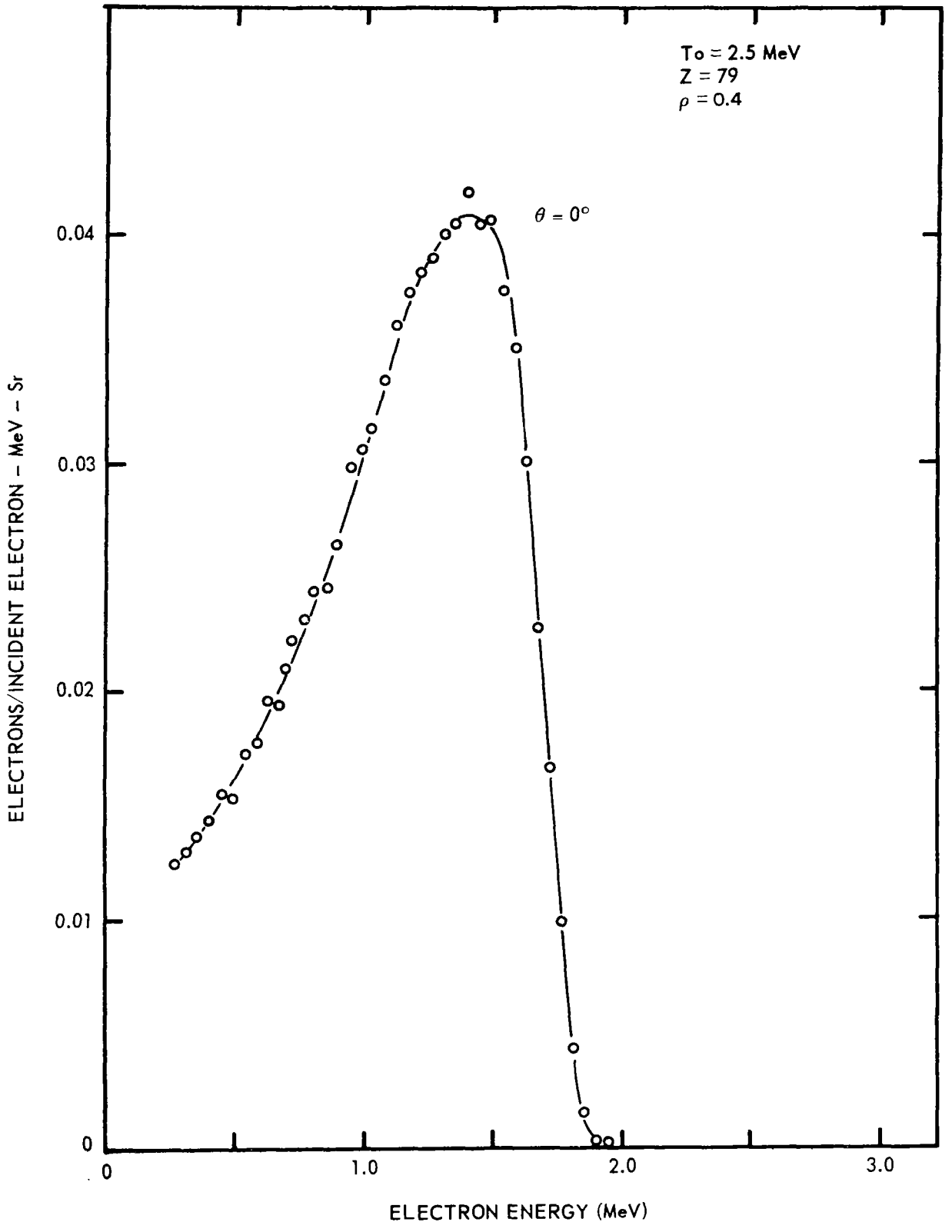
To = 2.5 MeV
Z = 79
ρ = 0.4
θ = 0°
0.04
0.03
0.02
0.01
0
0
1.0
2.0
3.0
ELECTRONS/INCIDENT ELECTRON - MeV - Sr
ELECTRON ENERGY (MeV)

FIGURE 11

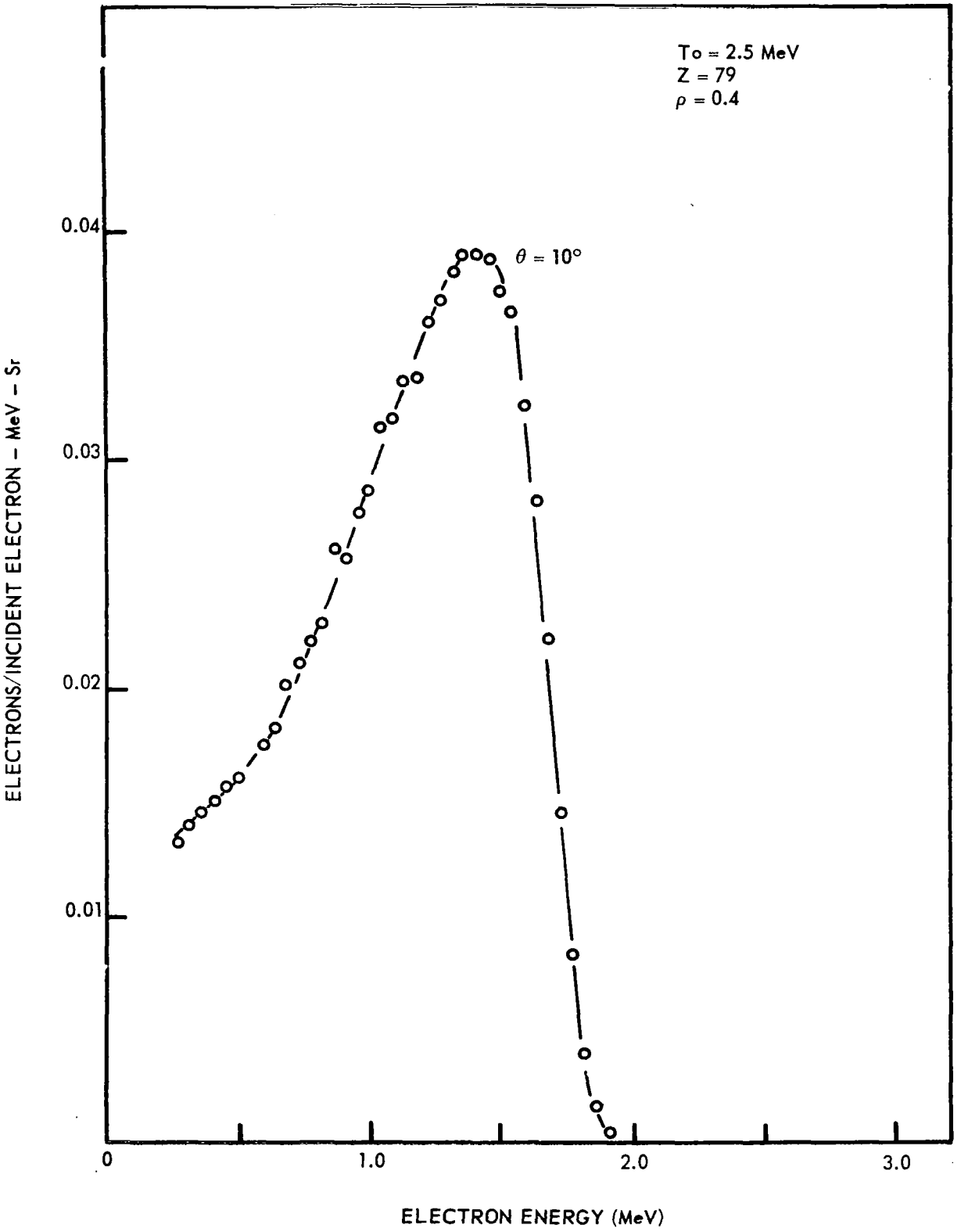
To = 2.5 MeV
Z = 79
ρ = 0.4
θ = 10°
0.04
0.03
0.02
0.01
0
1.0
2.0
3.0
ELECTRONS/INCIDENT ELECTRON - MeV - Sr
ELECTRON ENERGY (MeV)

FIGURE 12

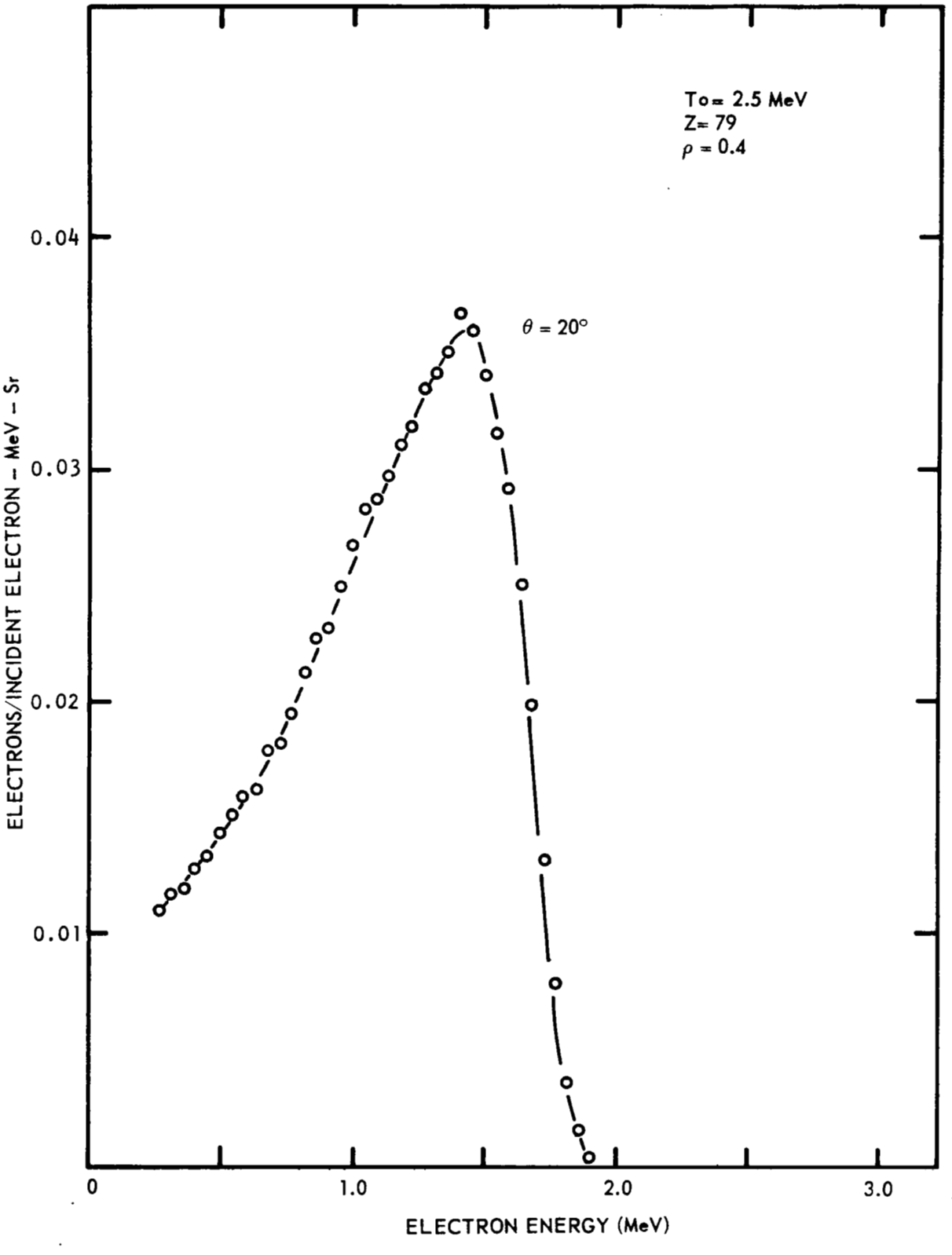
To= 2.5 MeV
Z= 79
ρ = 0.4
θ = 20°
0.04
0.03
0.02
0.01
ELECTRONS/INCIDENT ELECTRON - MeV - Sr
0
1.0
2.0
3.0
ELECTRON ENERGY (MeV)

FIGURE 13

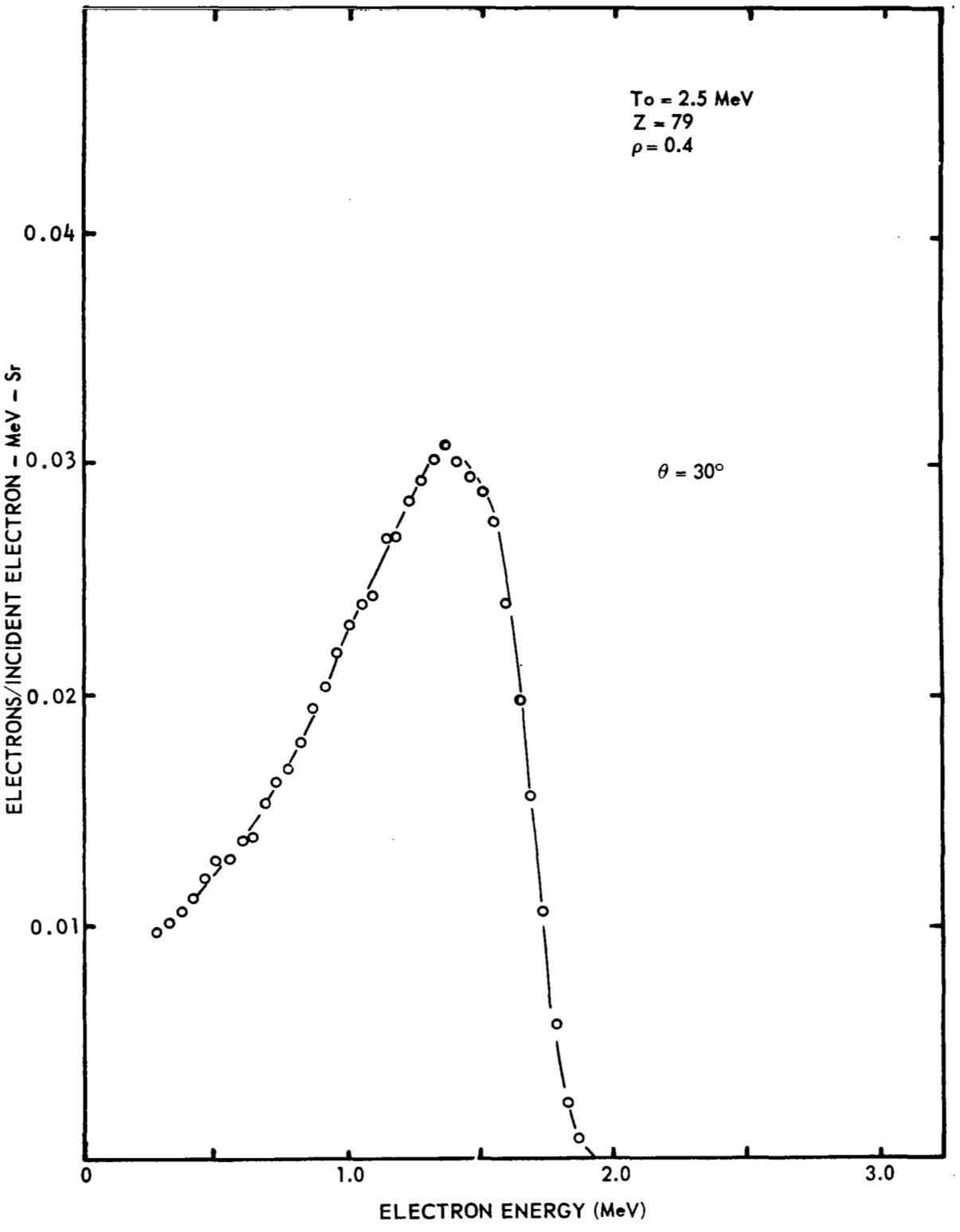
To = 2.5 MeV
Z = 79
ρ = 0.4
θ = 30°
0.04
0.03
0.02
0.01
0
1.0
2.0
3.0
ELECTRONS/INCIDENT ELECTRON - MeV - Sr
ELECTRON ENERGY (MeV)

FIGURE 14

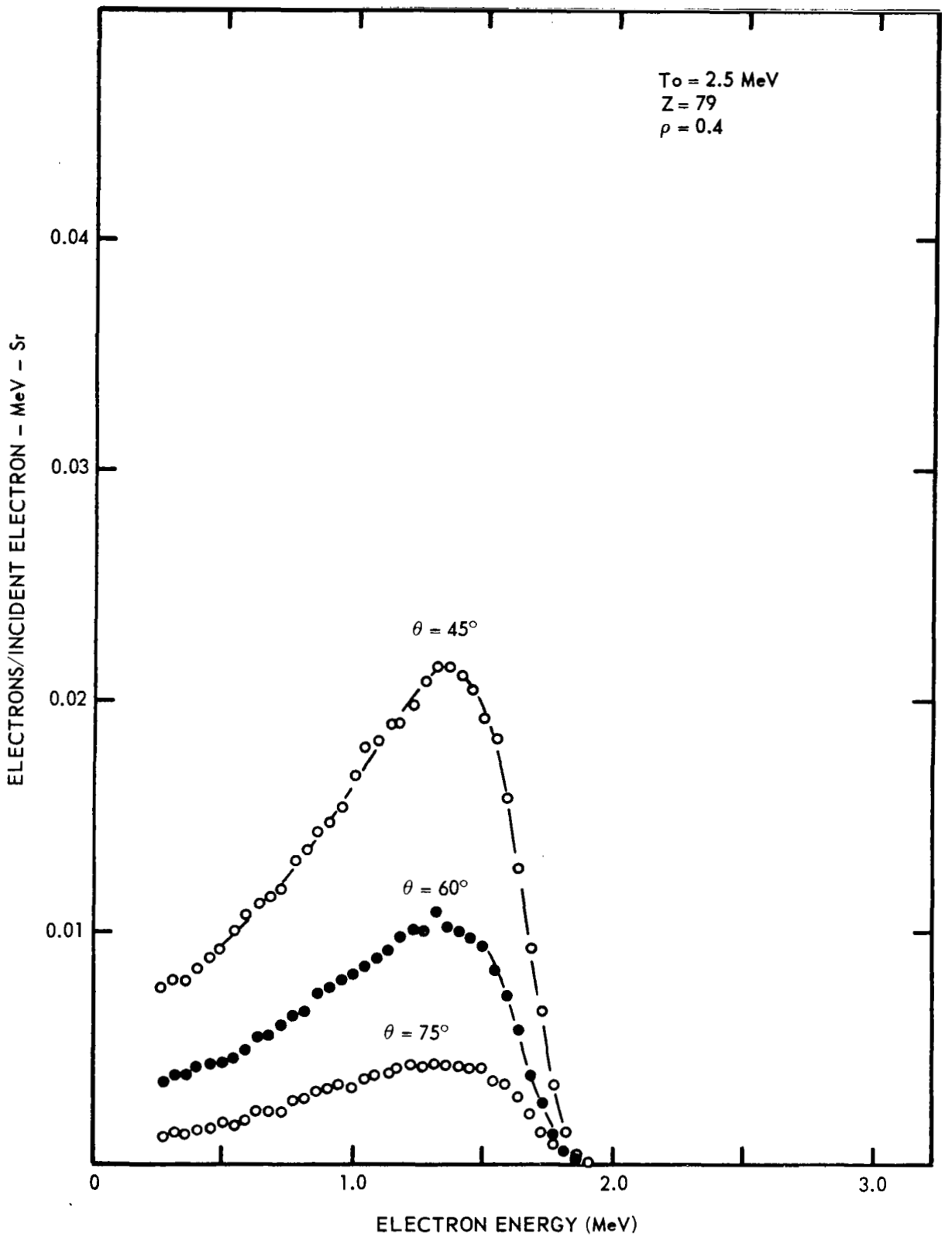
To = 2.5 MeV
Z = 79
ρ = 0.4
θ = 45°
θ = 60°
θ = 75°
0.04
0.03
0.02
0.01
0
1.0
2.0
3.0
ELECTRONS/INCIDENT ELECTRON – MeV – Sr
ELECTRON ENERGY (MeV)

FIGURE 15

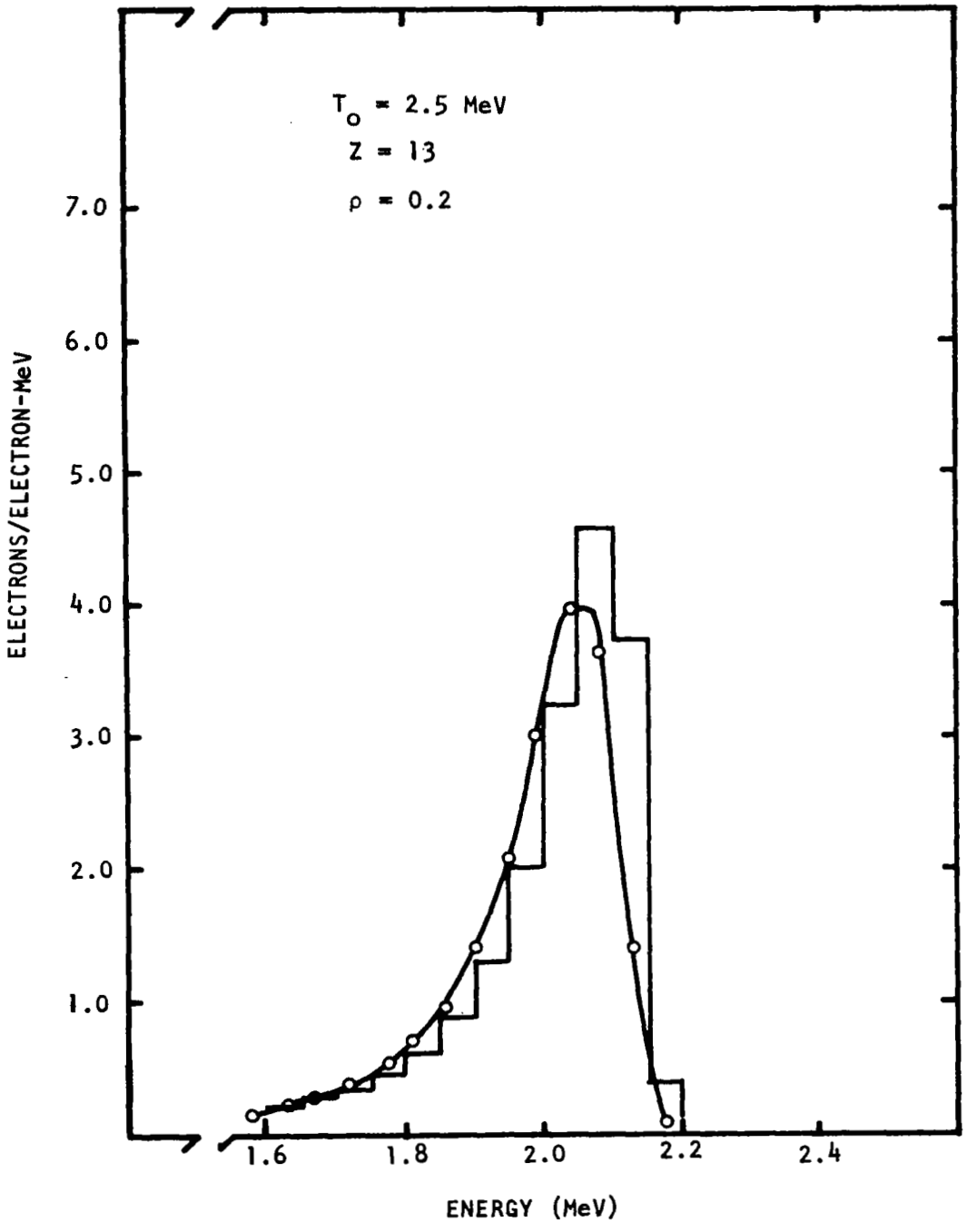
T_o = 2.5 MeV
Z = 13
ρ = 0.2
7.0
6.0
5.0
4.0
3.0
2.0
1.0
ELECTRONS/ELECTRON-MeV
1.6
1.8
2.0
2.2
2.4
ENERGY (MeV)

FIGURE 16

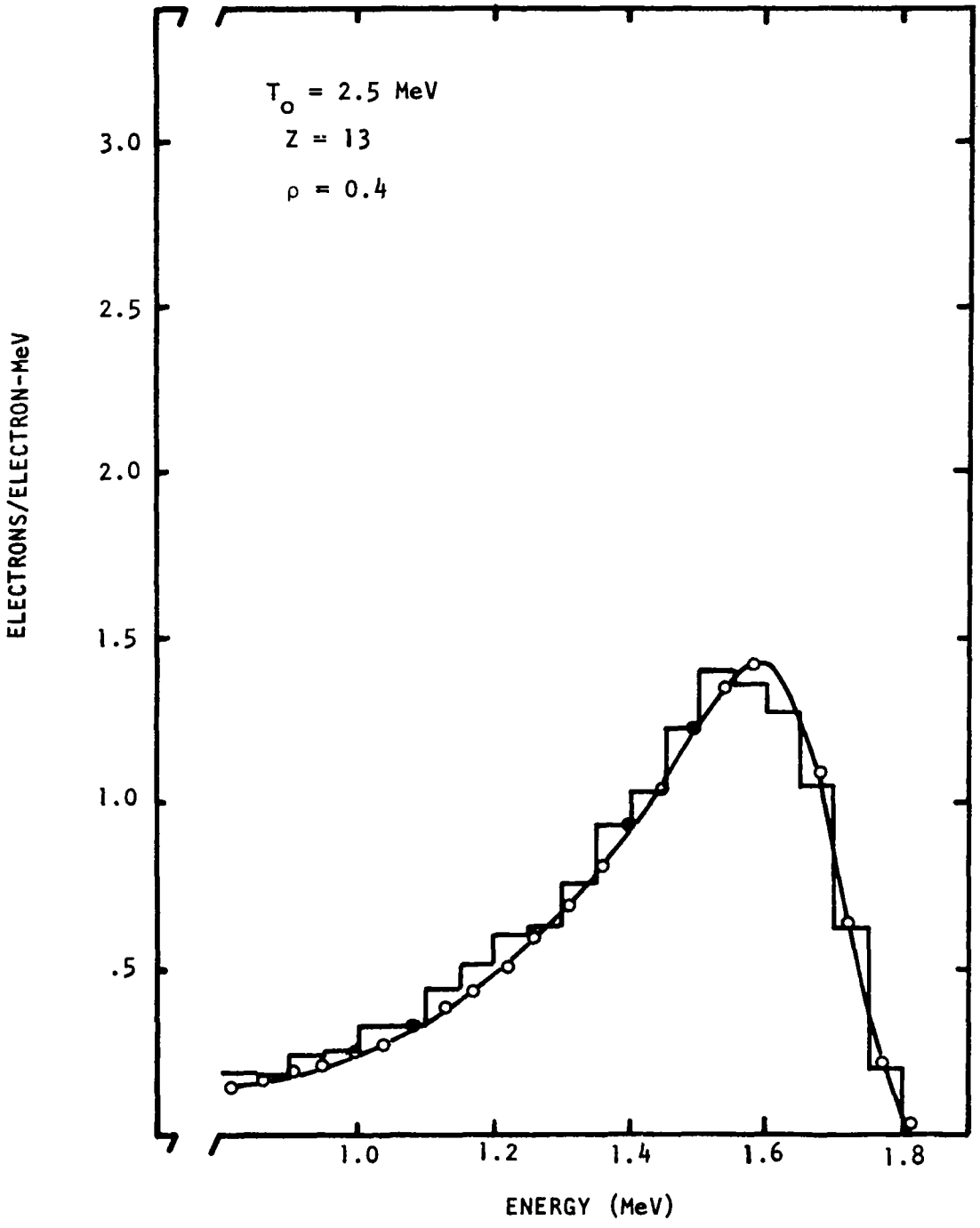
T_o = 2.5 MeV
Z = 13
ρ = 0.4
3.0
2.5
2.0
1.5
1.0
.5
ELECTRONS/ELECTRON-MeV
1.0
1.2
1.4
1.6
1.8
ENERGY (MeV)

FIGURE 17

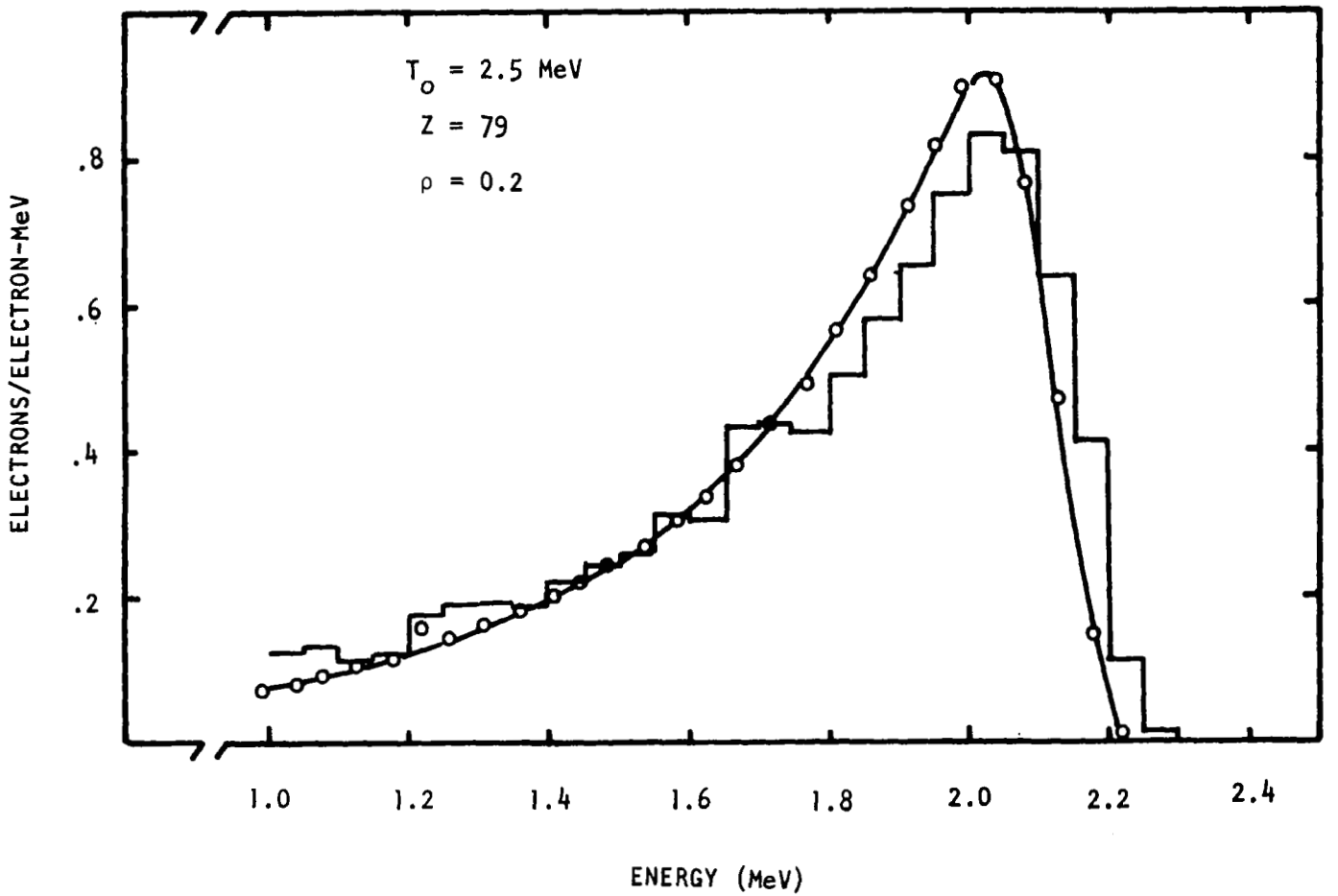
T_o = 2.5 MeV
Z = 79
ρ = 0.2
ELECTRONS/ELECTRON-MeV
.2
.4
.6
.8
1.0
1.2
1.4
1.6
1.8
2.0
2.2
2.4
ENERGY (MeV)

FIGURE 18

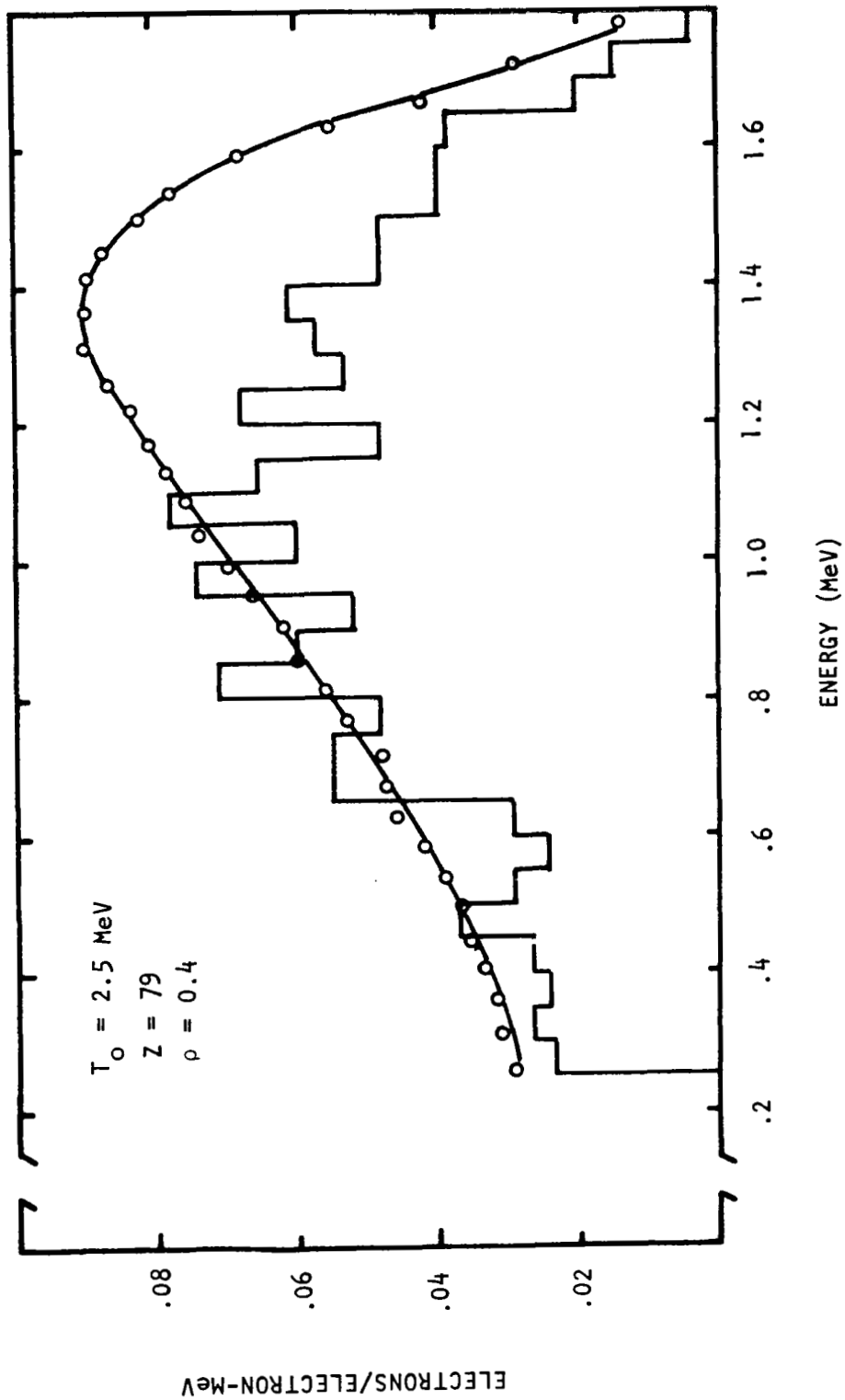
T_o = 2.5 MeV
Z = 79
ρ = 0.4
.02
.04
.06
.08
.2
.4
.6
.8
1.0
1.2
1.4
1.6
ENERGY (MeV)
ELECTRONS/ELECTRON-MeV

FIGURE 19

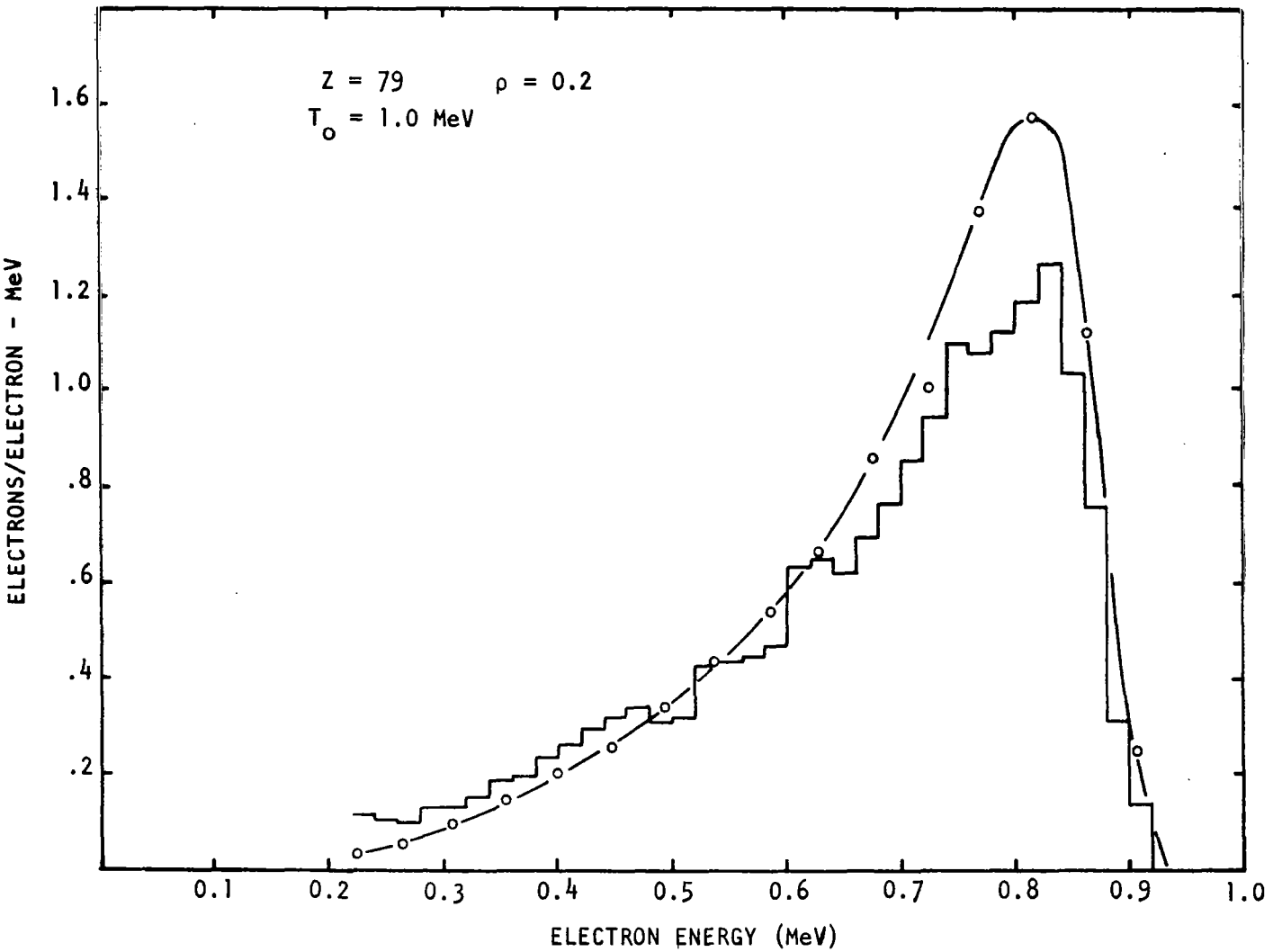
Z = 79
ρ = 0.2
T_o = 1.0 MeV
ELECTRONS/ELECTRON - MeV
1.6
1.4
1.2
1.0
.8
.6
.4
.2
0.1
0.2
0.3
0.4
0.5
0.6
0.7
0.8
0.9
1.0
ELECTRON ENERGY (MeV)

FIGURE 20

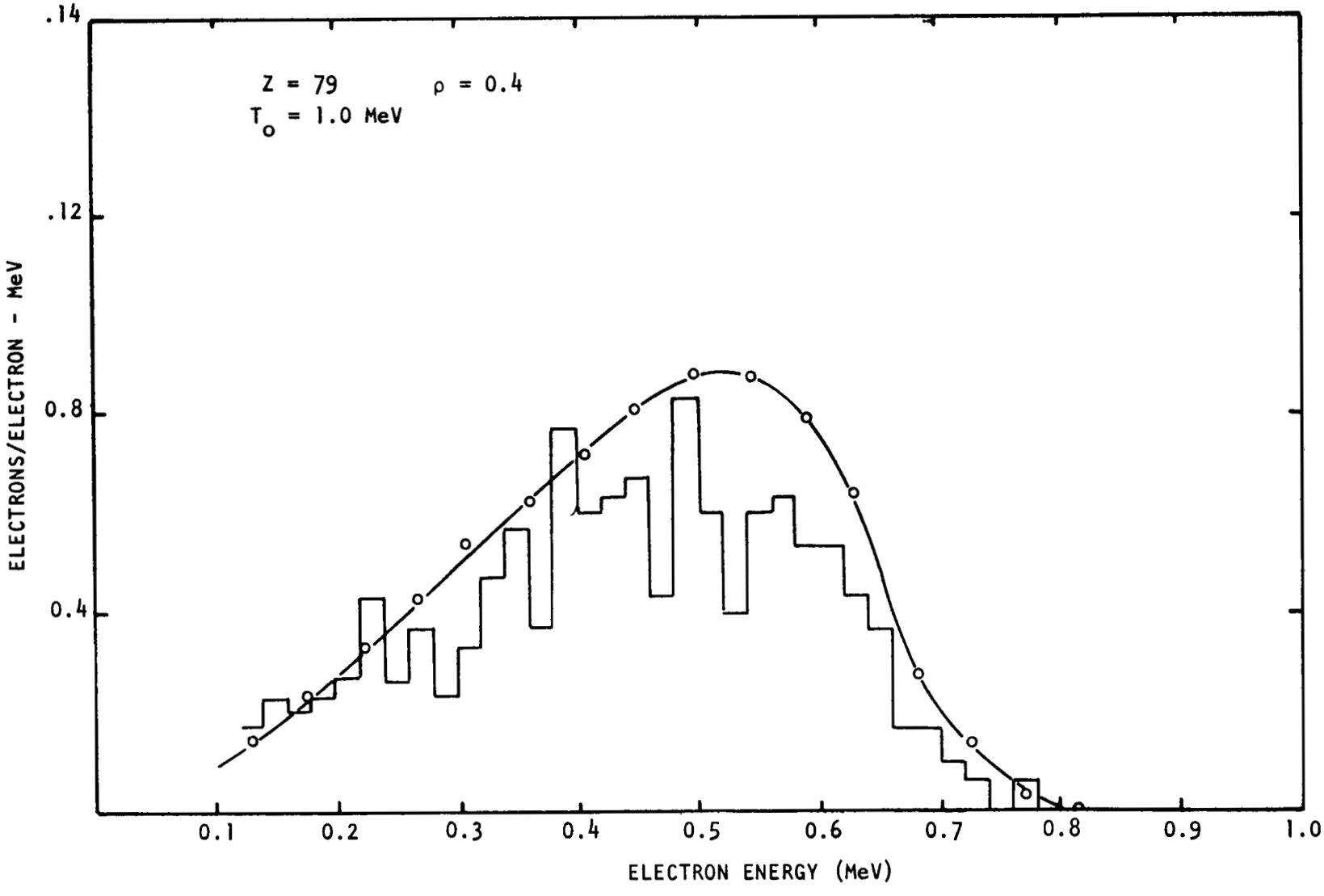
Z = 79
ρ = 0.4
T_o = 1.0 MeV
.14
.12
0.8
0.4
ELECTRONS/ELECTRON - MeV
0.1
0.2
0.3
0.4
0.5
0.6
0.7
0.8
0.9
1.0
ELECTRON ENERGY (MeV)

FIGURE 21

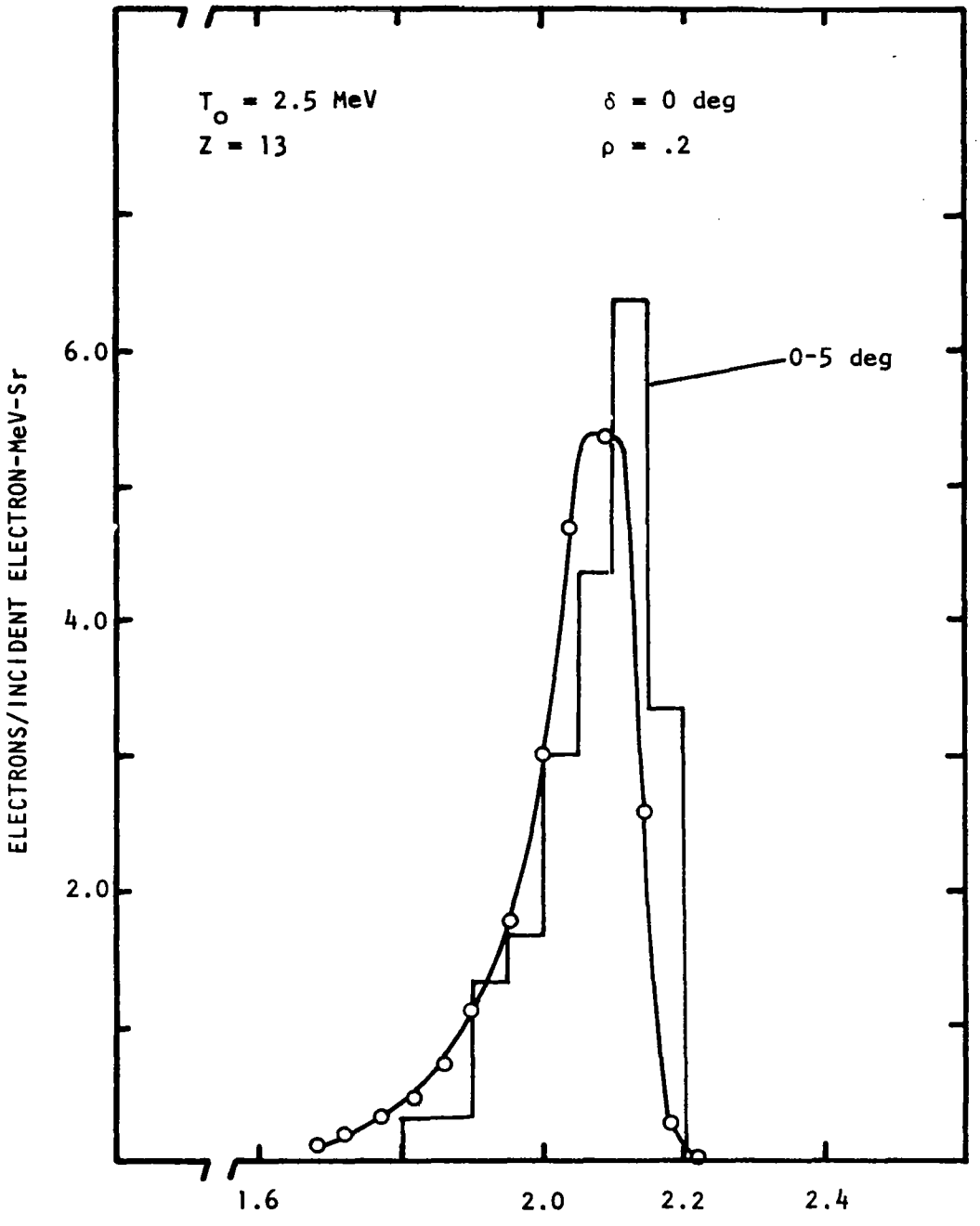
T_o = 2.5 MeV
Z = 13
δ = 0 deg
ρ = .2
0-5 deg
6.0
4.0
2.0
ELECTRONS/INCIDENT ELECTRON-MeV-Sr
1.6
2.0
2.2
2.4
ELECTRON ENERGY (MeV)

FIGURE 22

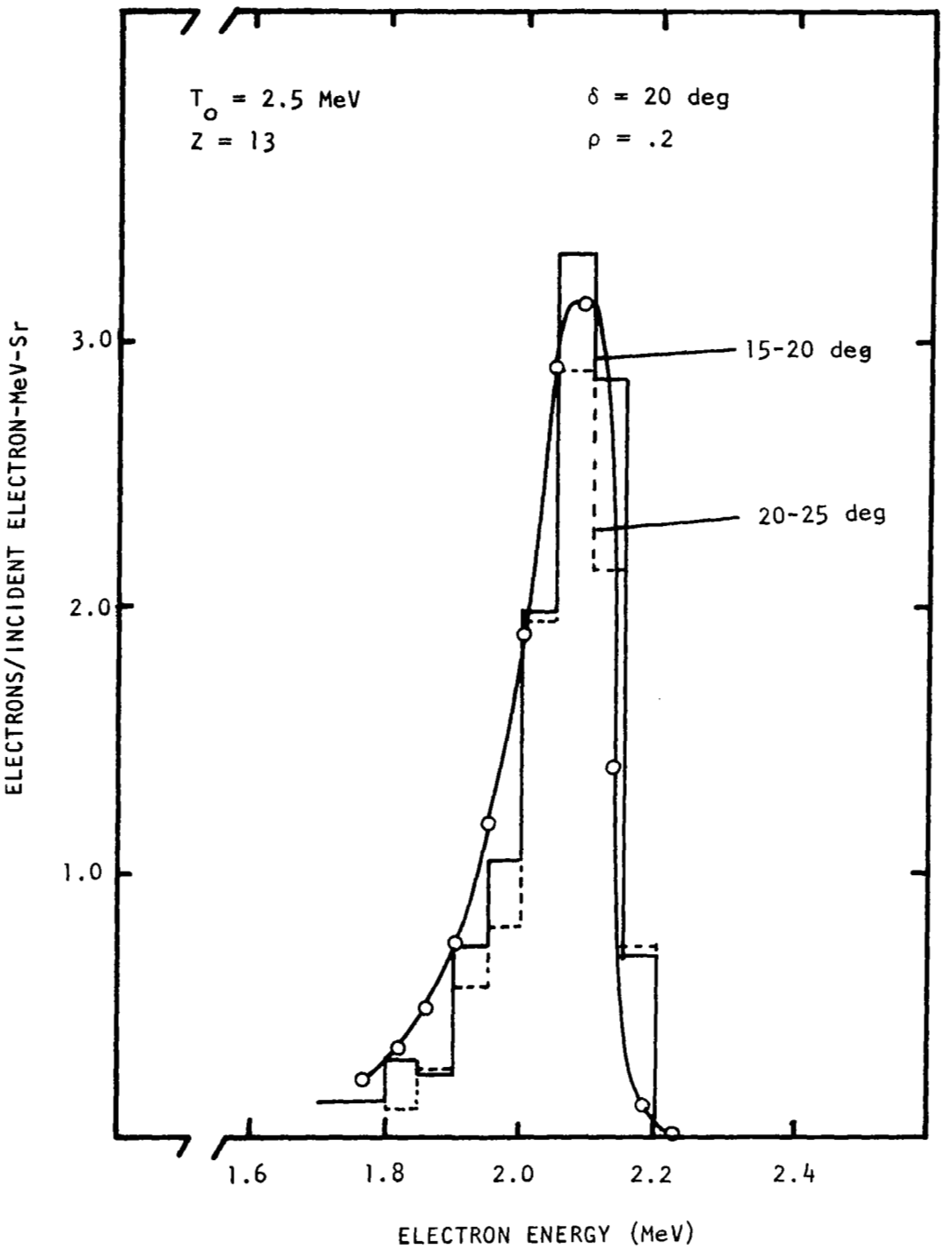
T_o = 2.5 MeV
Z = 13
δ = 20 deg
ρ = .2
15-20 deg
20-25 deg
ELECTRONS/INCIDENT ELECTRON-MeV-Sr
3.0
2.0
1.0
1.6
1.8
2.0
2.2
2.4
ELECTRON ENERGY (MeV)

FIGURE 23

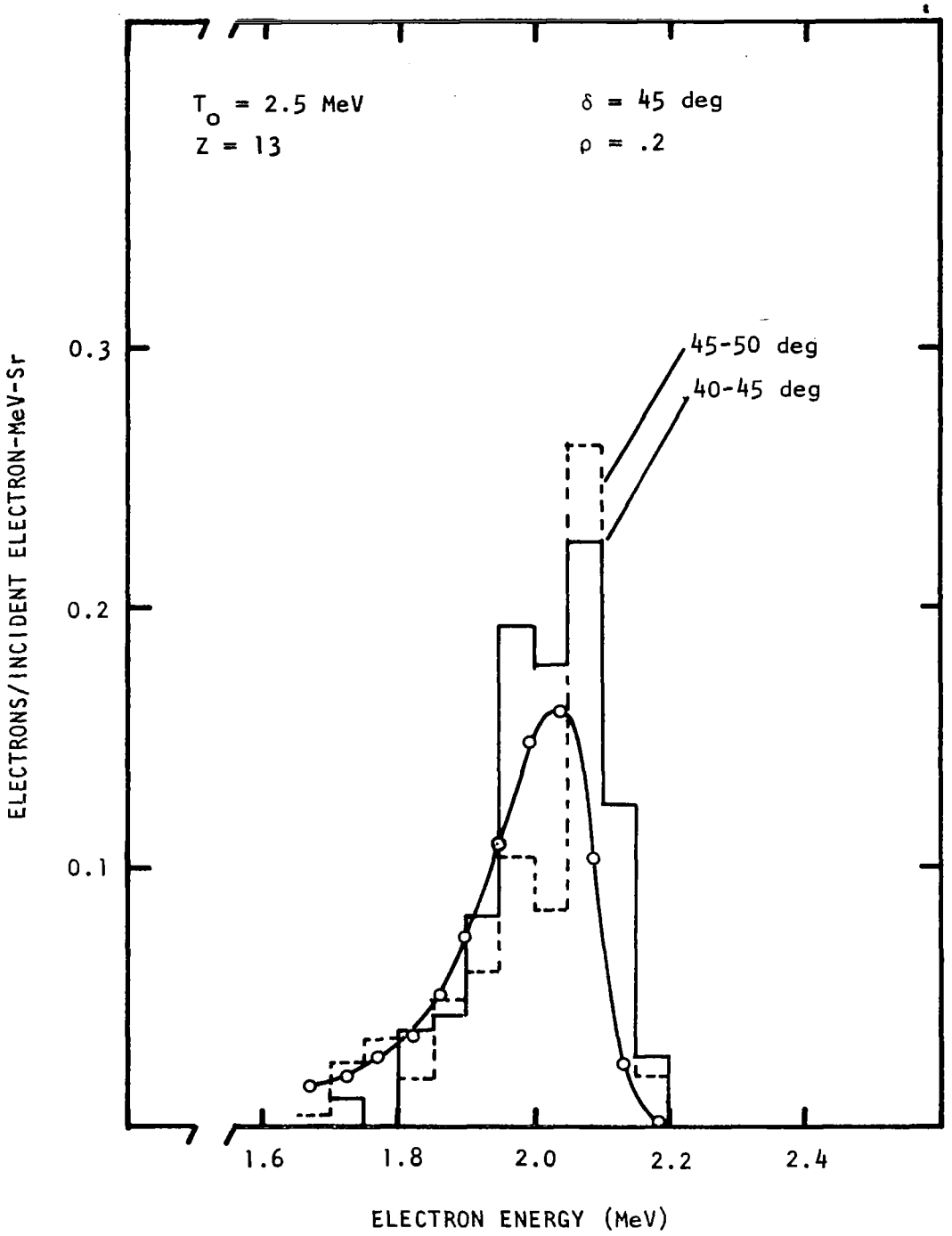
T_o = 2.5 MeV
Z = 13
δ = 45 deg
ρ = .2
45-50 deg
40-45 deg
0.3
0.2
0.1
ELECTRONS/INCIDENT ELECTRON-MeV-Sr
1.6
1.8
2.0
2.2
2.4
ELECTRON ENERGY (MeV)

FIGURE 24

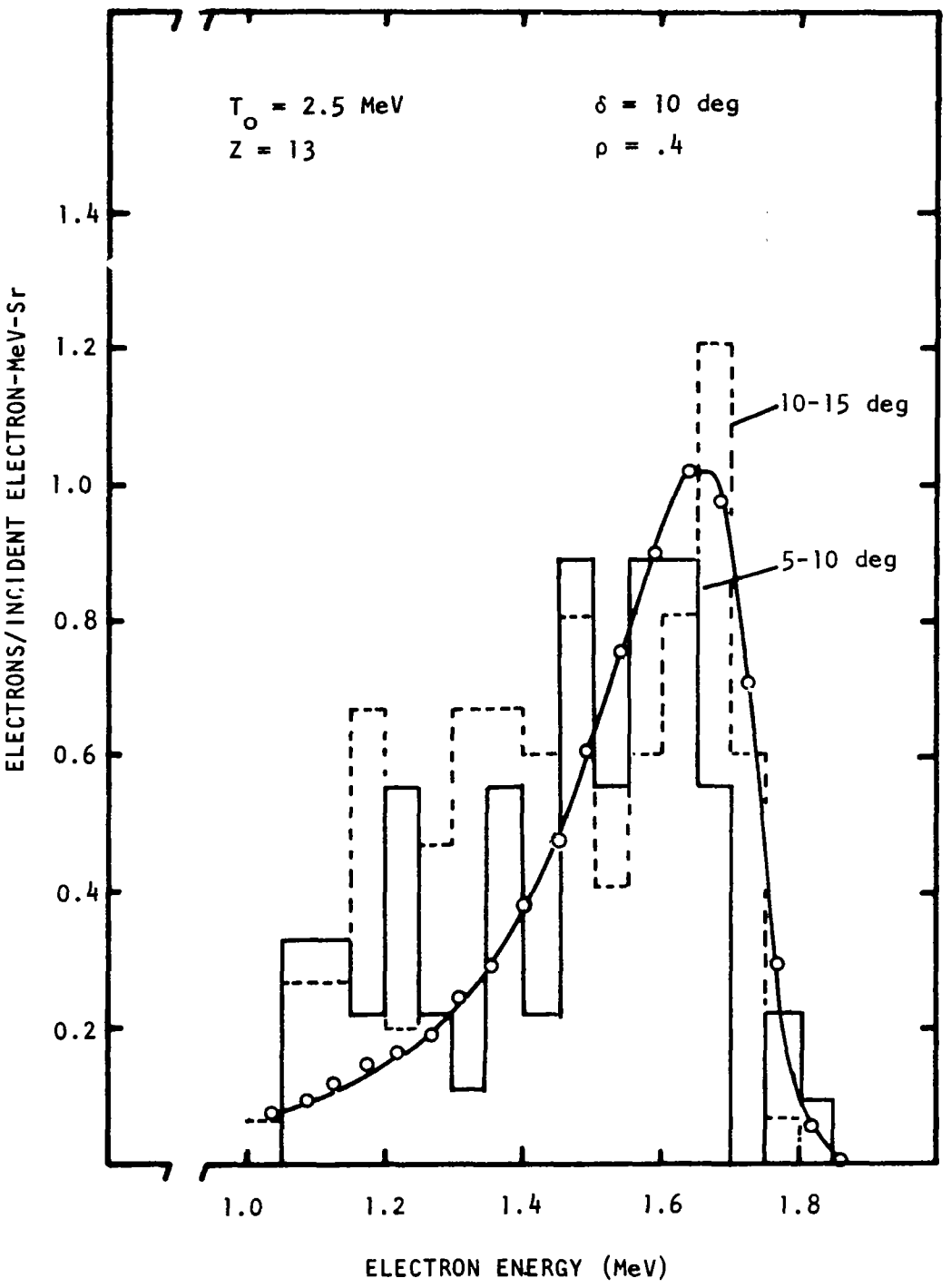
T_o = 2.5 MeV
Z = 13
δ = 10 deg
ρ = .4
10-15 deg
5-10 deg
ELECTRONS/INCIDENT ELECTRON-MeV-Sr
1.4
1.2
1.0
0.8
0.6
0.4
0.2
1.0
1.2
1.4
1.6
1.8
ELECTRON ENERGY (MeV)

FIGURE 25

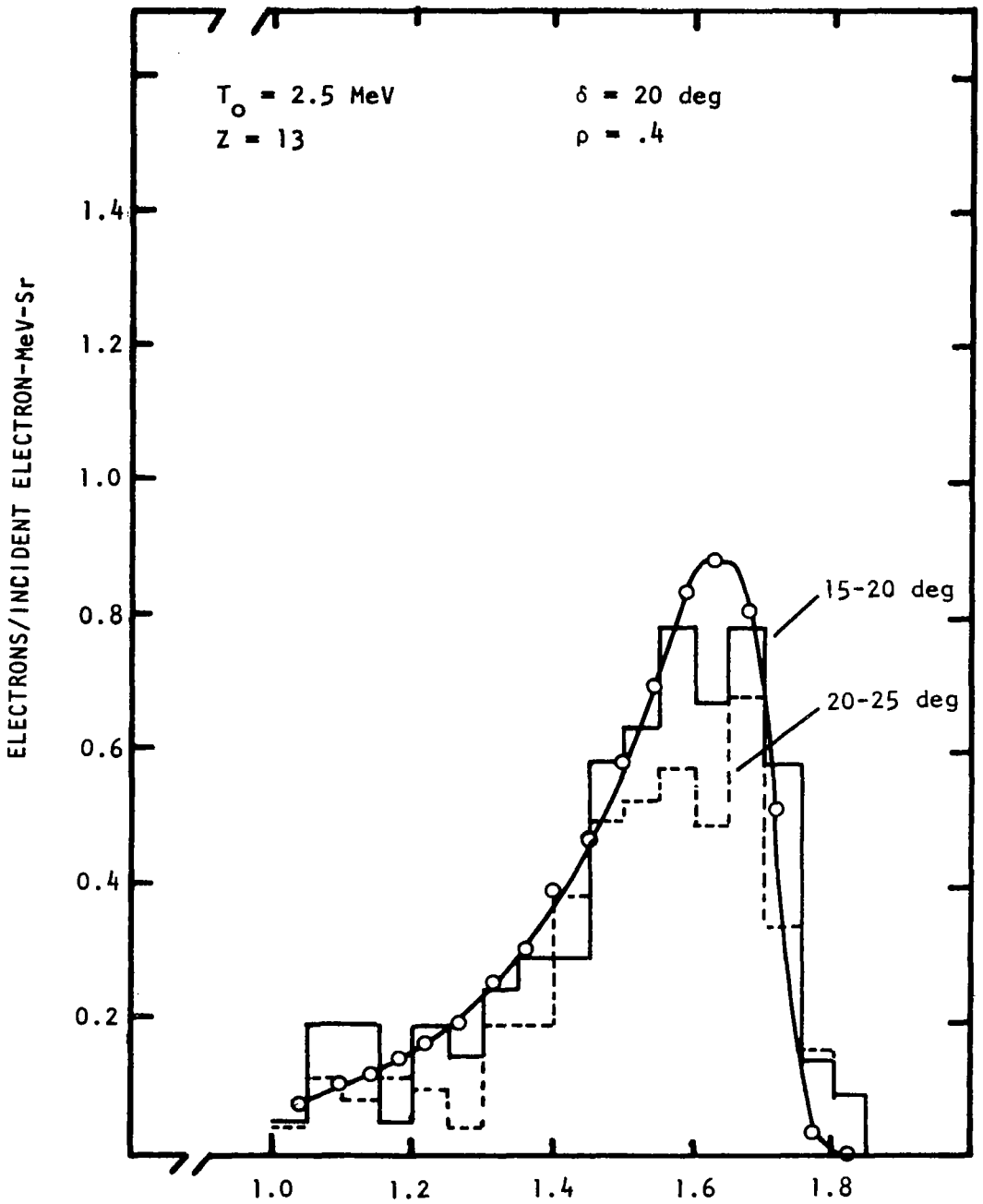
T_o = 2.5 MeV
Z = 13
δ = 20 deg
ρ = .4
15-20 deg
20-25 deg
ELECTRONS/INCIDENT ELECTRON-MeV-Sr
ELECTRON ENERGY (MeV)
1.4
1.2
1.0
0.8
0.6
0.4
0.2
1.0
1.2
1.4
1.6
1.8

FIGURE 26

PART IV

BREMSSTRAHLUNG PRODUCTION AND ELECTRON TRANSMISSION STUDIES FOR ELECTRON BEAMS OF NON-NORMAL INCIDENCE

BREMSSTRAHLUNG PRODUCTION AND ELECTRON TRANSMISSION STUDIES FOR ELECTRON BEAMS OF NON-NORMAL INCIDENCE

INTRODUCTION

Previous measurements of electron-bremsstrahlung production were carried out for the simplest experimental geometry, namely for normal incidence of the electron beam to the target plane. For this arrangement the resulting radiation pattern has axial symmetry with respect to the incident beam direction, and a series of measurements in one plane is sufficient to describe the external bremsstrahlung. A set of such measurements can be used to construct a total radiation spectrum and to obtain the total energy radiated from the target. A systematic study of electron-bremsstrahlung production for normal incidence on thick targets was reported in Part III of NASA Contract Report, NASA CR 1194.[1] Early electron diffusion studies were also limited to normal incidence of the electron beam to the target. The importance of these measurements like the bremsstrahlung measurements was that measurements in one plane could be combined to determine the properties of the total scattered electron distribution. Comparisons were made to computed spectra at specific points as a rigorous test of the computations; in addition, characteristics of the target radiation integrated over direction were obtained and compared to the calculations.

Measurements of bremsstrahlung production in more than one plane, which are required for determining the complete radiation pattern for non-normal electron incidence, are not practical with the present experimental arrangement because of the use of a massive, shielded NaI spectrometer as the bremsstrahlung detector. However, measurements of electron penetration and backscattering for an angle of non-normal incidence of 60 deg at 1.0 MeV bombarding energy on an Al target of thickness corresponding to 0.4 the range at 1.0 MeV were reported in Part I of NASA Contractor Report, NASA CR 1194.[1] In this experiment

accurate measurements in a 4π-geometry were possible because of the availability of Si(Li) spectrometers for charged particle detection. A Si(Li) spectrometer of active volume sufficient to absorb 1.0-MeV electrons can be fabricated from a cylindrical disc of Si less than a centimeter in diameter and two millimeters in thickness. Provision for accurately positioning these detectors in three dimensions can be made in a vacuum chamber of about the same size as is used for positioning the detectors in one plane.

Analysis of the measurements of electron scattering for an angle of non-normal incidence revealed that for many targets some features of the transmitted electron distributions are not as complex as might be expected. The angular distribution of transmitted electron number is very nearly axially symmetric around the normal to the target at the point of beam-target intersection, as for the case of normal incidence. Also the energy distributions are similar in shape as a function of angle of observation for fixed angle of incidence. As expected the total fraction of incident particles penetrating the target is less than for normal incidence, due to the increase in the backscatter fraction; however, the energy distributions are almost insensitive to the angle of incidence for many target thicknesses and target materials. The similarity in angular and energy distributions observed between normal and non-normal incidence is attributed to the fact that for a target thickness corresponding to 0.4 the range in Al at the incident energy a diffusion distribution of the electrons is established before penetration of the target occurs.

The bremsstrahlung pattern resulting from non-normal incidence, on the other hand, cannot be described so simply since bremsstrahlung emission occurs continuously as the electron flux undergoes slowing down in the medium, before and after diffusion occurs. Possible features of the radiation can be considered, however. Photons near the incident electron energy are emitted in a thin layer of the target on the side of electron incidence before the electron energy is

degraded, and are expected to be correlated with the incident beam direction. The efficiency for radiative emission by the electron is reduced as the electron energy is reduced so that even at low photon energies the correlation may still exist. In addition, attenuation is important for materials composed of elements of high atomic number and affects the externally observed radiation pattern strongly for angles of observation near the target plane.

Two different sets of measurements are reported below which add to the data previously reported. The first consists of measurements in one plane of bremsstrahlung spectra as a function of angle of observation for electron beams of 30-, 45-, and 60- deg incidence. The measurements were made at 1.0 and 2.0 MeV incident electron energies for targets of Al and Au of thicknesses corresponding to the mean ranges at these energies. The experimental results include the individual intensity spectra for comparison to the computed spectra when they become available. In addition, at 2.0 MeV incident electron energy, angular distributions of intensity for different energy increments of the photon spectrum have been reduced from the spectra for 30- and 60- deg incidence. The second consists of measurements of an adequate number of transmitted electron spectra at 1.0 MeV for various angles of electron incidence so that approximate total penetration spectra could be constructed for a cosine law source. A cosine law source is of interest since the electron flux seen by an incremental area of an object in an omnidirectional flux varies as the cosine of angle from the normal. The use of non-normal incidence measurements to obtain total penetration spectra for a cosine law source has been done for two targets of Al and for a Sn and a Au target. Comparison of the spectra constructed from the experimental data for the Al targets to the Monte Carlo spectra of Berger is included. The individual spectra and comparisons of the shapes at various angles of incidence are also given.

EXPERIMENTAL MEASUREMENTS AND RESULTS

The experimental procedure followed in carrying out the measurements has been described in NASA Contractor Reports CR 759[2] and 1194[1], as has been the method of analysis of the pulse height spectra. The bremsstrahlung distributions were measured with an anticoincidence dual crystal NaI spectrometer. Electron distributions were obtained with Si(Li) spectrometers. The electron beam used in the bombardment was obtained from a 3-MeV Van de Graaff accelerator.

Bremsstrahlung Studies for Electron Beams of Non-normal Incidence

Bremsstrahlung spectra for targets of Al and Au have been obtained at bombarding energies of 1.0 and 2.0 MeV. Target orientations were used for angles between the normal to the target and the beam direction of ψ = 30, 45, and 60 deg at both energies. Target thicknesses of one mean range were employed at each energy and no corrections for attenuation effects in the targets were made. The photon intensity distributions are given in Figs. 7-32. The angles θ of observation with respect to the incident beam are indicated in the figures. A sign convention has been adopted for θ with positive values labeling measurements at angles with respect to the incident beam direction such that the target normal on the transmission side of the target is at positive angle. In the data the effect of the target plane is observed. For example, at 30- deg incidence, ψ = 30 deg, the target plane occurs at the angle of observation θ = -60 deg. At observation angles near θ = -60 deg significant attenuation of the transmitted photon beam occurs. This is seen in Fig. 1 for Au. The figure is a plot of total photon number above 0.10 MeV per steradian per microcoulomb of electrons bombarding the target for the three target angles. At all photon transmission angles absorption occurs. On the reflection side of the target the yield rises rapidly and actually exceeds the yield at forward angles. The intensity spectra in Fig. 15 for ψ = 30 deg show that the loss in intensity is primarily

in the low photon region at θ = -30 and -45 deg, and that the intensity in this region increases at θ = -75 and -90 deg, on the reflection side of the target. Figure 2 shows a plot of photon number versus angle for Al, for which attenuation effects are much less important except in the immediate neighborhood of the target plane. The peak in the angular distribution for all three target orientations occurs at θ = 0 deg, or in the incident beam direction.

Plots of the angular distributions of intensity radiated in four 0.5-MeV increments of the photon spectra at 2.0 MeV bombarding energy are shown in Figs. 3-6. For Al, Figs. 3-4, the shapes of the distributions are very similar to that observed for total photon number at 1.0 MeV. For the Au targets, Figs. 5-6, symmetry about the incident beam direction can be seen for the interval 1.5-2.0 MeV, where attenuation in the target is only of small importance. Photon absorption in the target for the increment below 0.5 MeV is so great that at transmission angles the intensity in this region falls below that of the increment from 0.5-1.0 MeV. The shape of the angular distributions for Au below 1.5 MeV photon energy is largely determined by target absorption.

Comparison of the spectral distributions of radiation intensity for non-normal incidence to those previously reported for normal incidence indicates that the spectral distributions do not change appreciably with angle of incidence. The reduction in intensity, except for attenuation, is related quantitatively to the increase in the backscattered energy with angle of incidence. Therefore, it appears that a reasonably good approximation of the characteristics of the bremsstrahlung produced by electrons of any angle of incidence can be obtained by use of the spectra for normal incidence with intensity corrections applied which are based on the change in the backscattered energy with angle and the attenuation of the photon beam in the material.

The average experimental error estimated for the individual energy spectra is 10% in the photon energy region less than 80% of the end-point energy. This error arises from error in target and detector angles, from background which is not removed, and from beam current integration. In the photon energy region greater than 80% of the end-point energy the average error is estimated to be 30% because of additional uncertainty in response removal and statistical uncertainty. Essentially, the same estimate of error applies to the angular distributions of intensity, Figs. 3-6. The uncertainty in the highest energy group, 1.5-2.0 MeV photon energy, is estimated to be 30%. For some points, especially at larger angles, the uncertainty in this region may be as large as 50% because of the low yield recorded in the spectra. Below 0.5 MeV, the angular distributions suffer some uncertainty due to the electronic cutoff on the low energy end. This is more significant for Al than for Au and may result in a total error of 15% for the angular distributions.

Electron Transmission Studies for Electron Beams of Non-normal Incidence

A study of the angular and energy distributions of electrons scattered by an Al target of thickness corresponding to 0.4 the range in Al at 1.0 MeV oriented at 60 deg from an incident beam of electrons showed that the penetrating flux of electrons was very nearly axially symmetric with respect to the target normal. It can be generalized that measurements confined to one plane are adequate to specify the transmission distribution regardless of the angle of incidence of the incident particles for target thicknesses where a diffusion distribution is established. Measurements of the angular distributions of electrons in one plane penetrating an Al target and backscattering from it for three angles of incidence are shown in Fig. 33. The target thickness was equivalent to 0.4 the range ($\rho = 0.4$) at the incident energy of 1.0 MeV. The similarity of the shapes of the angular distributions of the transmission spectra is shown for angles of incidence $\delta = 0$, 30, and 60 deg. The plane in which measurements were made is defined by the target normal at the beam spot

value at $\rho = 0.5$ shown here in the direction of better agreement with the experiment. The experimental values shown in the figure were derived from the single measurement at each angle of incidence and an integration over angle of observation and energy. The integration was performed as discussed above by assuming that the angular distributions for non-normal incidence are the same as for normal incidence.

The energy distributions of transmitted electrons from a unit area for a unit unidirectional flux of incident electrons with all directions equally probable, cosine law source, are shown in Fig. 42 for two Al targets. The fractions of the incident number of π electrons which penetrated the targets for $\rho = 0.4$ and 0.56 are 0.41 and 0.21, respectively. Figure 43 shows a comparison to the computed spectra by Berger*, with the ordinate normalized to a single incident electron. The calculated transmission coefficients for $\rho = 0.40$ and 0.56 are 0.42 and 0.18. The experimentally determined transmitted energies are 0.23 MeV for $\rho = 0.4$ and 0.08 MeV for $\rho = 0.56$. The corresponding computed values are 0.216 MeV for $\rho = 0.4$ and 0.068 MeV for $\rho = 0.56$. The comparisons show good agreement between calculation and experiment. The differences which are observed are in the direction expected in view of the approximations made in constructing the experimental spectra.

Similar measurements for targets of Sn and Su have been made. A single target thickness for each element was used. The spectra obtained for various angles of incidence, observed in the direction perpendicular to the target are shown in Figs. 44-45. Comparisons of the shapes at 30 and 60 deg similar to those for Al at these angles are shown in Fig. 46. The variation of shape is less for these elements than for Al. The total penetration spectra are shown

---

* This data was computed at Marshall Space Flight Center by the Monte Carlo Program ETRAN 15 of M. J. Berger and S. M. Seltzer.

on the target and the incident beam direction. In the figure the target normals for the three angles of orientation are indicated by the arrows above the curves. The symmetry which exists for the transmitted flux is apparent. On the other hand, the symmetry which exists at δ = 0 deg for the backscattered flux is destroyed by non-normal incidence. The maxima for angles of incidence δ = 30 and 60 deg occur at angles which correspond to the angles of reflection. The angular scale at the bottom of the figure, which gives the angle with respect to the incident beam, is interpreted by considering the value of the angle ψ, with limits also indicated at the bottom of the figure. The half plane containing the normal is labeled by ψ = 0 deg, and the other half plane by ψ = 180 deg as shown in the diagram. The abscissa of the figure has been divided accordingly; however, the region ψ = 180 deg at the right is marked off with the angle θ decreasing from 180 deg as the figure is scanned from left to right.

An additional characteristic of the transmission spectra which was observed previously is that the energy distributions change only slightly with emission angle for a given target. There is a decrease in the value of the most probably energy of about 30 keV, for a target of thickness corresponding to 0.4 the range at 1.0 MeV, and a small increase in straggling with increasing angle. Thus, the total spectrum of penetrating electrons for an angle of incidence can be constructed accurately by using a "standard" angular distribution curve and the energy distribution at one of the angles of observation. The angular region most comparable to the total spectrum integrated over solid angle is the region between 30 and 50 deg. However, only small error is introduced by using the distributions measured at 0 deg with respect to the target normal, as was done in the present case.

Measurements for angles of incidence δ = 0, 15, 30, 45, 60, and 75 deg were made for targets of Al of thicknesses corresponding to

0.2, 0.4, and 0.56 the range in Al at 1.0 MeV. The spectra obtained from these measurements are shown in Figs. 34-39 for an angle of observation of the transmitted electron flux of 0 deg with respect to the target normal. The spectra for the case of the thinnest target, 0.2 the range at 1.0 MeV, vary in intensity with angle significantly more than those for the other two thicknesses. This behavior is not inconsistent with the shape of the angular distribution for normal incidence for this target thickness, which was found to be prominently peaked in the region of small angle. The construction of a penetrating spectrum due to a cosine law source by averaging over angles of incidence and outgoing angles was not attempted for the thinnest layer for these reasons. Comparisons of the shapes of the energy spectra for angles of incidence δ = 30 and 60 deg for the three Al targets are shown in Fig. 40. The spectra were normalized to the same maximum value at the most probable energy. There is a shift of about 60 keV in the peak energy and about a 50% broadening of the width of the distribution at half maximum.

In the present study to obtain transmission spectra for a cosine law source the variations of the measured energy distributions with incident angle have been folded into the integration over angle. However, the neglect of this detail by taking spectral shapes from the normal incidence studies would not introduce error so great as to make the resulting spectra useless, since the largest contribution for a cosine law source comes from the region of δ less than 60 deg. The region from 30 to 45 deg is most heavily weighted in the integration. The error is even smaller for targets of medium and high atomic number elements because the spectral shapes and intensities are less dependent on the angle of incidence.

The derived dependence of transmission of the two thicker Al targets and the Sn and Au targets on angle of incidence is shown in Fig. 41. Comparisons to early data of Berger[3] are shown to the experimental values for Al. More recent values of Berger alter his

in Fig. 47 for π incident particles. The procedure for constructing these spectra was the same as that employed in constructing the Al spectra. However, the angular distributions of transmitted electrons for the different atomic numbers were found experimentally to vary slightly. This variation with atomic number was taken into account in the integration process. The fraction of the incident particles transmitting the Au target was 0.31, with an energy transmission of 0.22 MeV, while the transmitted fraction for the Sn target was 0.07 with an energy transmission of .033 MeV.

The estimated average uncertainty of the individual spectra is 7%; however, additional considerations must be made in using the data. Error in the measurements due to uncertainties in target thickness is most important for thicker targets for which transmission is small. Statistical uncertainty and error due to background and response removal are important in spectral regions where the yield falls a factor of three below the maximum of the distribution. Errors due to uncertainties in the target angle and in the detector angle are largest where the slope of the angular distribution is large. Since approximations are made in synthesizing the penetration spectra due to the cosine law source, distortion of the resulting spectra is expected. The constructed spectra are shifted to higher energy and exhibit less straggling than the true spectra because of the approximations made, as indicated above.

REFERENCES

1. M. J. Berger, NBS Technical Note 187, "Transmission and Reflection of Electrons by Aluminum Foils", April 1, 1963.

FIGURE CAPTIONS

Fig. 1 Angular distributions of photon number above 0.10 MeV for bombardment of a Au target with 1.0-MeV electrons of incident angles of 30, 45, and 60 deg.

Fig. 2 Angular distributions of photon number above 0.10 MeV for bombardment of an Al target with 1.0-MeV electrons of incident angles of 30, 45, and 60 deg.

Fig. 3 Angular distributions of radiated intensity for four 0.5-MeV photon energy increments at an incident energy of 2.0 MeV.

Fig. 4 Angular distributions of radiated intensity for four 0.5-MeV photon energy increments at an incident energy of 2.0 MeV.

Fig. 5 Angular distributions of radiated intensity for four 0.5-MeV photon energy increments at an incident energy of 2.0 MeV.

Fig. 6 Angular distributions of radiated intensity for four 0.5-MeV photon energy increments at an incident energy of 2.0 MeV.

Fig. 7 Intensity distributions for an incident electron energy of 1.0 MeV.

Fig. 8 Intensity distributions for an incident electron energy of 1.0 MeV.

Fig. 9 Intensity distributions for an incident electron energy of 1.0 MeV.

Fig. 10 Intensity distributions for an incident electron energy of 1.0 MeV.

Fig. 11 Intensity distributions for an incident electron energy of 1.0 MeV.

Fig. 12 Intensity distributions for an incident electron energy of 1.0 MeV.

Fig. 13 Intensity distributions for an incident electron energy of 1.0 MeV.

Fig. 14 Intensity distributions for an incident electron energy of 1.0 MeV.

Fig. 15 Intensity distributions for an incident electron energy of 1.0 MeV.

Fig. 16 Intensity distributions for an incident electron energy of 1.0 MeV.

Fig. 17 Intensity distributions for an incident electron energy of 1.0 MeV.

Fig. 18 Intensity distributions for an incident electron energy of 1.0 MeV.

Fig. 19 Intensity distributions for an incident electron energy of 1.0 MeV.

Fig. 20 Intensity distributions for an incident electron energy of 1.0 MeV.

Fig. 21 Intensity distributions for an incident electron energy of 2.0 MeV.

Fig. 22 Intensity distributions for an incident electron energy of 2.0 MeV.

Fig. 23 Intensity distributions for an incident electron energy of 2.0 MeV.

Fig. 24 Intensity distributions for an incident electron energy of 2.0 MeV.

Fig. 25 Intensity distributions for an incident electron energy of 2.0 MeV.

Fig. 26 Intensity distributions for an incident electron energy of 2.0 MeV.

Fig. 27 Intensity distributions for an incident electron energy of 2.0 MeV.

Fig. 28 Intensity distributions for an incident electron energy of 2.0 MeV.

Fig. 29 Intensity distributions for an incident electron energy of 2.0 MeV.

Fig. 30 Intensity distributions for an incident electron energy of 2.0 MeV.

Fig. 31 Intensity distributions for an incident electron energy of 2.0 MeV.

Fig. 32 Intensity distributions for an incident electron energy of 2.0 MeV.

Fig. 33 Angular distributions of transmitted and backscattered electrons for 0-, 30-, and 60- deg incidence on an Al target of thickness corresponding to 0.4 the mean range at 1.0 MeV, $\rho = 0.4$.

Fig. 34 Transmission spectra for angles of incidence δ at 1.0 MeV bombarding energy. The detector was positioned to measure the transmitted electrons with momenta parallel to the normal to the target for an Al target of thickness corresponding to 0.2 the mean range in Al at 1.0 MeV.

Fig. 35 Transmission spectra for angles of incidence δ at 1.0 MeV bombarding energy. The detector was positioned to measure the transmitted electrons with momenta parallel to the normal to the target for an Al target of thickness corresponding to 0.2 the mean range in Al at 1.0 MeV.

Fig. 36 Transmission spectra for angles of incidence δ at 1.0 MeV bombarding energy. The detector was positioned to measure the transmitted electrons with momenta parallel to the normal to the target for an Al target of thickness corresponding to 0.40 the mean range in Al at 1.0 MeV.

Fig. 37 Transmission spectra for angles of incidence δ at 1.0 MeV bombarding energy. The detector was positioned to measure the transmitted electrons with momenta parallel to the normal to the target for an Al target of thickness corresponding to 0.40 the mean range in Al at 1.0 MeV.

Fig. 38 Transmission spectra for angles of incidence δ at 1.0 MeV bombarding energy. The detector was positioned to measure the transmitted electrons with momenta parallel to the normal to the target for an Al target of thickness corresponding to 0.56 the mean range in Al at 1.0 MeV.

Fig. 39 Transmission spectra for angles of incidence δ at 1.0 MeV bombarding energy. The detector was positioned to measure the transmitted electrons with momenta parallel to the normal to the target for an Al target of thickness corresponding to 0.56 the mean range in Al at 1.0 MeV.

Fig. 40 Comparisons for the three Al targets of the energy distributions for 30- and 60- deg incidence. The pairs of spectra are normalized to the same peak value.

Fig. 41 Transmission coefficients for the two thickest Al targets and the Sn and Au targets as a function of the angle of incidence. Comparisons to values obtained from early Monte Carlo calculations (ref. 1) are shown for the Al targets.

Fig. 42 The total penetration spectra constructed from non-normal incidence data for π incident electrons distributed in intensity as the cosine of the angle of incidence.

Fig. 43 Comparison of Monte Carlo calculated and experimentally derived transmitted energy distributions for Al targets. The source of electrons consisted of a 1.0-MeV beam with incident intensity varying as the cosine of the angle of incidence. Comparisons are made for targets corresponding to 0.4 and 0.56 the range at 1.0 MeV.

Fig. 44 Transmission spectra for a Sn target for various angles of incidence of a 1.0-MeV electron beam. Measurements were made with the detector measuring particles moving in the direction of the normal to the target. The data for 0 and 15-deg incidence were so similar as to be indistinquishable.

Fig. 45 Transmission spectra for a Au target for various angles of incidence of a 1.0-MeV electron beam. Measurements were made with the detector measuring particles moving in the direction of the normal to the target. The data for 0 and 15-deg incidence were so similar as to be indistinquishable.

Fig. 46 Comparisons of the shapes of the energy distributions at angles of incidence of 30 and 60 deg for the Sn and Au targets. The distributions are normalized to the same peak value. The variation of shape with angle of incidence for Sn and Au is small.

Fig. 47 The penetration spectra for the Sn and Au targets constructed from the non-normal incidence data to simulate a cosine law source for π incident electrons.

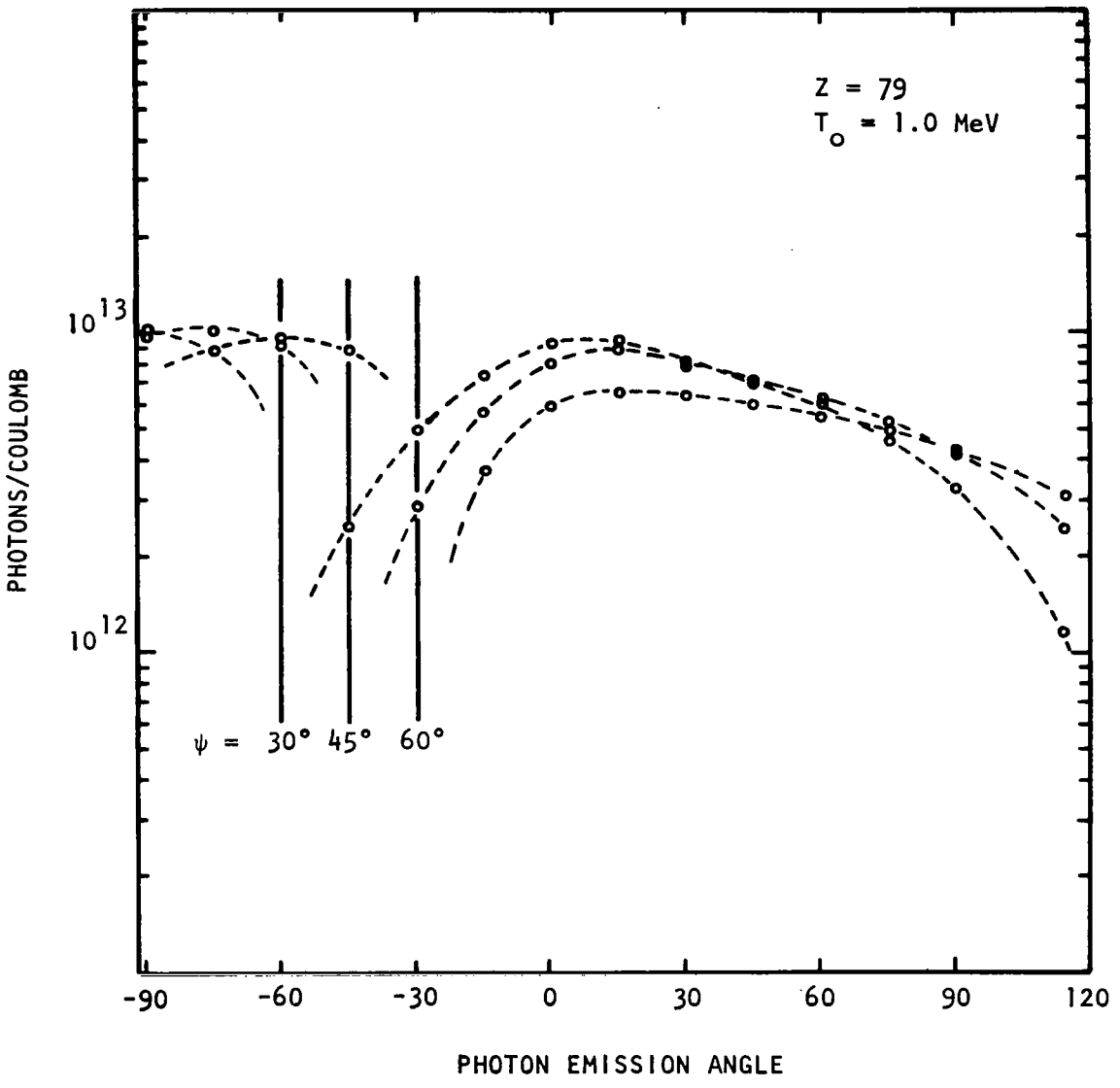
Z = 79
T_o = 1.0 MeV
10^{13}
10^{12}
PHOTONS/COULOMB
ψ = 30° 45° 60°
-90
-60
-30
0
30
60
90
120
PHOTON EMISSION ANGLE

FIGURE 1

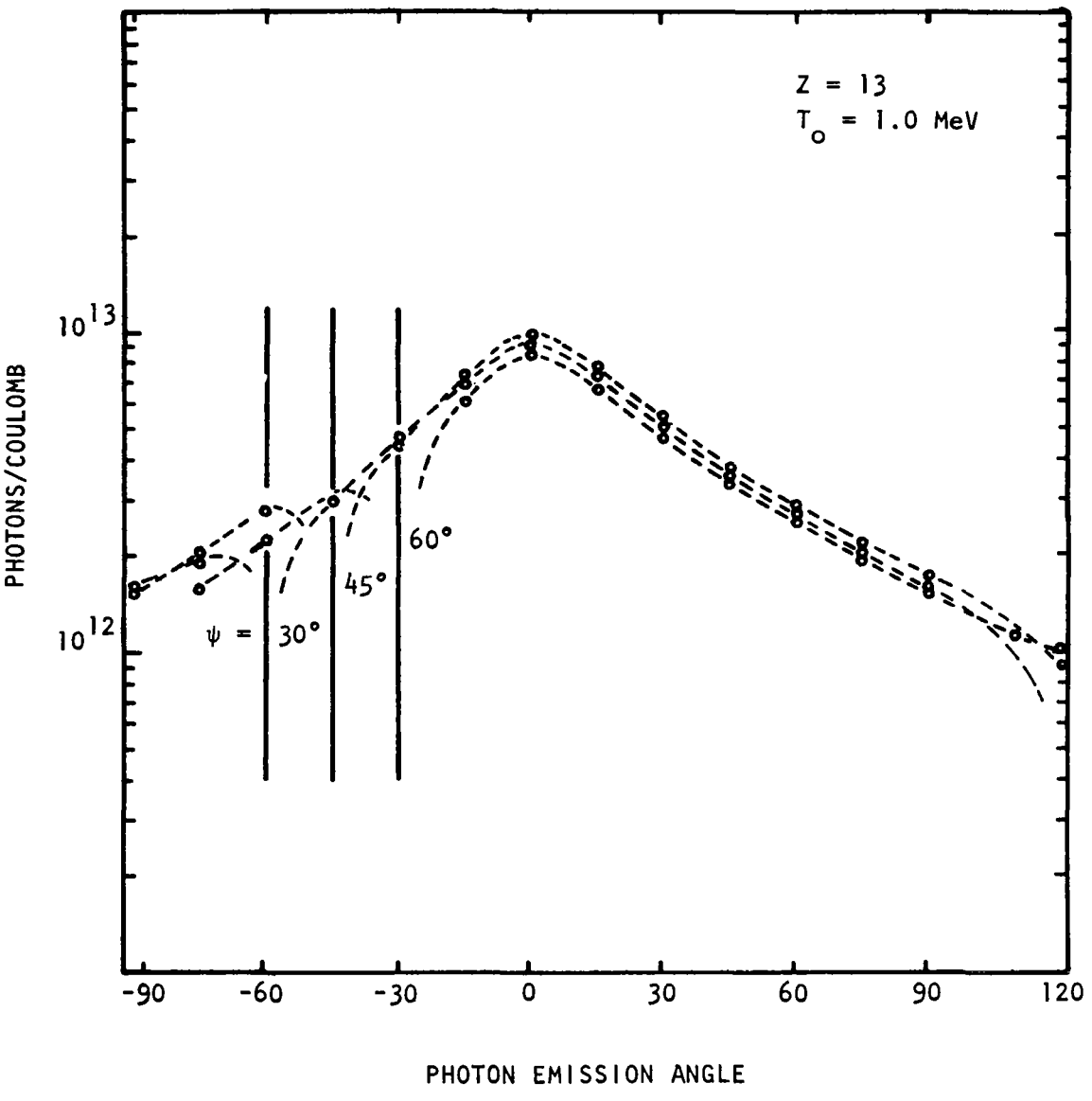
Z = 13
T_o = 1.0 MeV
10^{13}
10^{12}
PHOTONS/COULOMB
ψ = 30°
45°
60°
-90
-60
-30
0
30
60
90
120
PHOTON EMISSION ANGLE

FIGURE 2

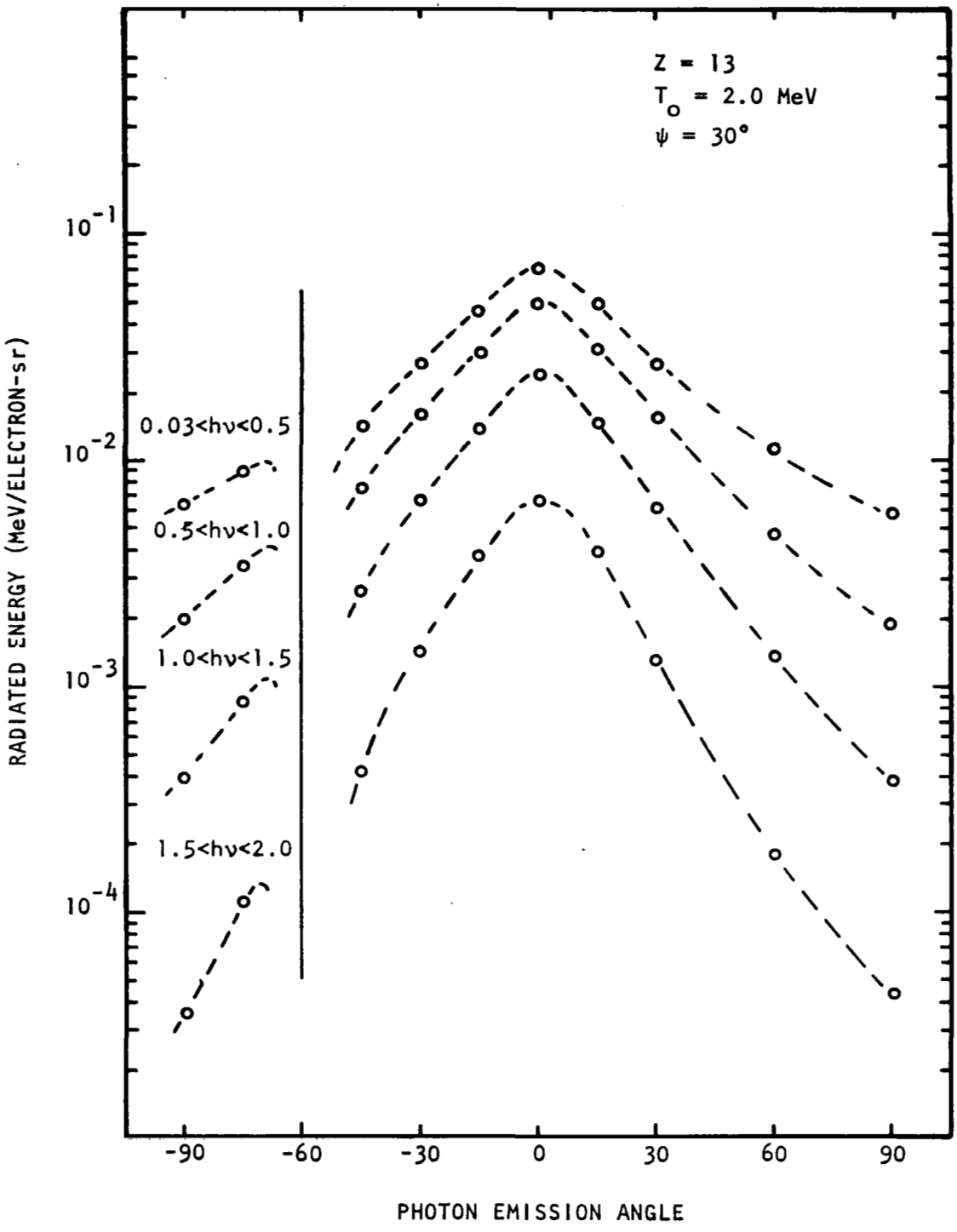
Z = 13
T_o = 2.0 MeV
ψ = 30°
10^{-1}
10^{-2}
10^{-3}
10^{-4}
0.03<hν<0.5
0.5<hν<1.0
1.0<hν<1.5
1.5<hν<2.0
-90
-60
-30
0
30
60
90
RADIATED ENERGY (MeV/ELECTRON-sr)
PHOTON EMISSION ANGLE

FIGURE 3

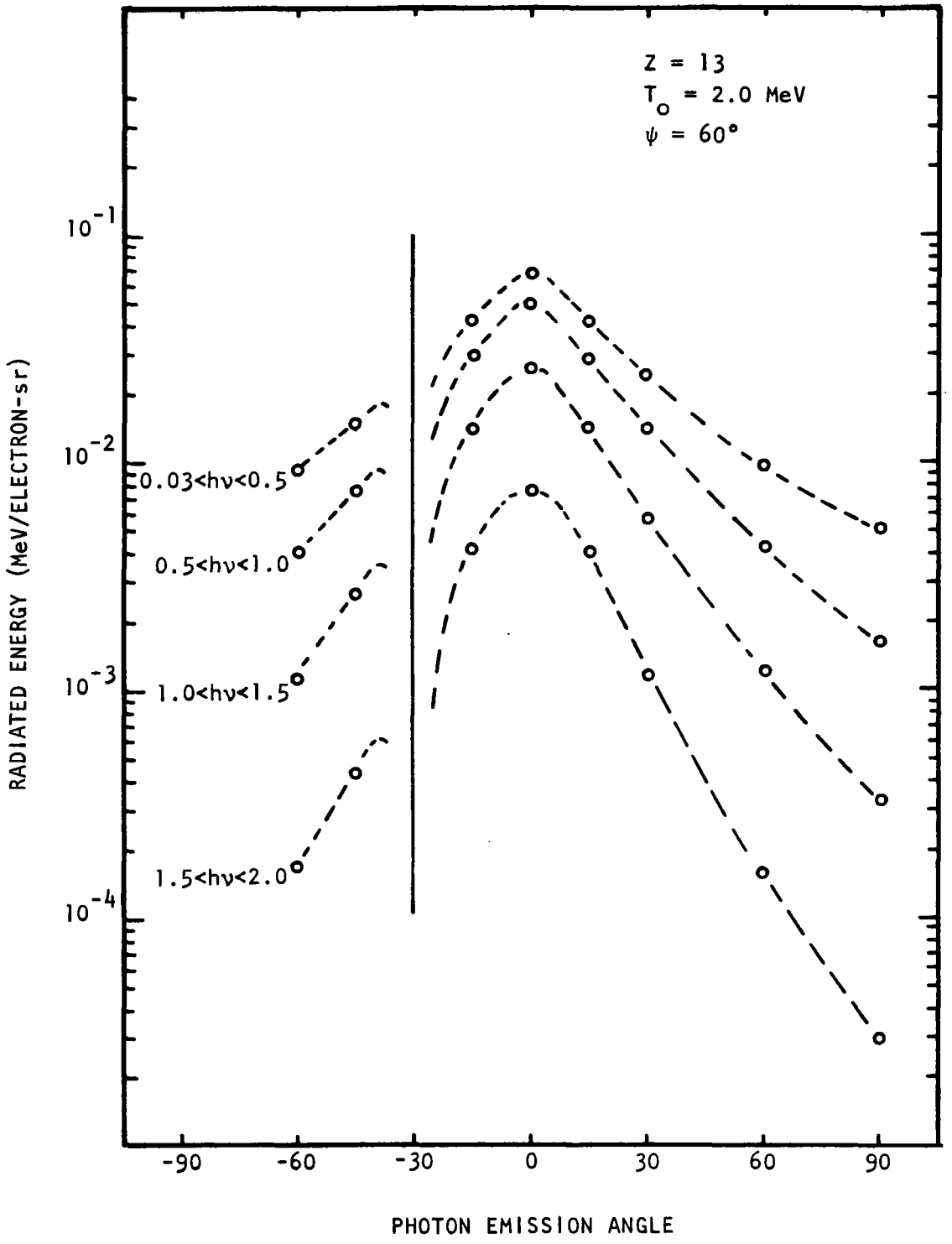
Z = 13
T_o = 2.0 MeV
ψ = 60°
10^{-1}
10^{-2}
10^{-3}
10^{-4}
0.03<hν<0.5
0.5<hν<1.0
1.0<hν<1.5
1.5<hν<2.0
RADIATED ENERGY (MeV/ELECTRON-sr)
-90
-60
-30
0
30
60
90
PHOTON EMISSION ANGLE

FIGURE 4

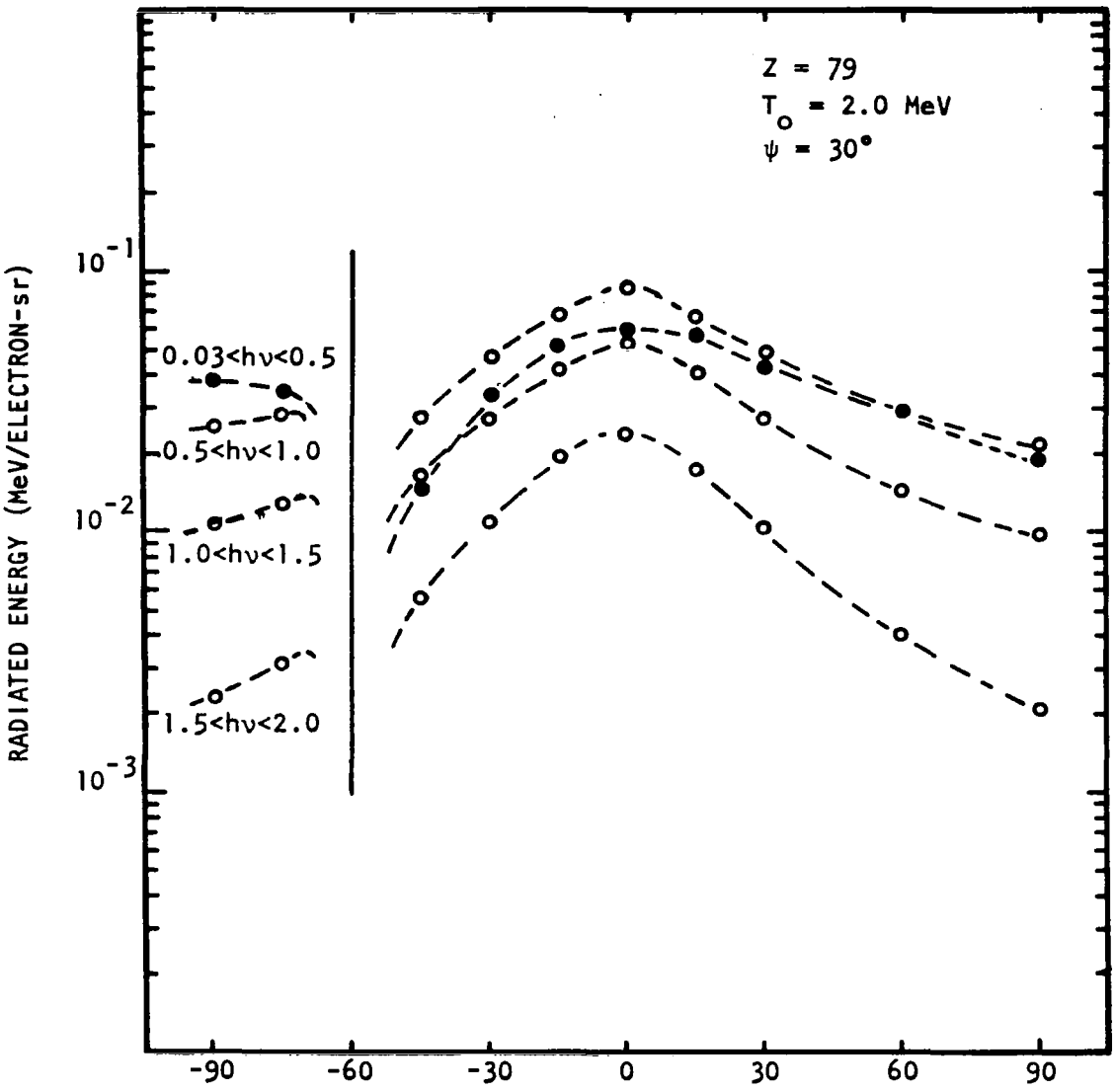
Z = 79
T_o = 2.0 MeV
ψ = 30°
10^-1
10^-2
10^-3
0.03<hν<0.5
0.5<hν<1.0
1.0<hν<1.5
1.5<hν<2.0
-90
-60
-30
0
30
60
90
RADIATED ENERGY (MeV/ELECTRON-sr)
PHOTON EMISSION ANGLE

FIGURE 5

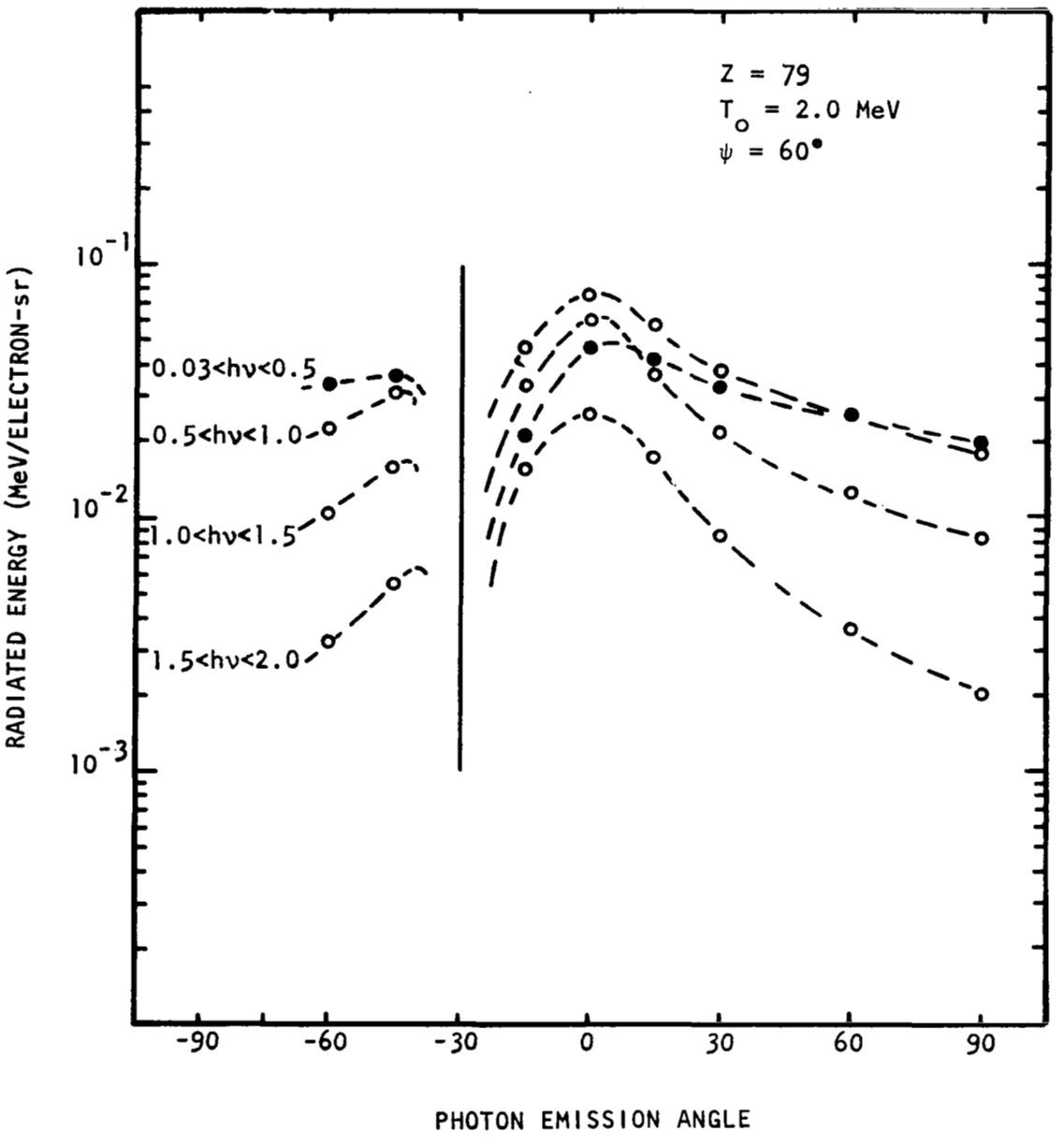
Z = 79
T_o = 2.0 MeV
ψ = 60°
10^{-1}
10^{-2}
10^{-3}
0.03<hν<0.5
0.5<hν<1.0
1.0<hν<1.5
1.5<hν<2.0
RADIATED ENERGY (MeV/ELECTRON-sr)
-90
-60
-30
0
30
60
90
PHOTON EMISSION ANGLE

FIGURE 6

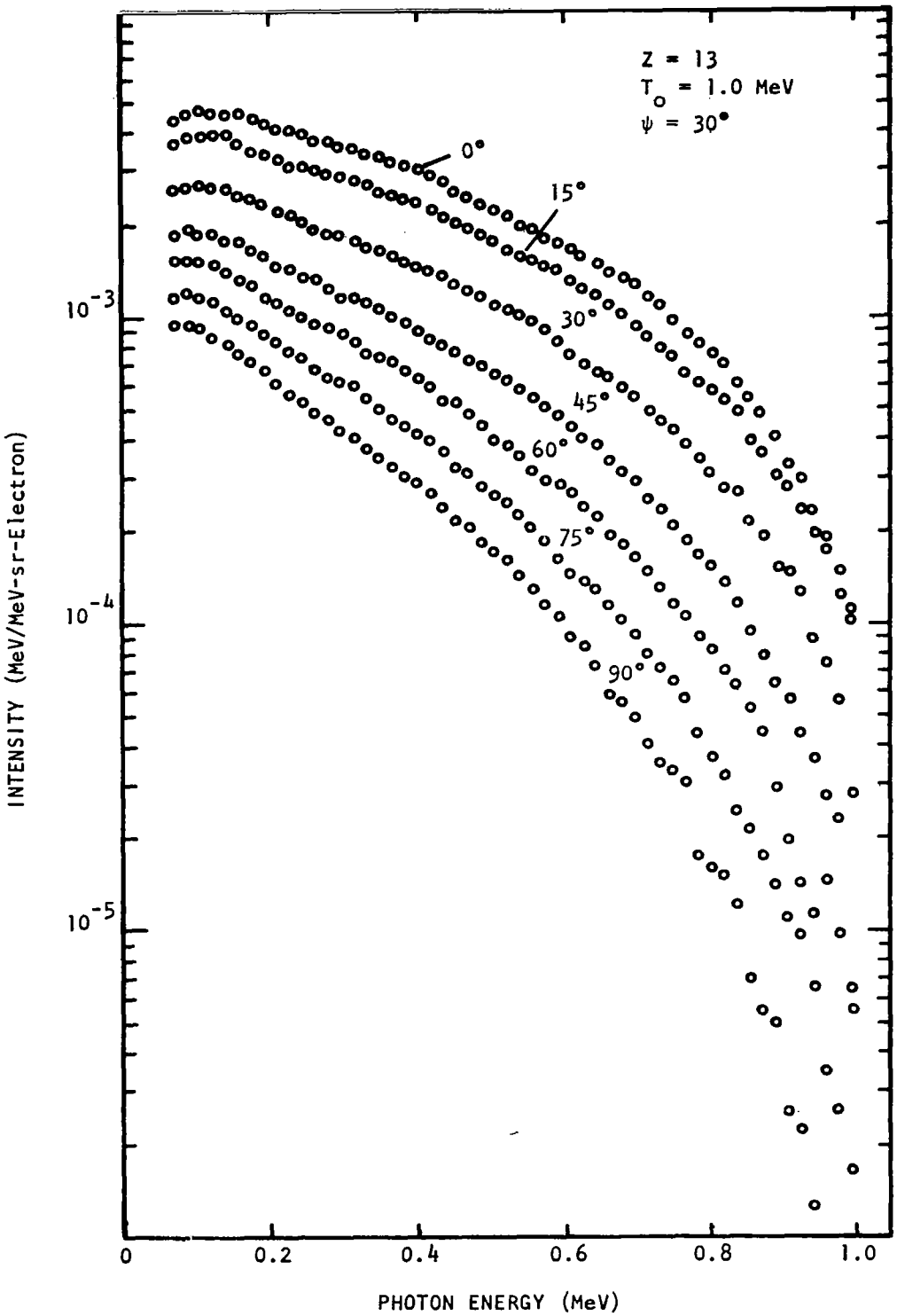
Z = 13
T_o = 1.0 MeV
ψ = 30°
0°
15°
30°
45°
60°
75°
90°
10^{-3}
10^{-4}
10^{-5}
INTENSITY (MeV/MeV-sr-Electron)
0
0.2
0.4
0.6
0.8
1.0
PHOTON ENERGY (MeV)

FIGURE 7

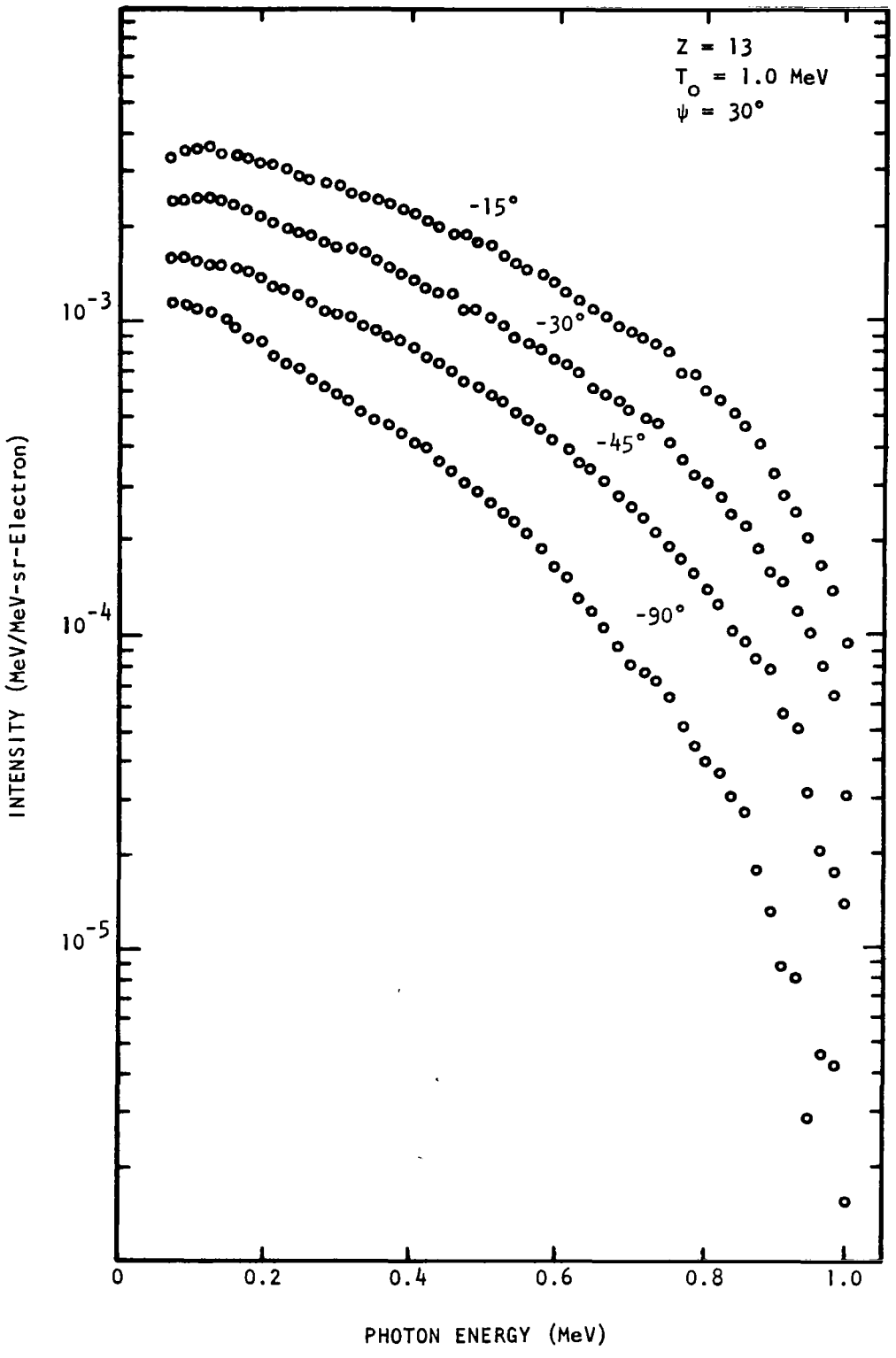
Z = 13
T_o = 1.0 MeV
ψ = 30°
-15°
-30°
-45°
-90°
10^{-3}
10^{-4}
10^{-5}
INTENSITY (MeV/MeV-sr-Electron)
0
0.2
0.4
0.6
0.8
1.0
PHOTON ENERGY (MeV)

FIGURE 8

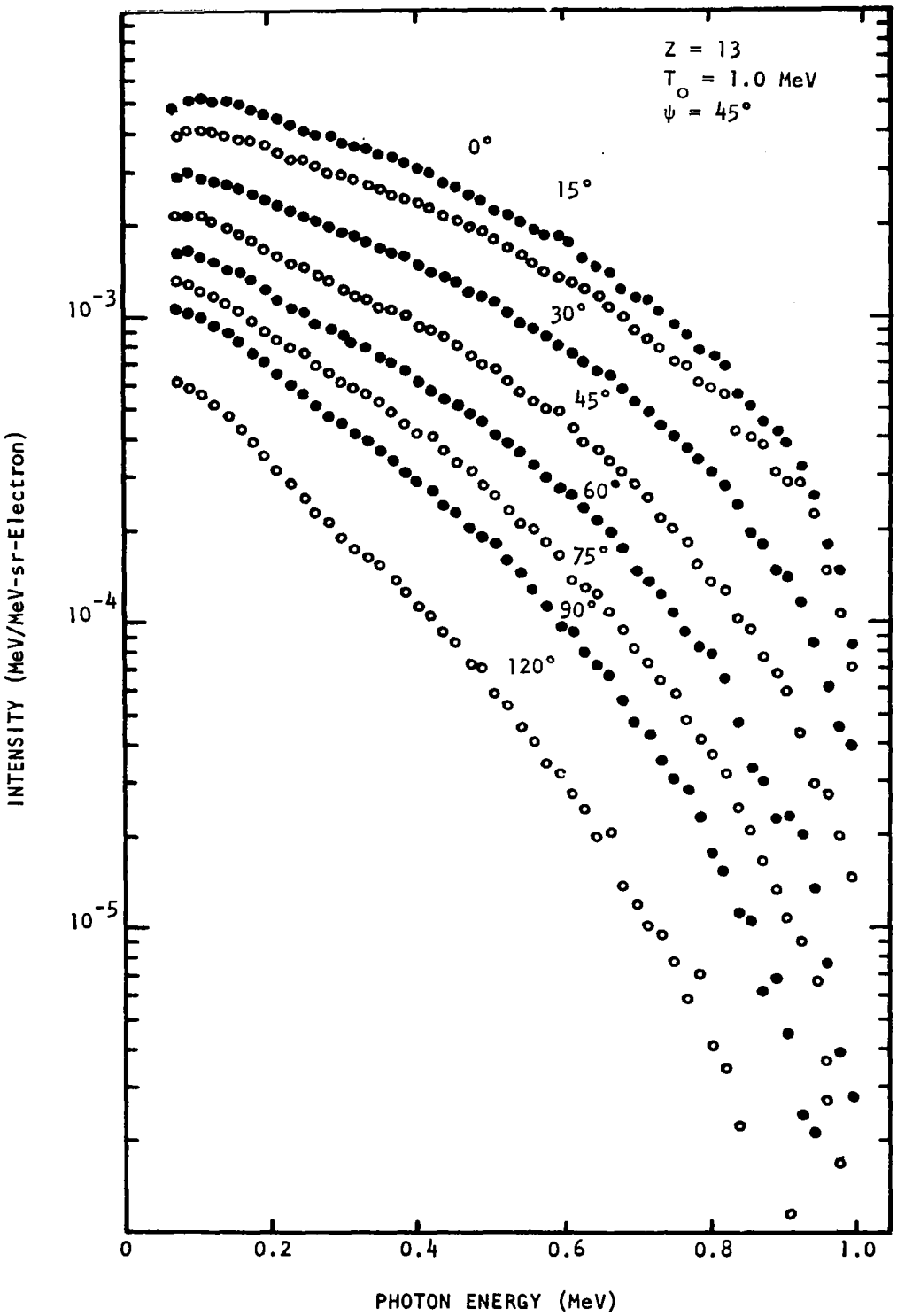
Z = 13
T$_o$ = 1.0 MeV
ψ = 45°
0°
15°
30°
45°
60°
75°
90°
120°
10^{-3}
10^{-4}
10^{-5}
INTENSITY (MeV/MeV-sr-Electron)
0
0.2
0.4
0.6
0.8
1.0
PHOTON ENERGY (MeV)

FIGURE 9

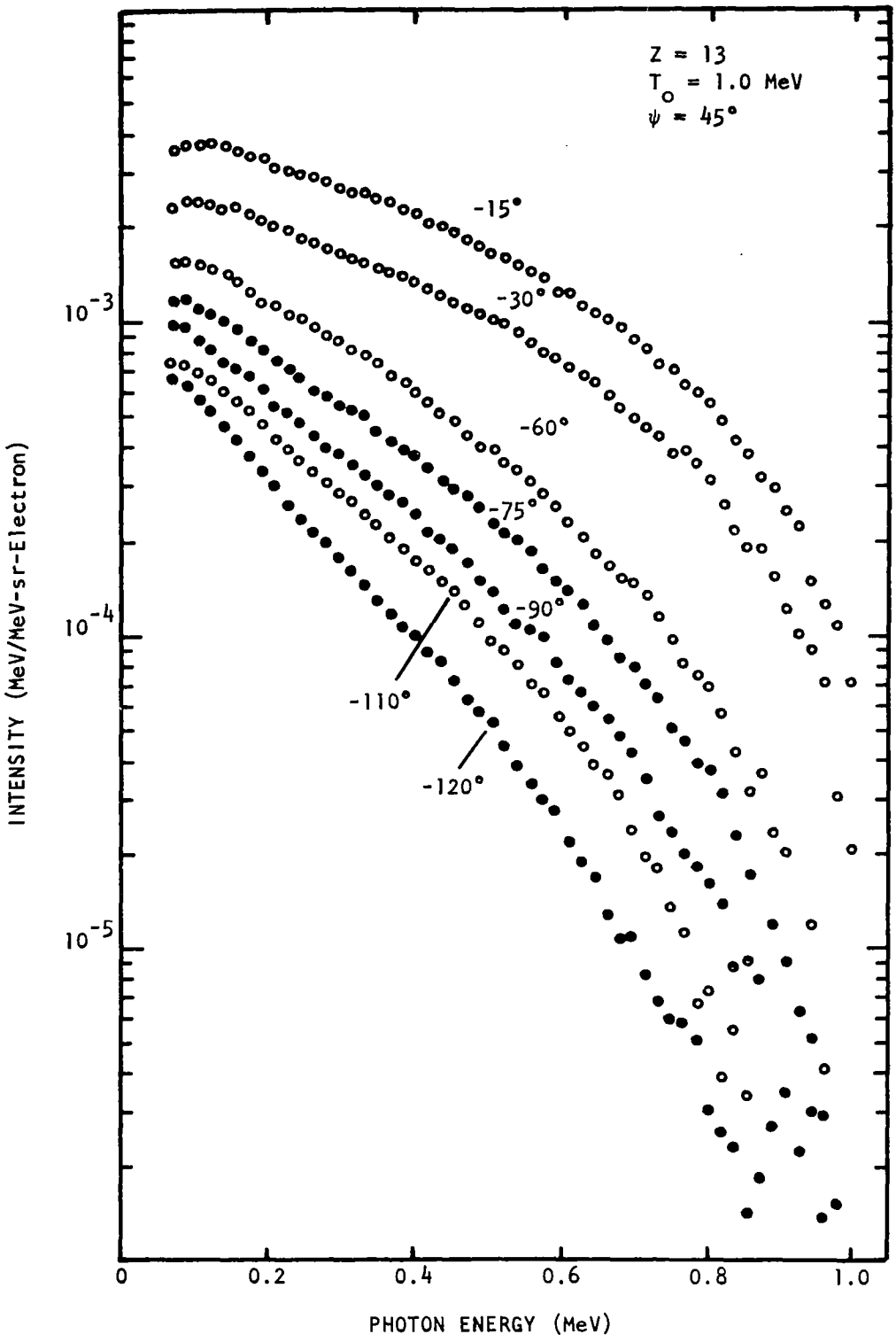
Z = 13
T$_o$ = 1.0 MeV
ψ = 45°
-15°
-30°
-60°
-75°
-90°
-110°
-120°
10^{-3}
10^{-4}
10^{-5}
INTENSITY (MeV/MeV-sr-Electron)
0
0.2
0.4
0.6
0.8
1.0
PHOTON ENERGY (MeV)

FIGURE 10

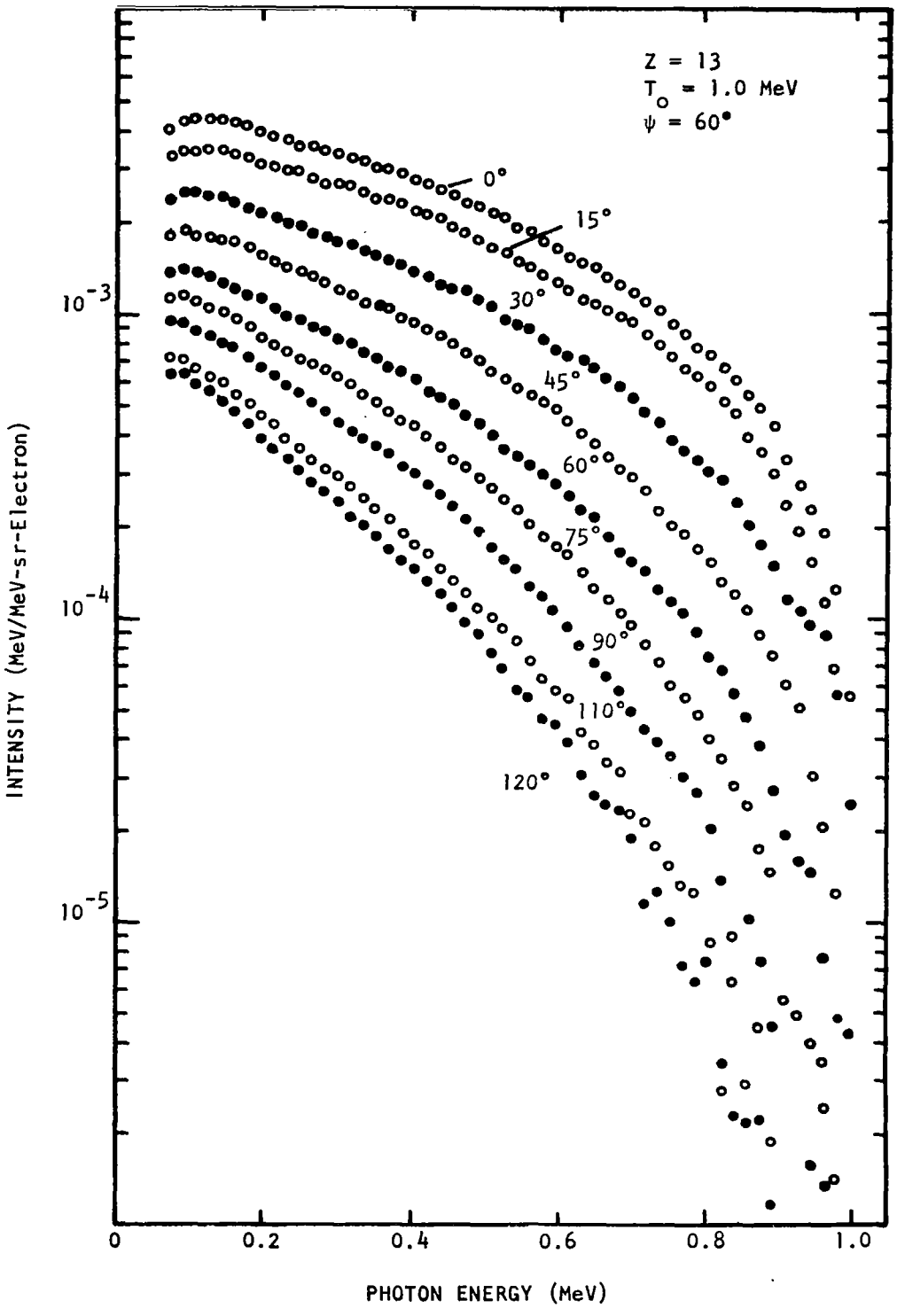
Z = 13
T$_o$ = 1.0 MeV
ψ = 60°
0°
15°
30°
45°
60°
75°
90°
110°
120°
10^{-3}
10^{-4}
10^{-5}
INTENSITY (MeV/MeV-sr-Electron)
0
0.2
0.4
0.6
0.8
1.0
PHOTON ENERGY (MeV)

FIGURE 11

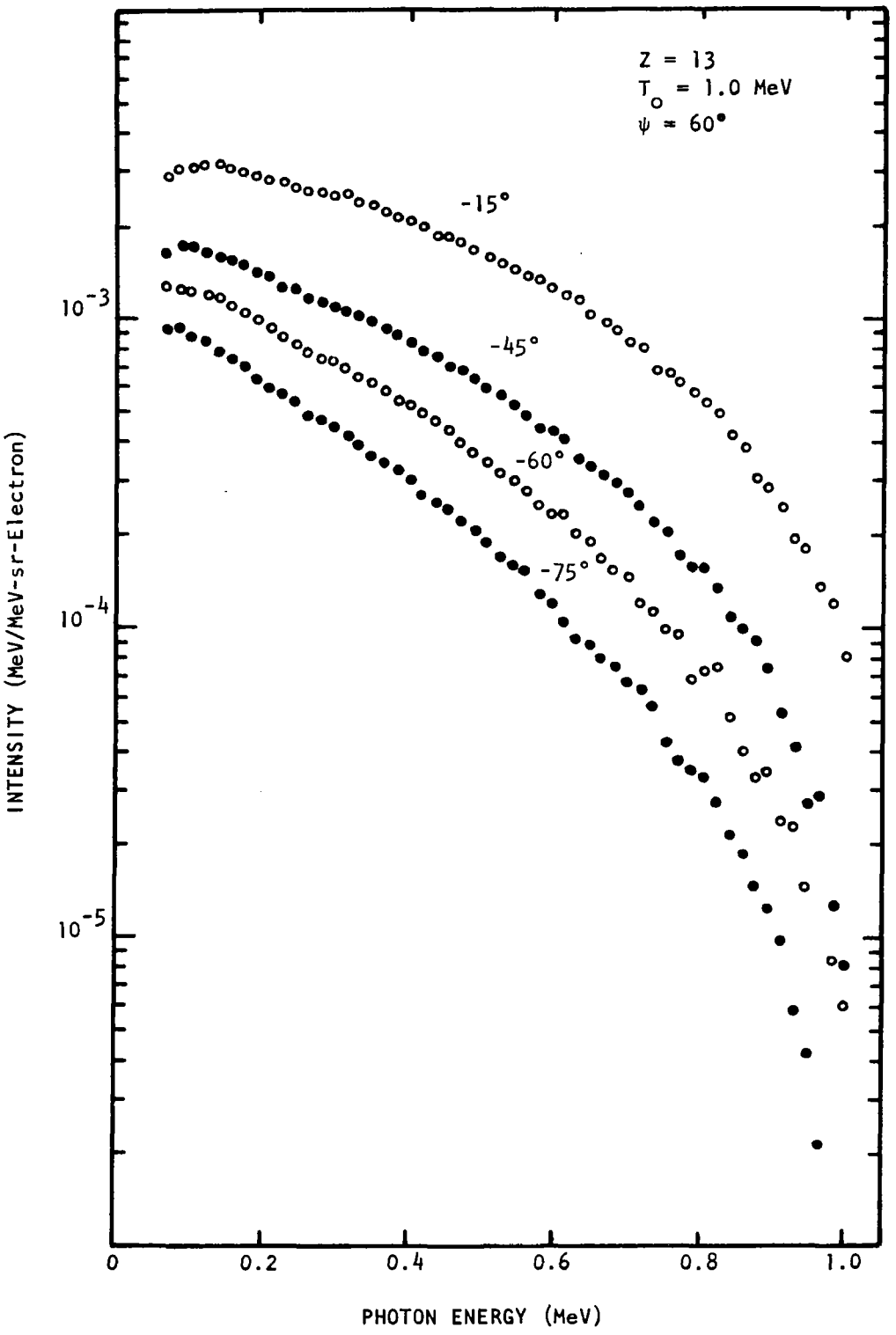
Z = 13
T_o = 1.0 MeV
ψ = 60°
-15°
-45°
-60°
-75°
10^-3
10^-4
10^-5
INTENSITY (MeV/MeV-sr-Electron)
0
0.2
0.4
0.6
0.8
1.0
PHOTON ENERGY (MeV)

FIGURE 12

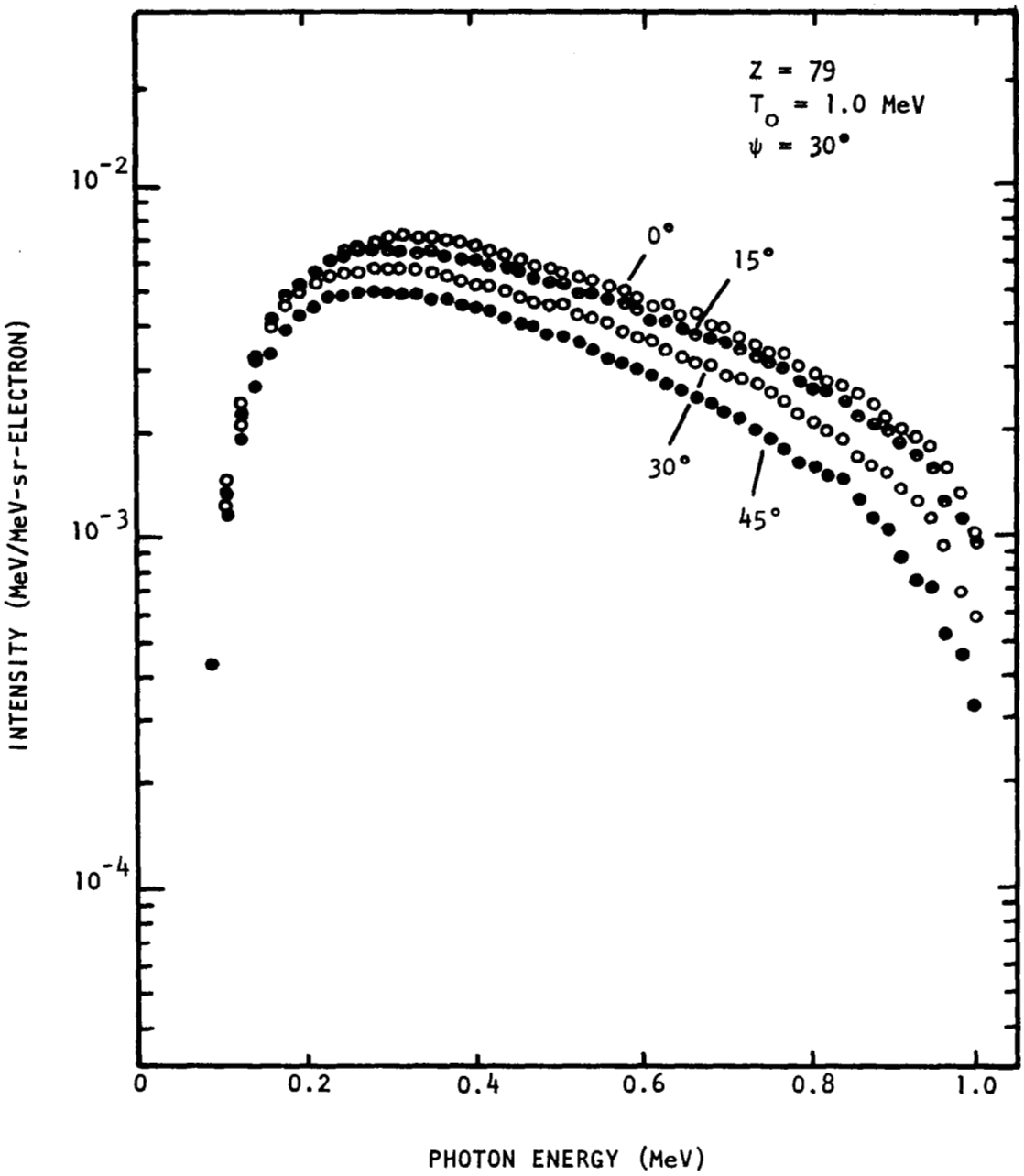
Z = 79
T_o = 1.0 MeV
ψ = 30°
0°
15°
30°
45°
10^-2
10^-3
10^-4
0
0.2
0.4
0.6
0.8
1.0
INTENSITY (MeV/MeV-sr-ELECTRON)
PHOTON ENERGY (MeV)

FIGURE 13

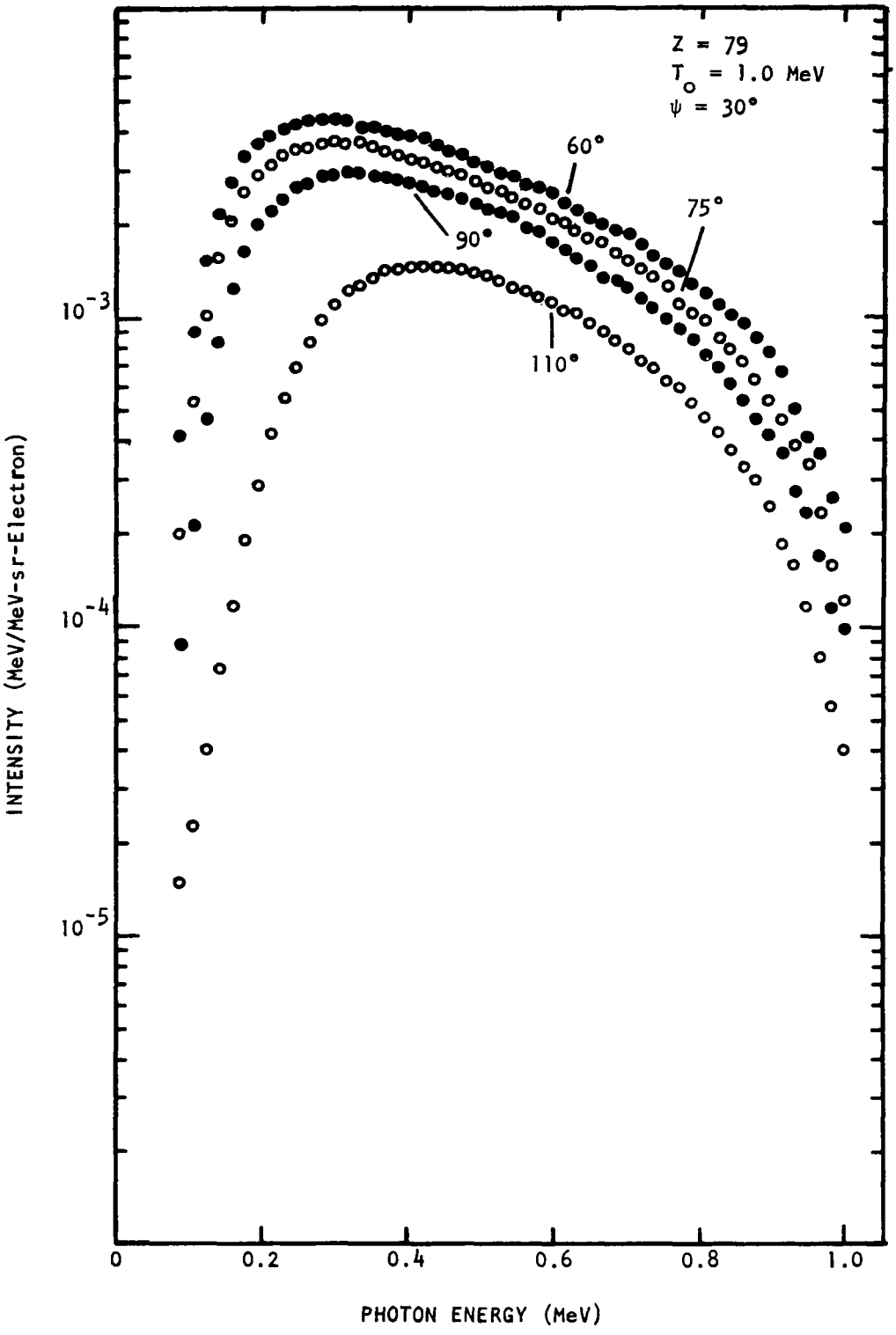
Z = 79
T_o = 1.0 MeV
ψ = 30°
60°
75°
90°
110°
10^{-3}
10^{-4}
10^{-5}
INTENSITY (MeV/MeV-sr-Electron)
0
0.2
0.4
0.6
0.8
1.0
PHOTON ENERGY (MeV)

FIGURE 14

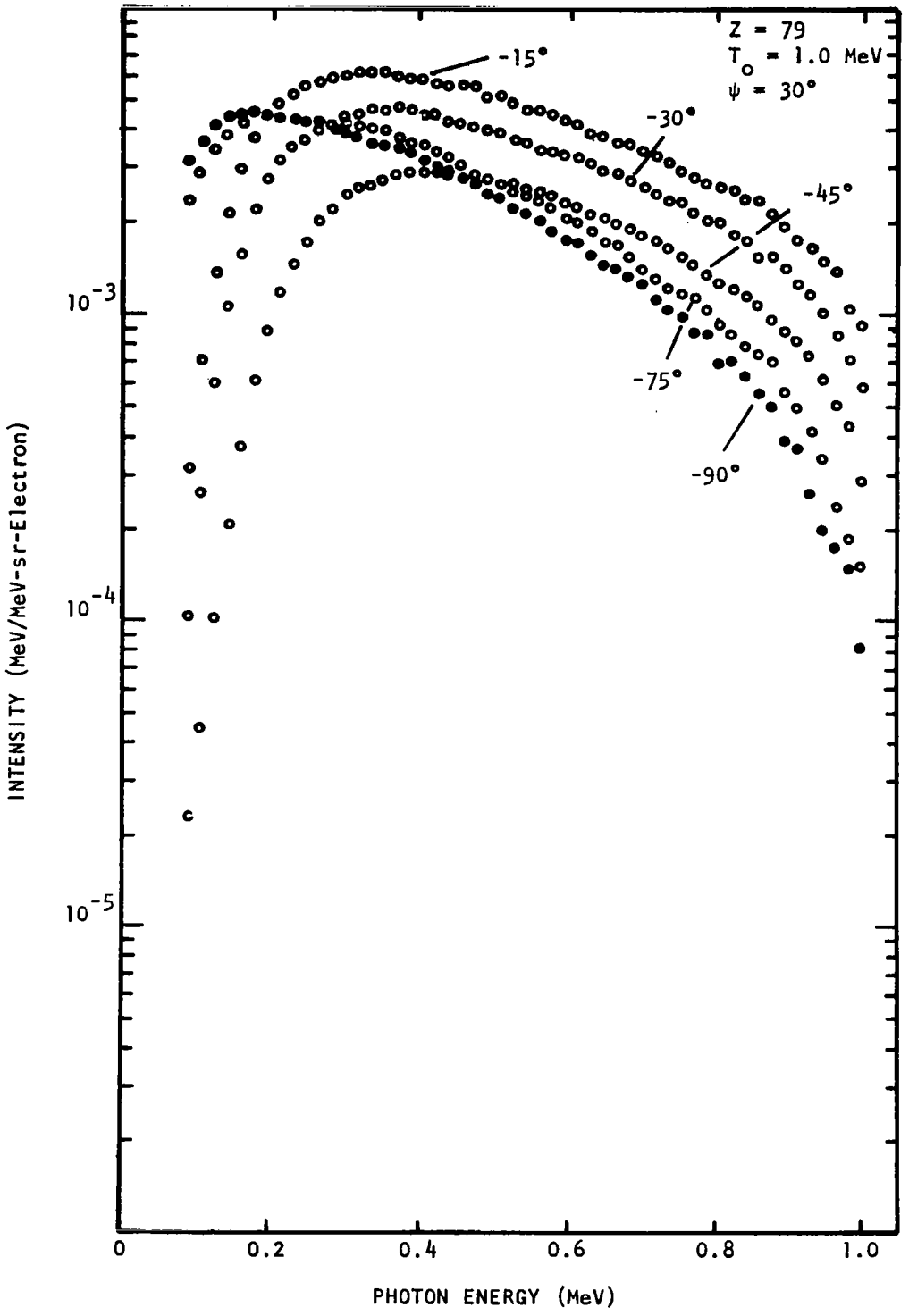
Z = 79
T_o = 1.0 MeV
ψ = 30°
-15°
-30°
-45°
-75°
-90°
10^-3
10^-4
10^-5
INTENSITY (MeV/MeV-sr-Electron)
0
0.2
0.4
0.6
0.8
1.0
PHOTON ENERGY (MeV)

FIGURE 15

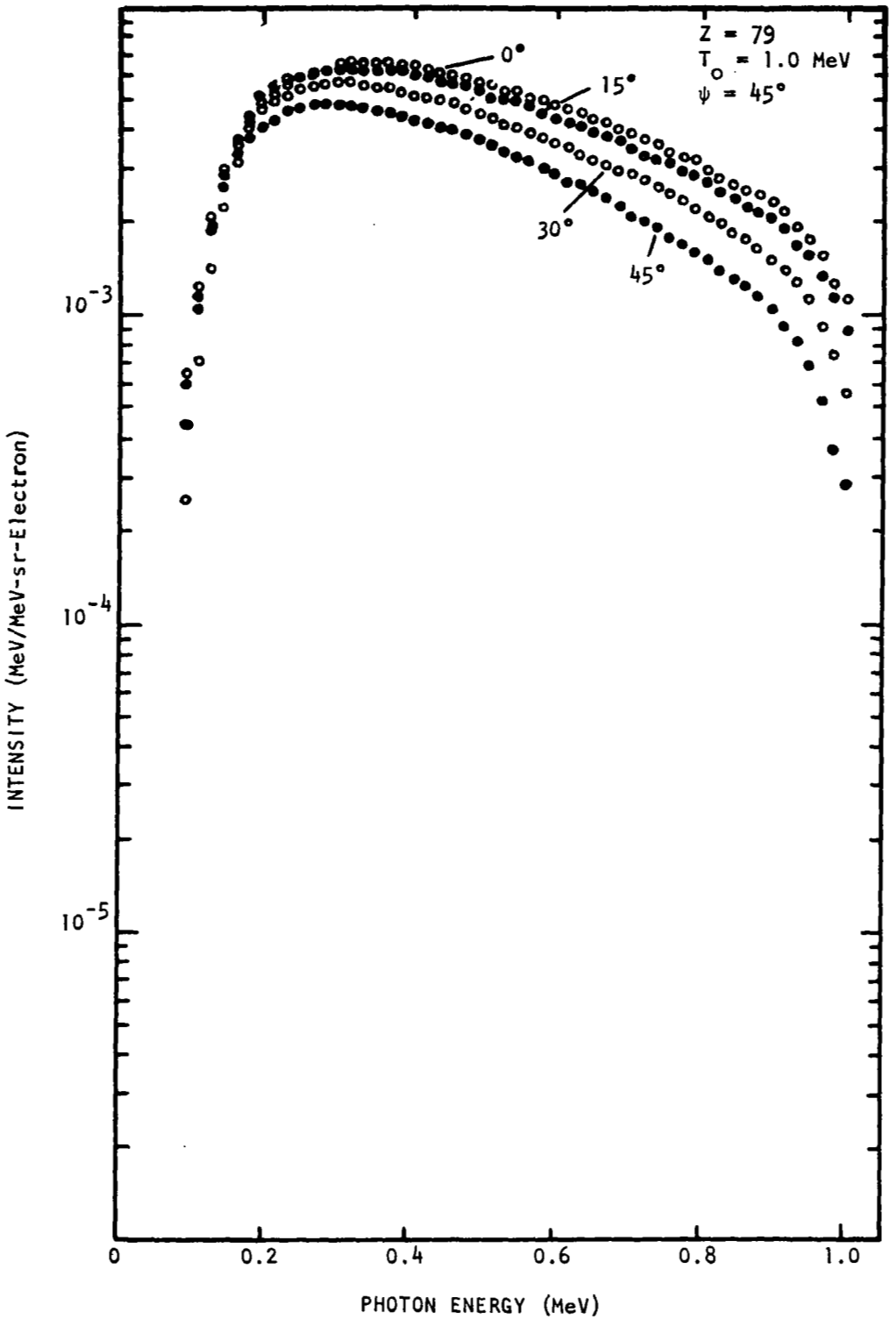
Z = 79
T$_o$ = 1.0 MeV
ψ = 45°
0°
15°
30°
45°
10^{-3}
10^{-4}
10^{-5}
INTENSITY (MeV/MeV-sr-Electron)
0
0.2
0.4
0.6
0.8
1.0
PHOTON ENERGY (MeV)

FIGURE 16

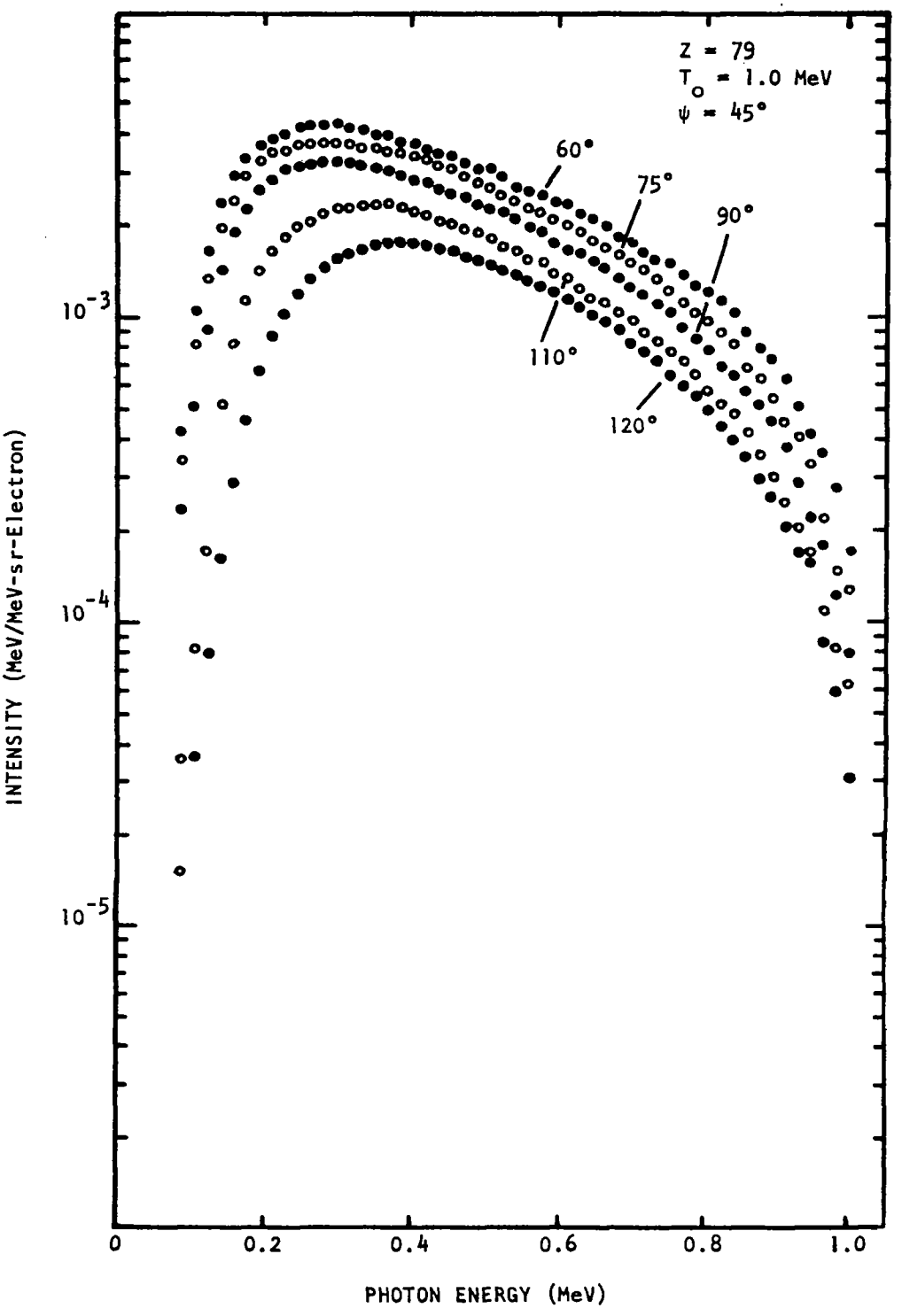
Z = 79
T_o = 1.0 MeV
ψ = 45°
60°
75°
90°
110°
120°
10^{-3}
10^{-4}
10^{-5}
INTENSITY (MeV/MeV-sr-Electron)
0
0.2
0.4
0.6
0.8
1.0
PHOTON ENERGY (MeV)

FIGURE 17

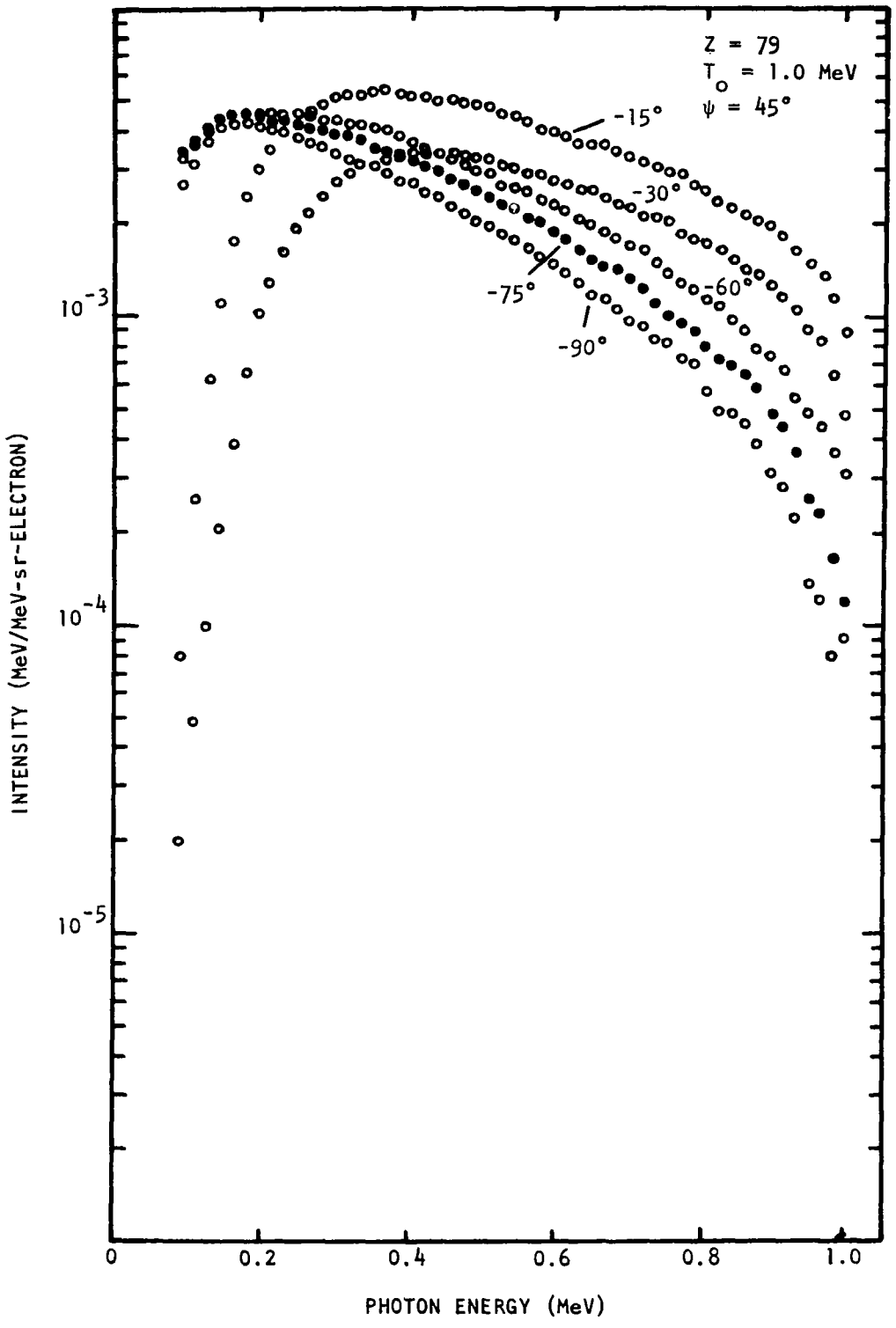
Z = 79
T_o = 1.0 MeV
ψ = 45°
-15°
-30°
-60°
-75°
-90°
10^-3
10^-4
10^-5
INTENSITY (MeV/MeV-sr-ELECTRON)
0
0.2
0.4
0.6
0.8
1.0
PHOTON ENERGY (MeV)

FIGURE 18

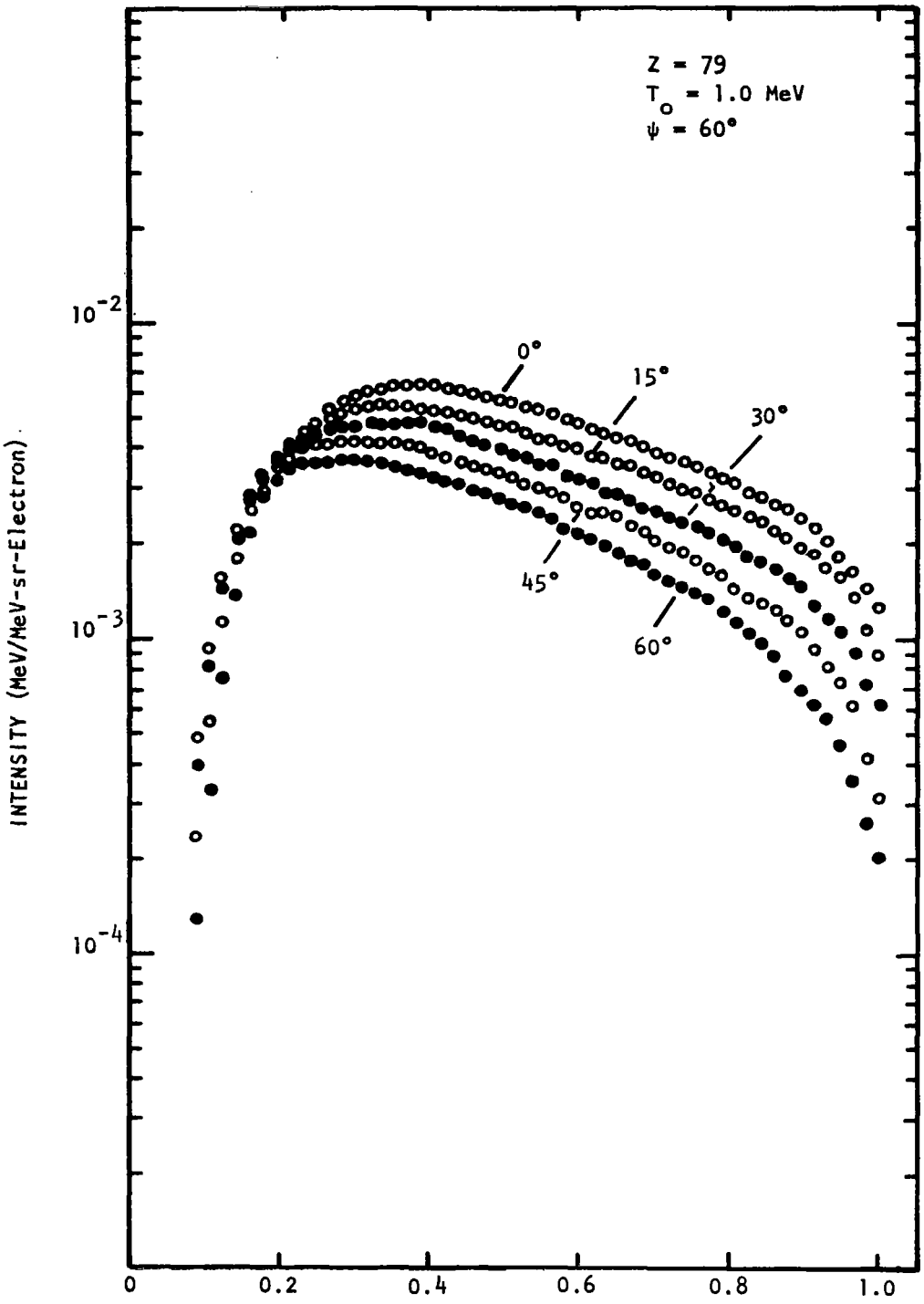
Z = 79
T_o = 1.0 MeV
ψ = 60°
0°
15°
30°
45°
60°
10^-2
10^-3
10^-4
INTENSITY (MeV/MeV-sr-Electron)
0
0.2
0.4
0.6
0.8
1.0
PHOTON ENERGY (MeV)

FIGURE 19

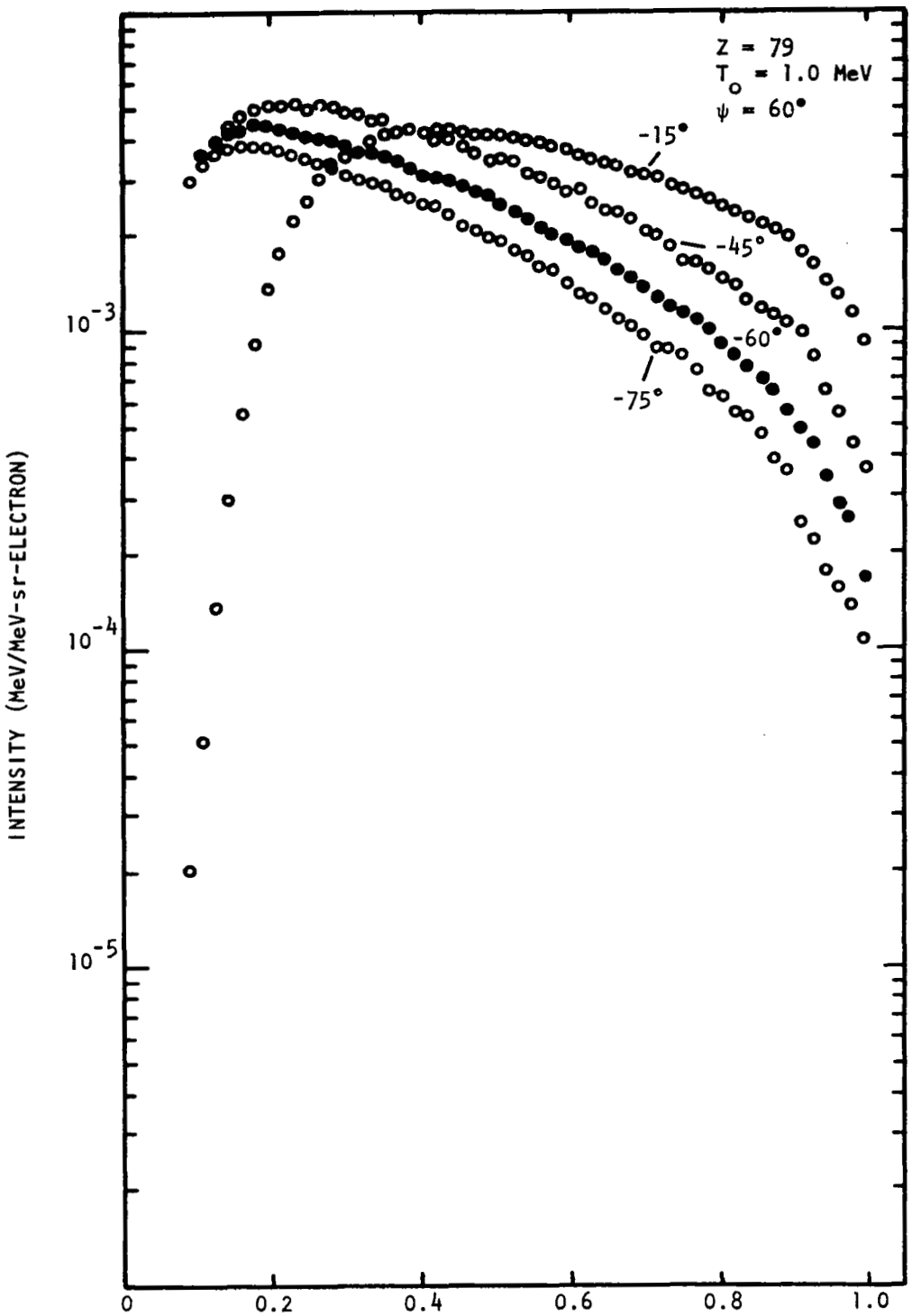
Z = 79
T$_o$ = 1.0 MeV
ψ = 60°
-15°
-45°
-60°
-75°
10^{-3}
10^{-4}
10^{-5}
INTENSITY (MeV/MeV-sr-ELECTRON)
0
0.2
0.4
0.6
0.8
1.0
PHOTON ENERGY (MeV)

FIGURE 20

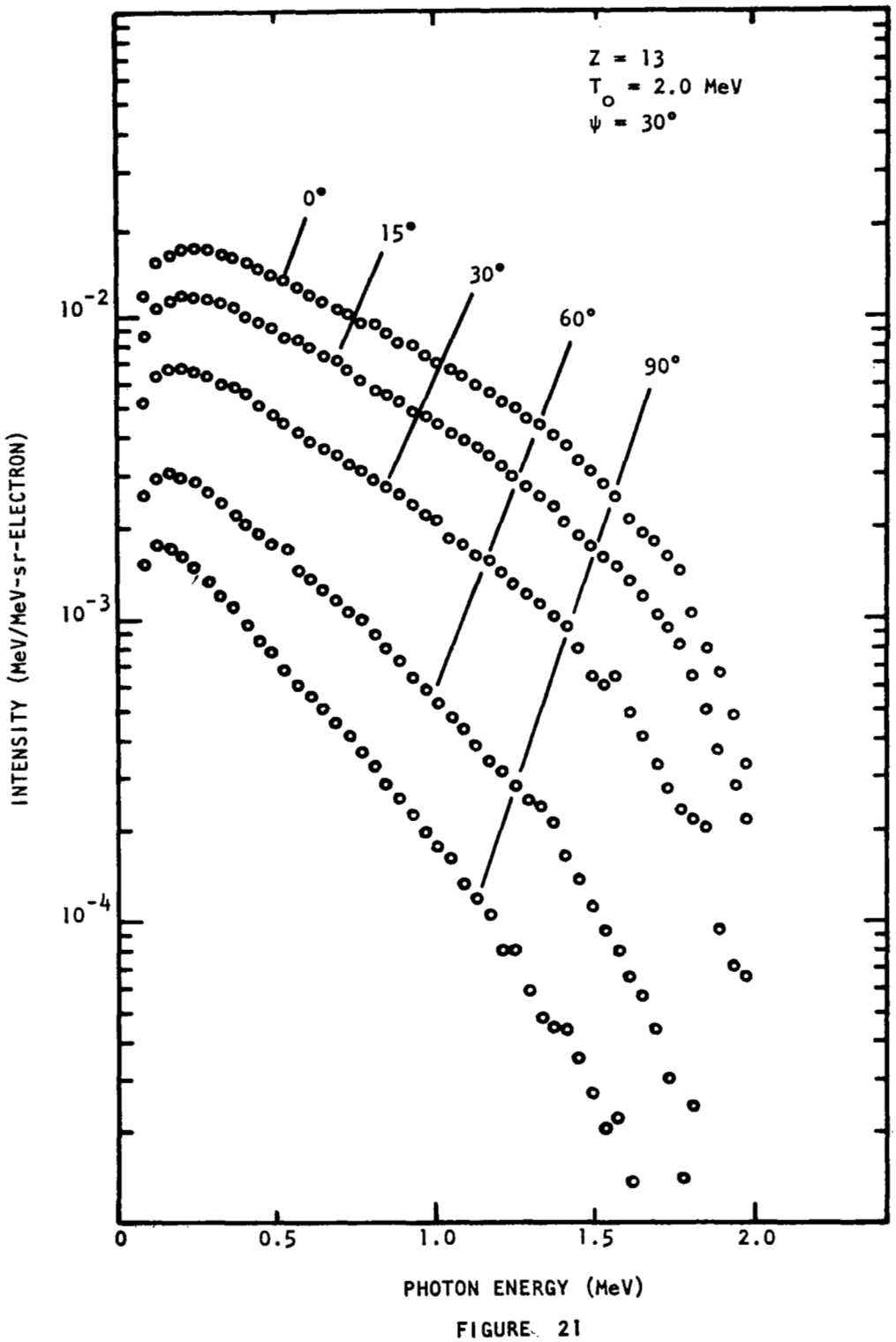
Z = 13
T_o = 2.0 MeV
ψ = 30°
0°
15°
30°
60°
90°
10^-2
10^-3
10^-4
INTENSITY (MeV/MeV-sr-ELECTRON)
0
0.5
1.0
1.5
2.0
PHOTON ENERGY (MeV)

FIGURE 21

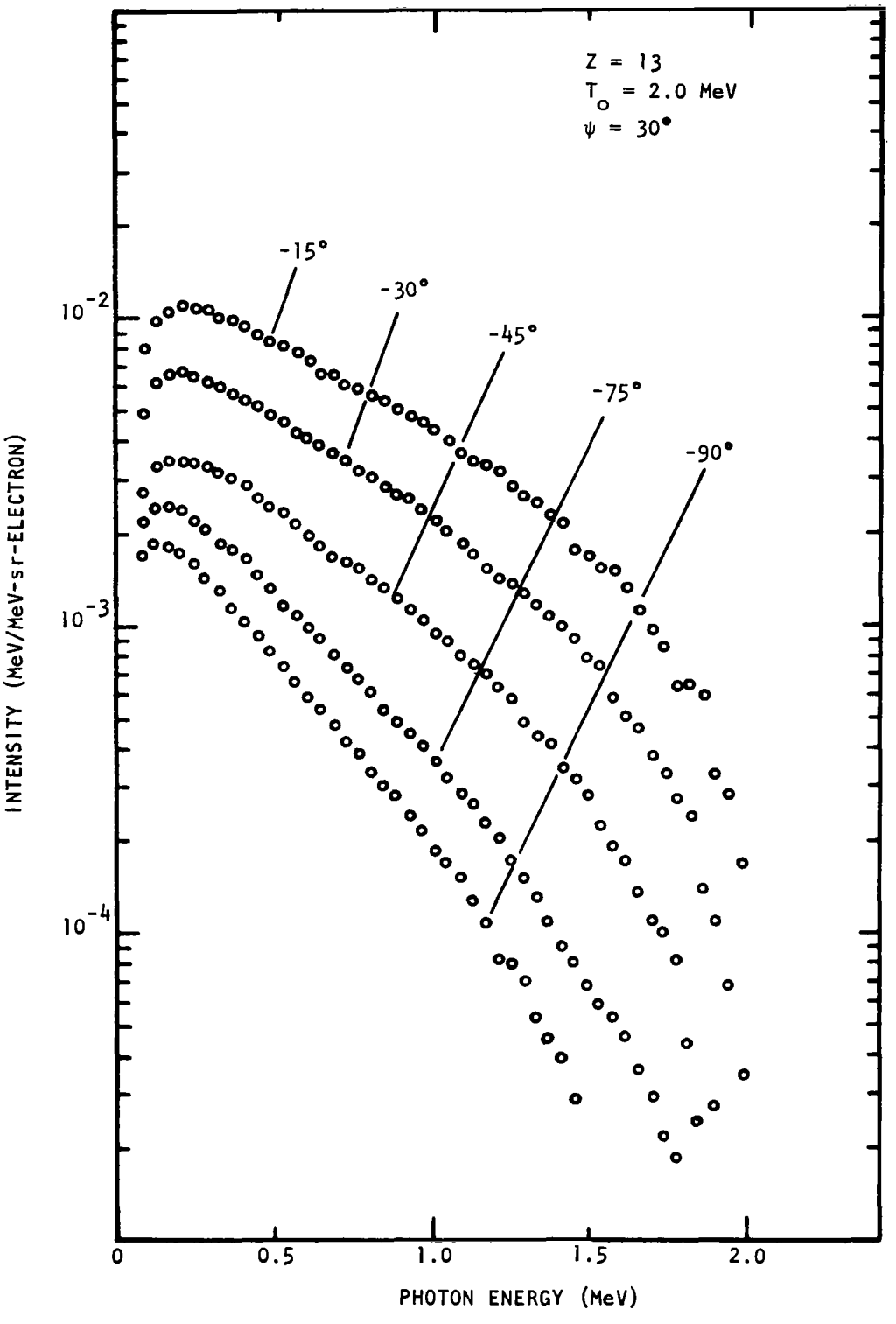
Z = 13
T_o = 2.0 MeV
ψ = 30°
-15°
-30°
-45°
-75°
-90°
10^-2
10^-3
10^-4
INTENSITY (MeV/MeV-sr-ELECTRON)
0
0.5
1.0
1.5
2.0
PHOTON ENERGY (MeV)

FIGURE 22

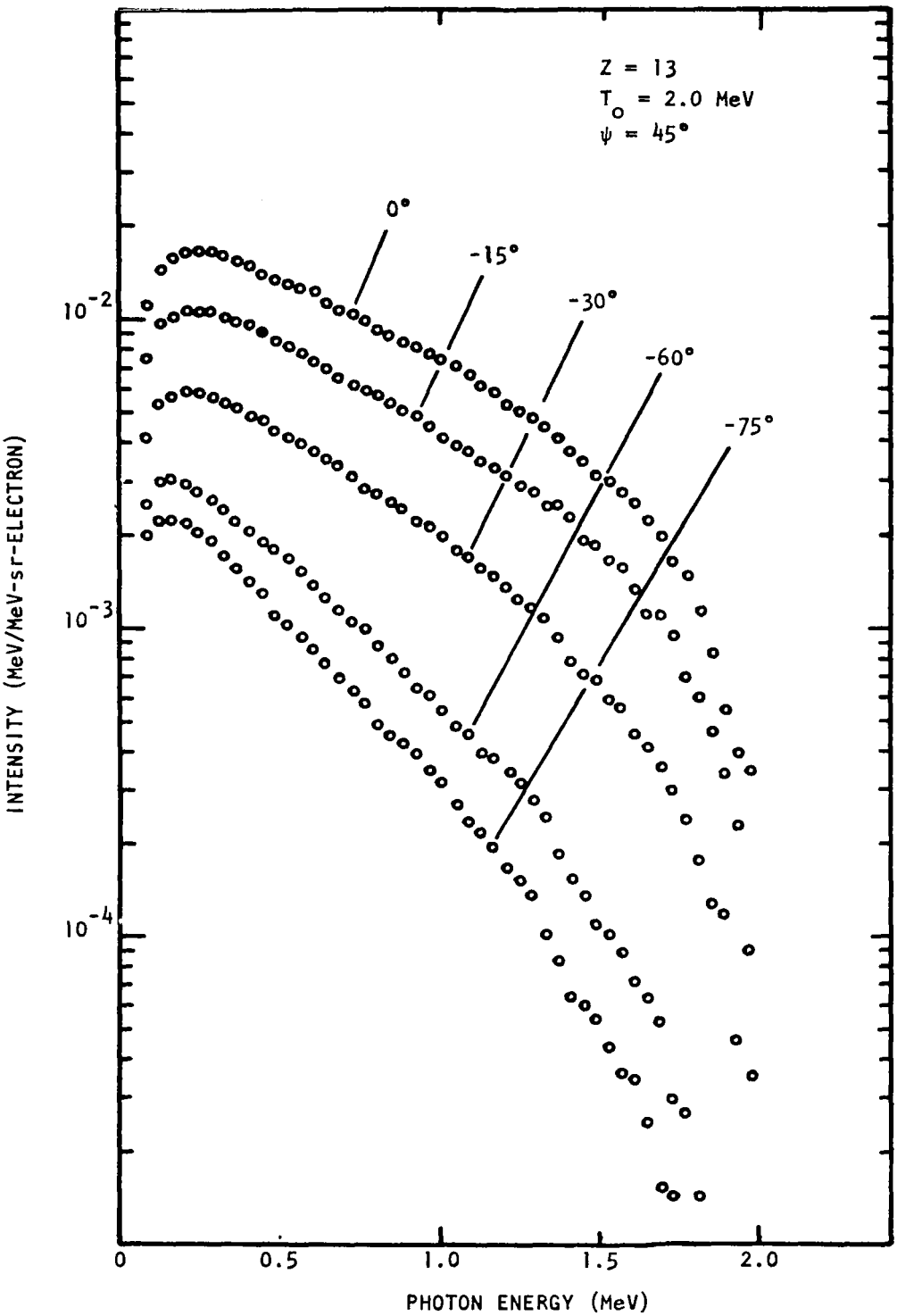
Z = 13
T_o = 2.0 MeV
ψ = 45°
0°
-15°
-30°
-60°
-75°
10^{-2}
10^{-3}
10^{-4}
INTENSITY (MeV/MeV-sr-ELECTRON)
0
0.5
1.0
1.5
2.0
PHOTON ENERGY (MeV)

FIGURE 23

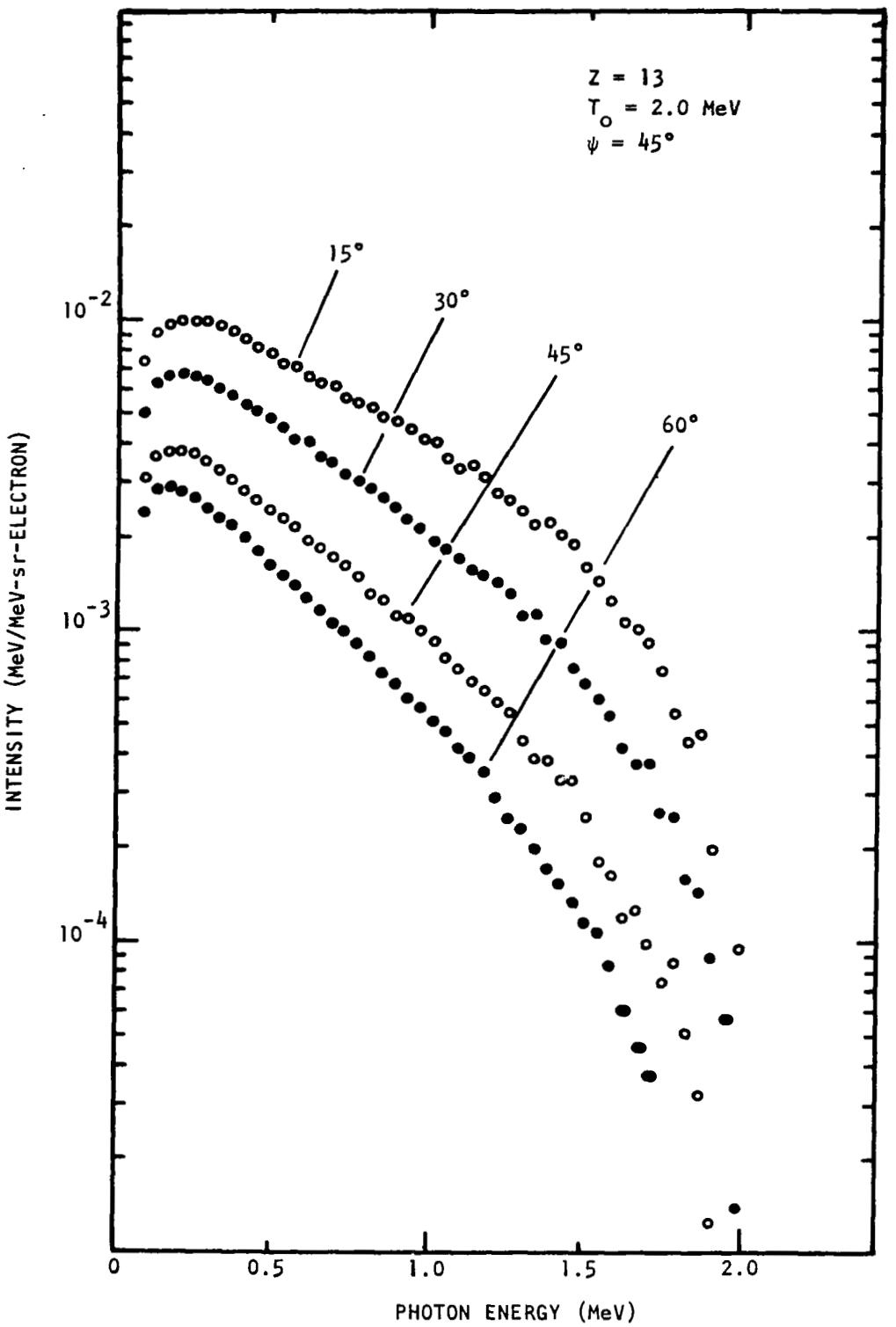
Z = 13
T_o = 2.0 MeV
ψ = 45°
15°
30°
45°
60°
10^{-2}
10^{-3}
10^{-4}
INTENSITY (MeV/MeV-sr-ELECTRON)
0
0.5
1.0
1.5
2.0
PHOTON ENERGY (MeV)

FIGURE 24

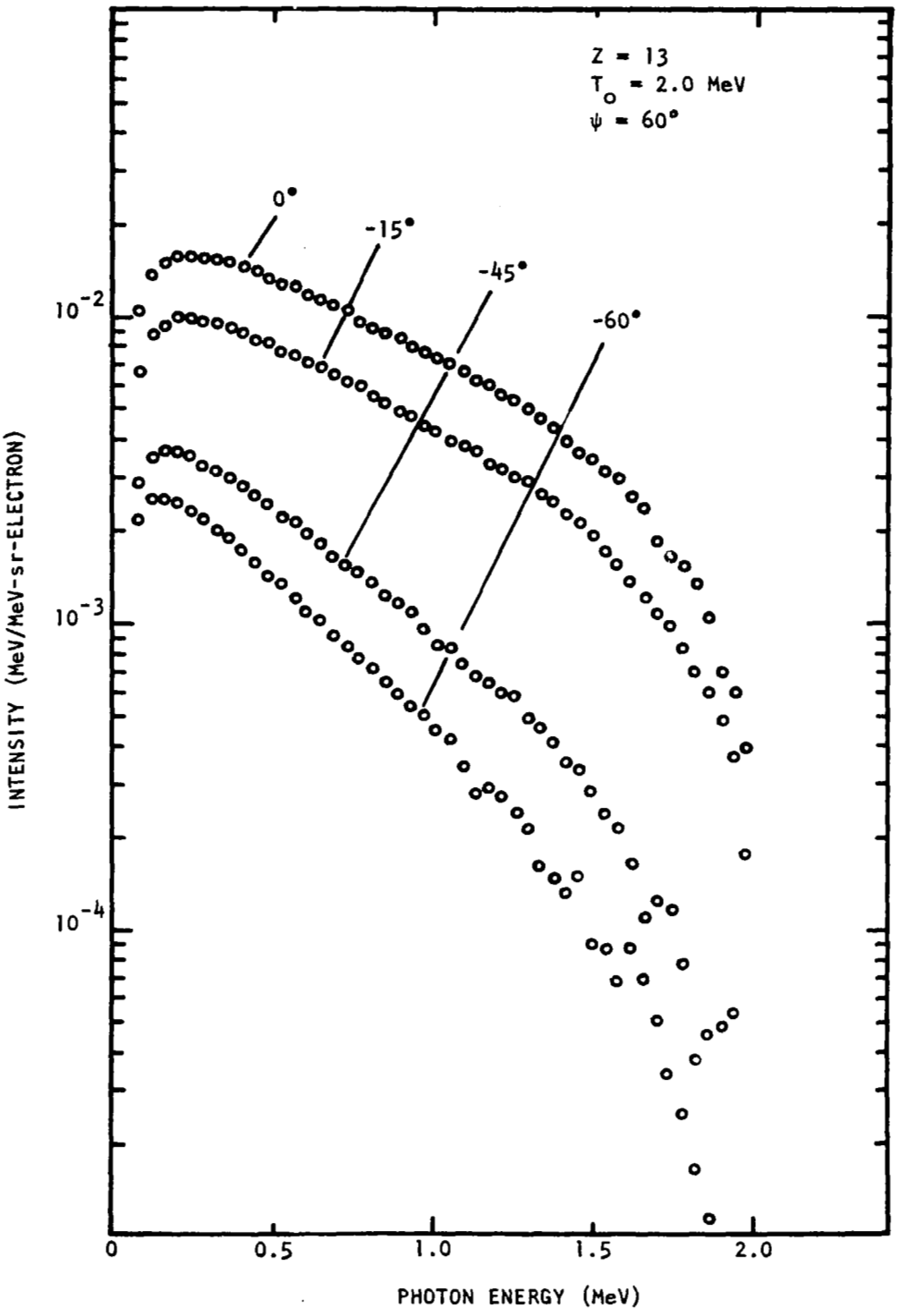
Z = 13
T_o = 2.0 MeV
ψ = 60°
0°
-15°
-45°
-60°
10^-2
10^-3
10^-4
INTENSITY (MeV/MeV-sr-ELECTRON)
0
0.5
1.0
1.5
2.0
PHOTON ENERGY (MeV)

FIGURE 25

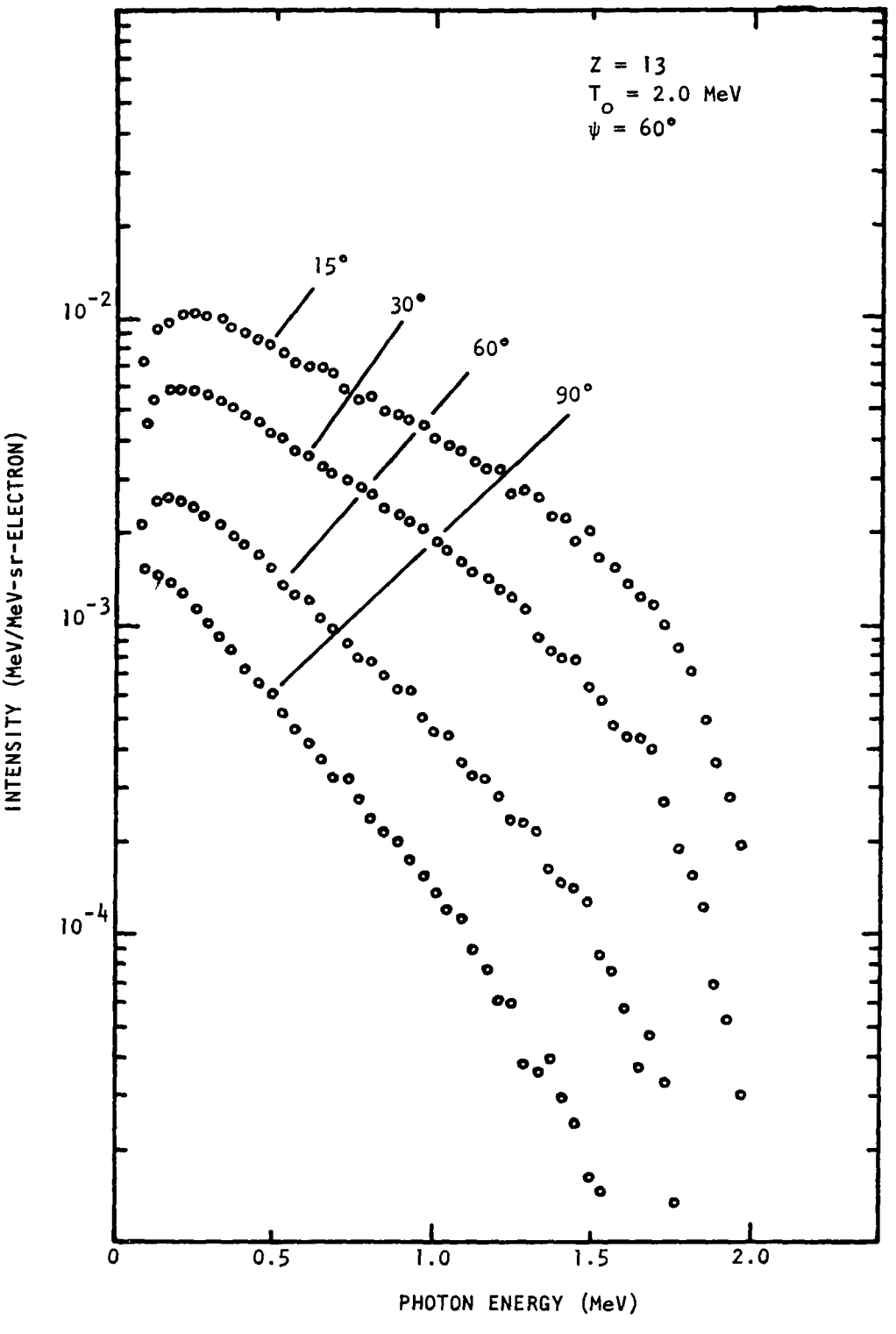
Z = 13
T_o = 2.0 MeV
ψ = 60°
15°
30°
60°
90°
10^{-2}
10^{-3}
10^{-4}
INTENSITY (MeV/MeV-sr-ELECTRON)
0
0.5
1.0
1.5
2.0
PHOTON ENERGY (MeV)

FIGURE 26

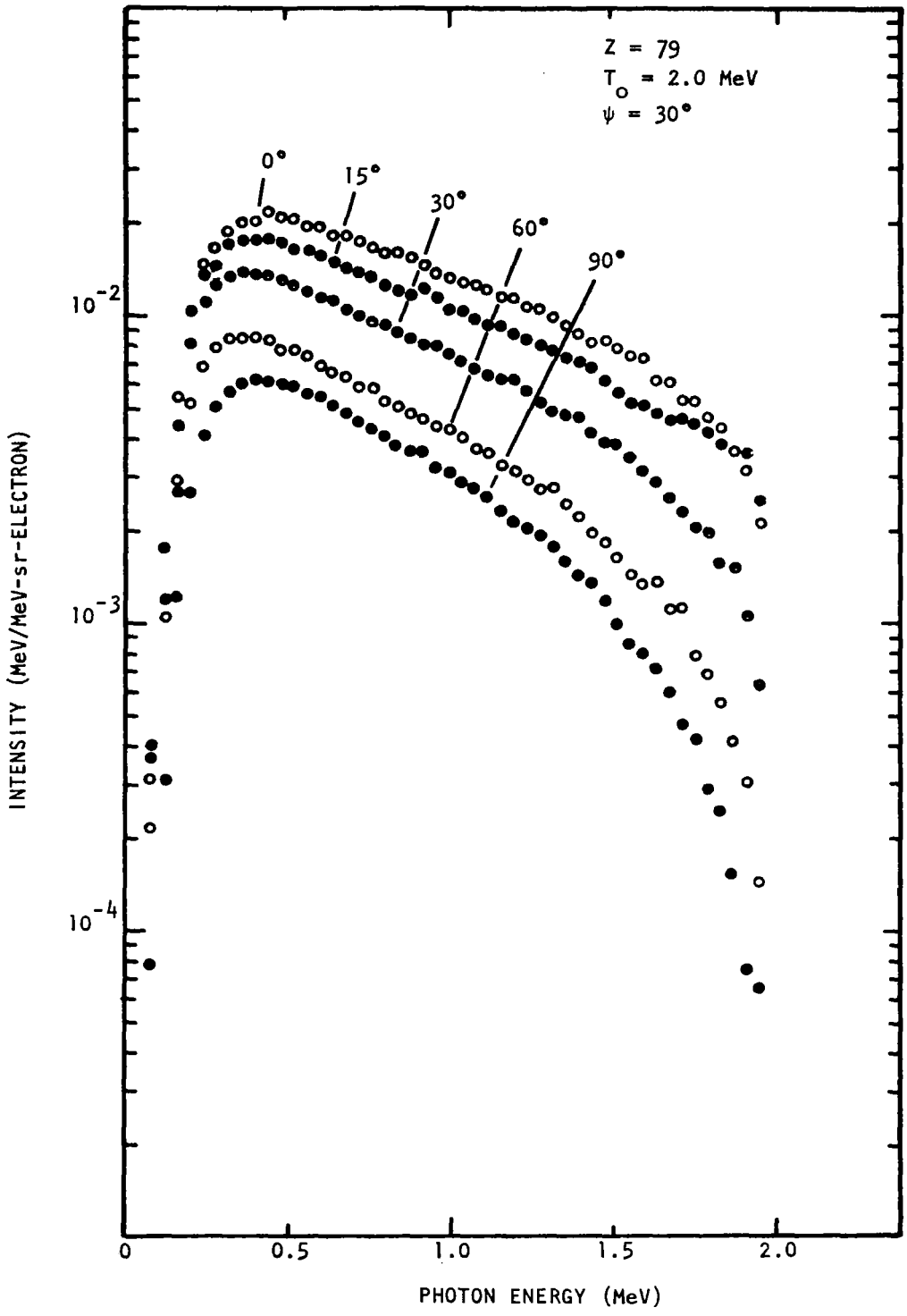
Z = 79
T_o = 2.0 MeV
ψ = 30°
0°
15°
30°
60°
90°
10^-2
10^-3
10^-4
INTENSITY (MeV/MeV-sr-ELECTRON)
0
0.5
1.0
1.5
2.0
PHOTON ENERGY (MeV)

FIGURE 27

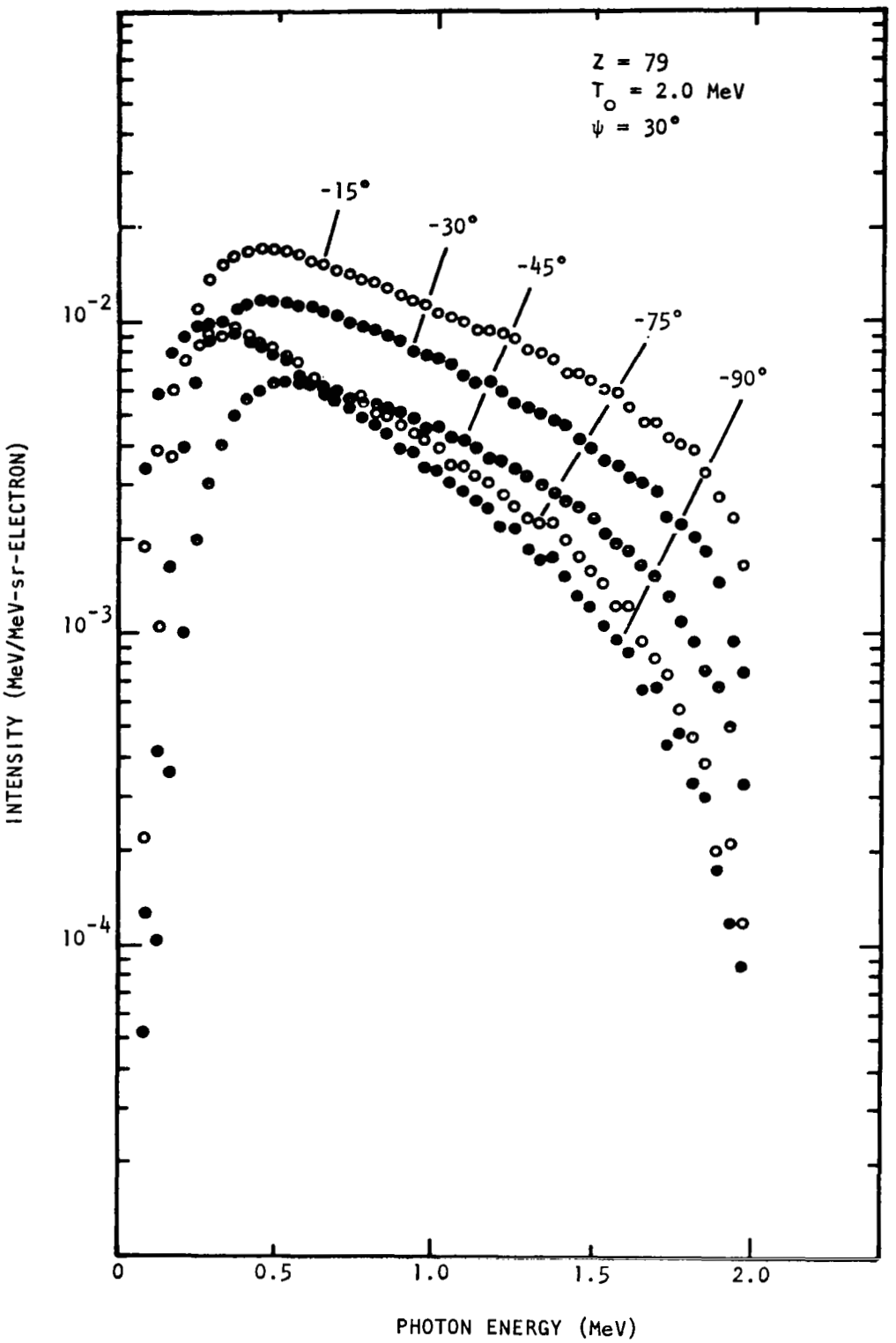
Z = 79
T_o = 2.0 MeV
ψ = 30°
-15°
-30°
-45°
-75°
-90°
10^{-2}
10^{-3}
10^{-4}
INTENSITY (MeV/MeV-sr-ELECTRON)
0
0.5
1.0
1.5
2.0
PHOTON ENERGY (MeV)

FIGURE 28

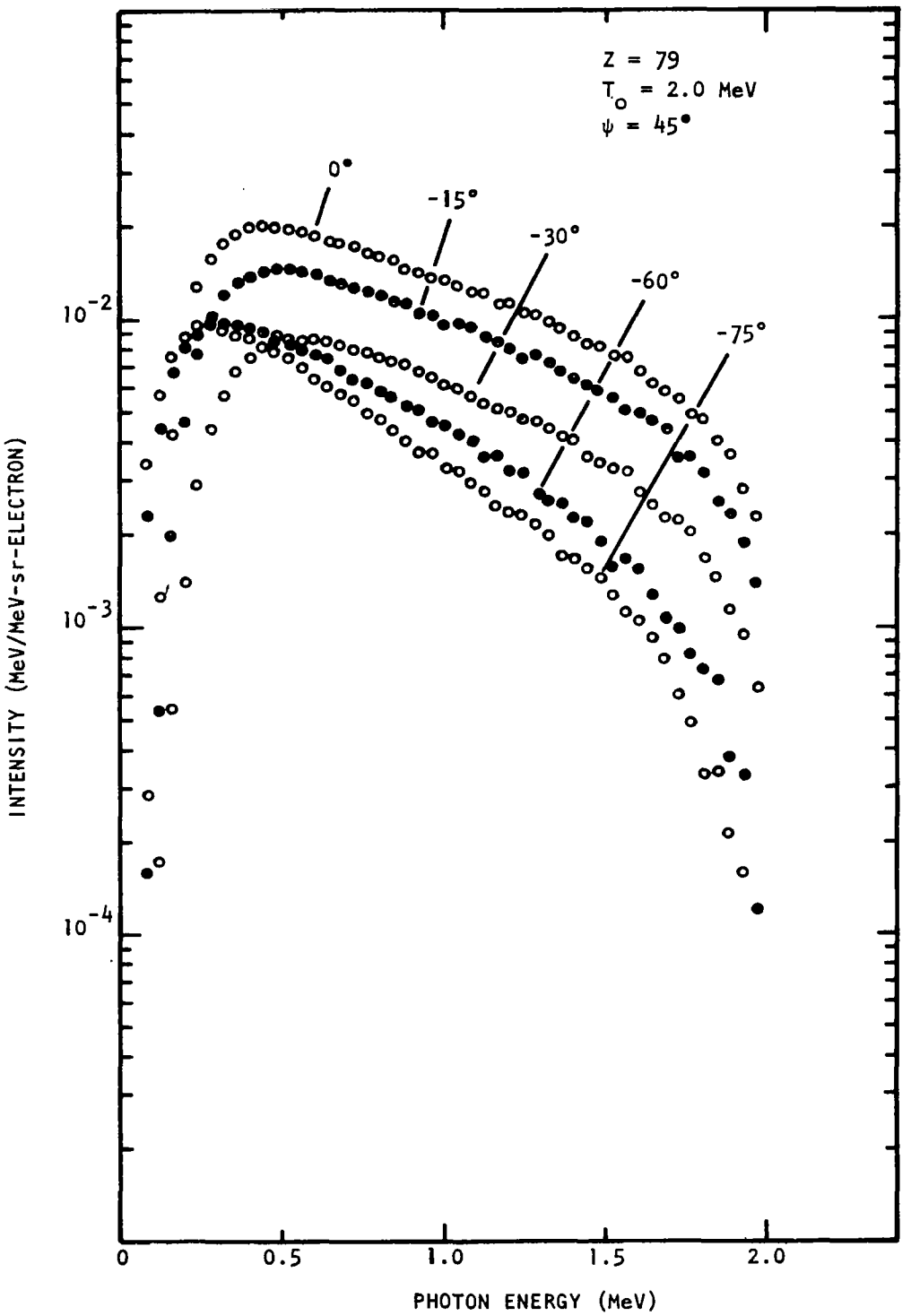
Z = 79
T$_o$ = 2.0 MeV
ψ = 45°
0°
-15°
-30°
-60°
-75°
10^{-2}
10^{-3}
10^{-4}
INTENSITY (MeV/MeV-sr-ELECTRON)
0
0.5
1.0
1.5
2.0
PHOTON ENERGY (MeV)

FIGURE 29

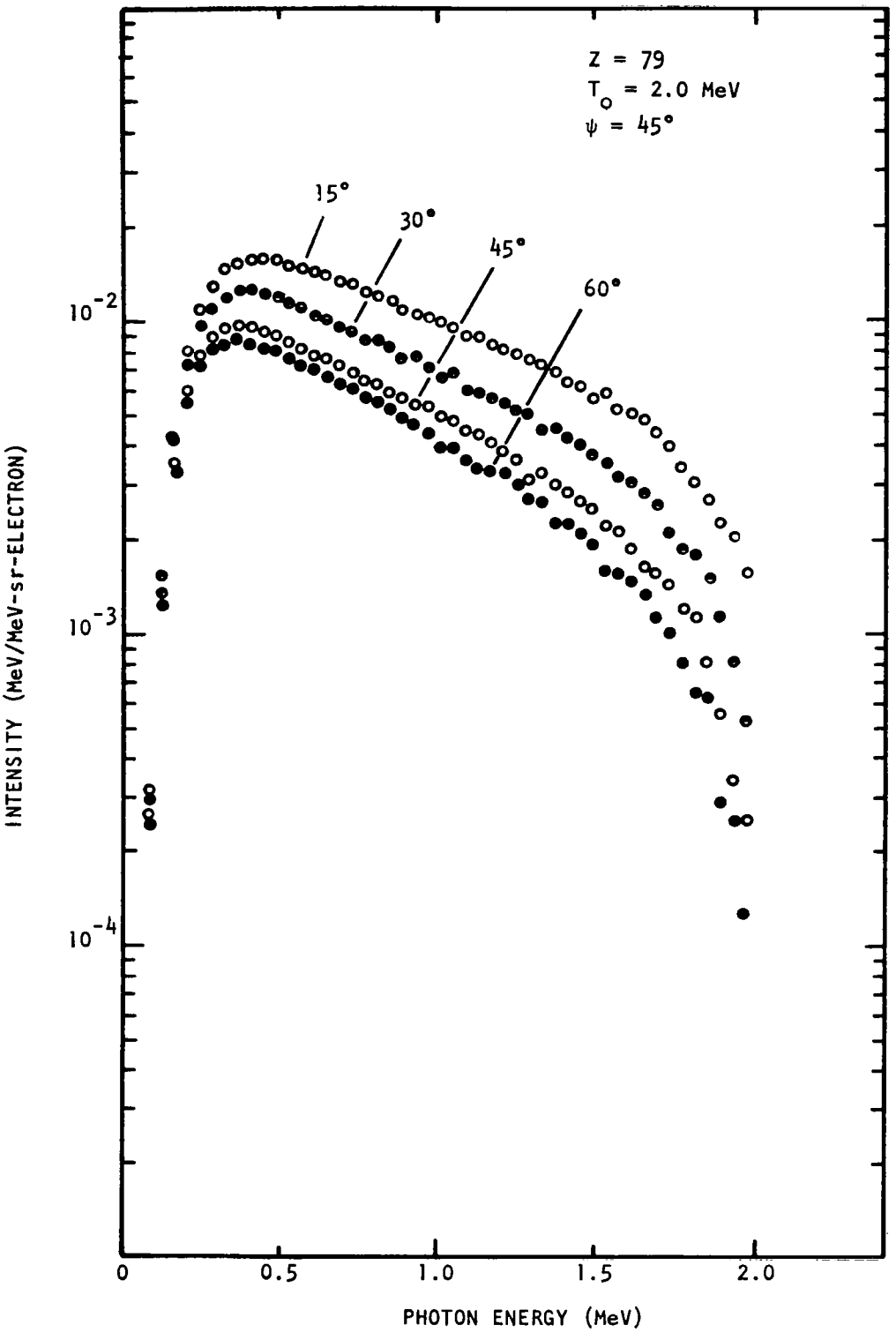
Z = 79
T_o = 2.0 MeV
ψ = 45°
15°
30°
45°
60°
10^{-2}
10^{-3}
10^{-4}
INTENSITY (MeV/MeV-sr-ELECTRON)
0
0.5
1.0
1.5
2.0
PHOTON ENERGY (MeV)

FIGURE 30

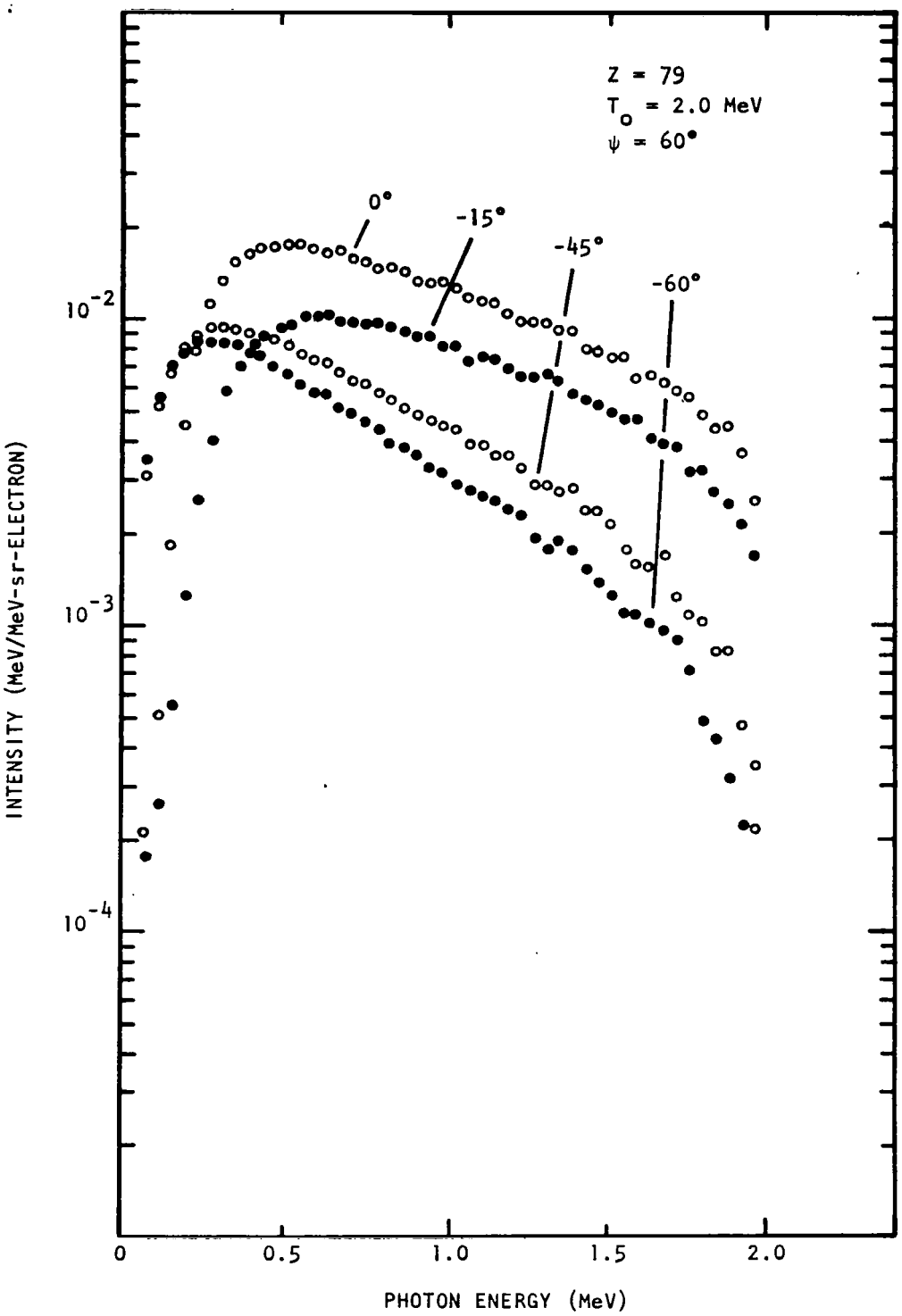
Z = 79
T_o = 2.0 MeV
ψ = 60°
0°
-15°
-45°
-60°
10^-2
10^-3
10^-4
INTENSITY (MeV/MeV-sr-ELECTRON)
0
0.5
1.0
1.5
2.0
PHOTON ENERGY (MeV)

FIGURE 31

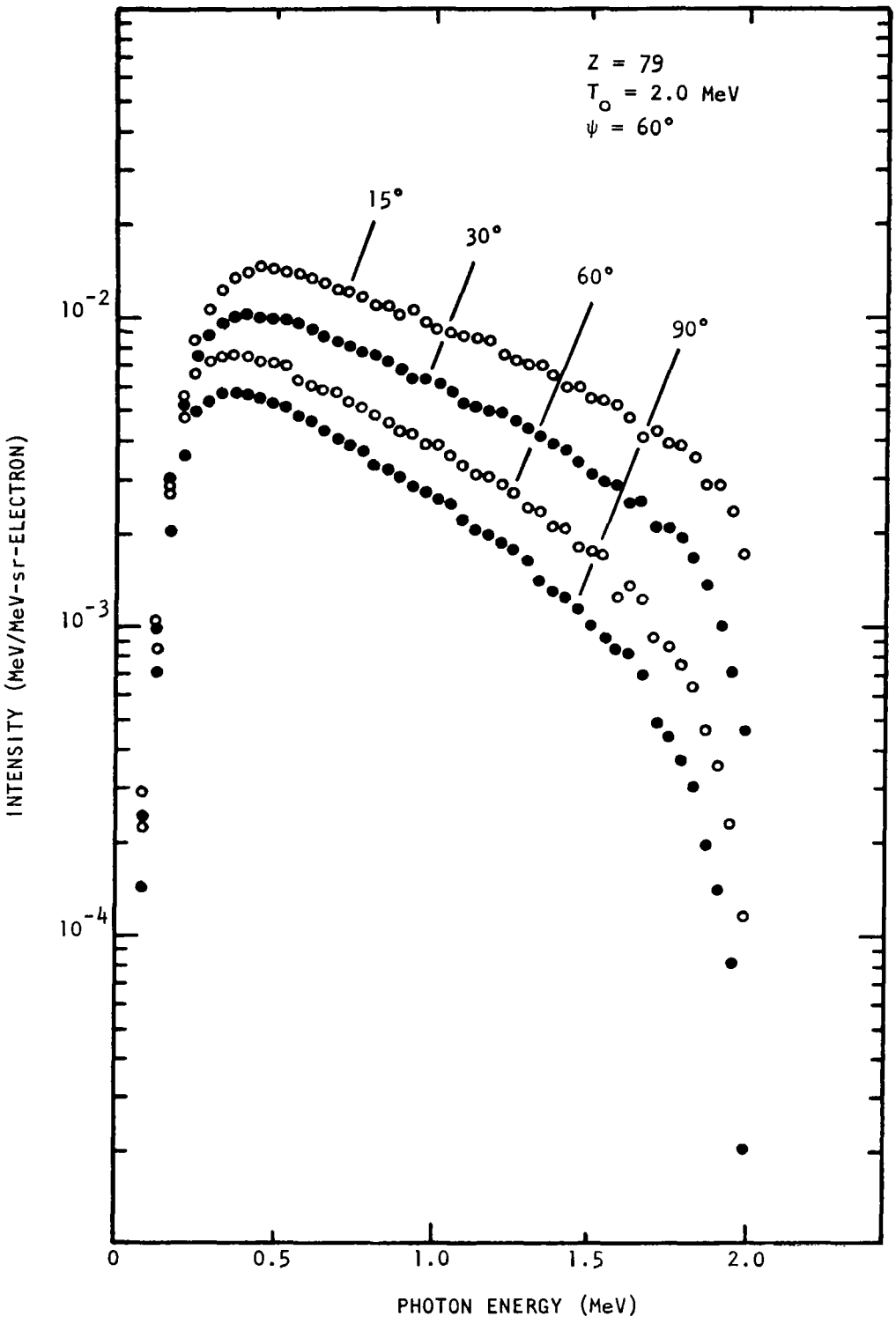
Z = 79
T_o = 2.0 MeV
ψ = 60°
15°
30°
60°
90°
10^{-2}
10^{-3}
10^{-4}
INTENSITY (MeV/MeV-sr-ELECTRON)
0
0.5
1.0
1.5
2.0
PHOTON ENERGY (MeV)

FIGURE 32

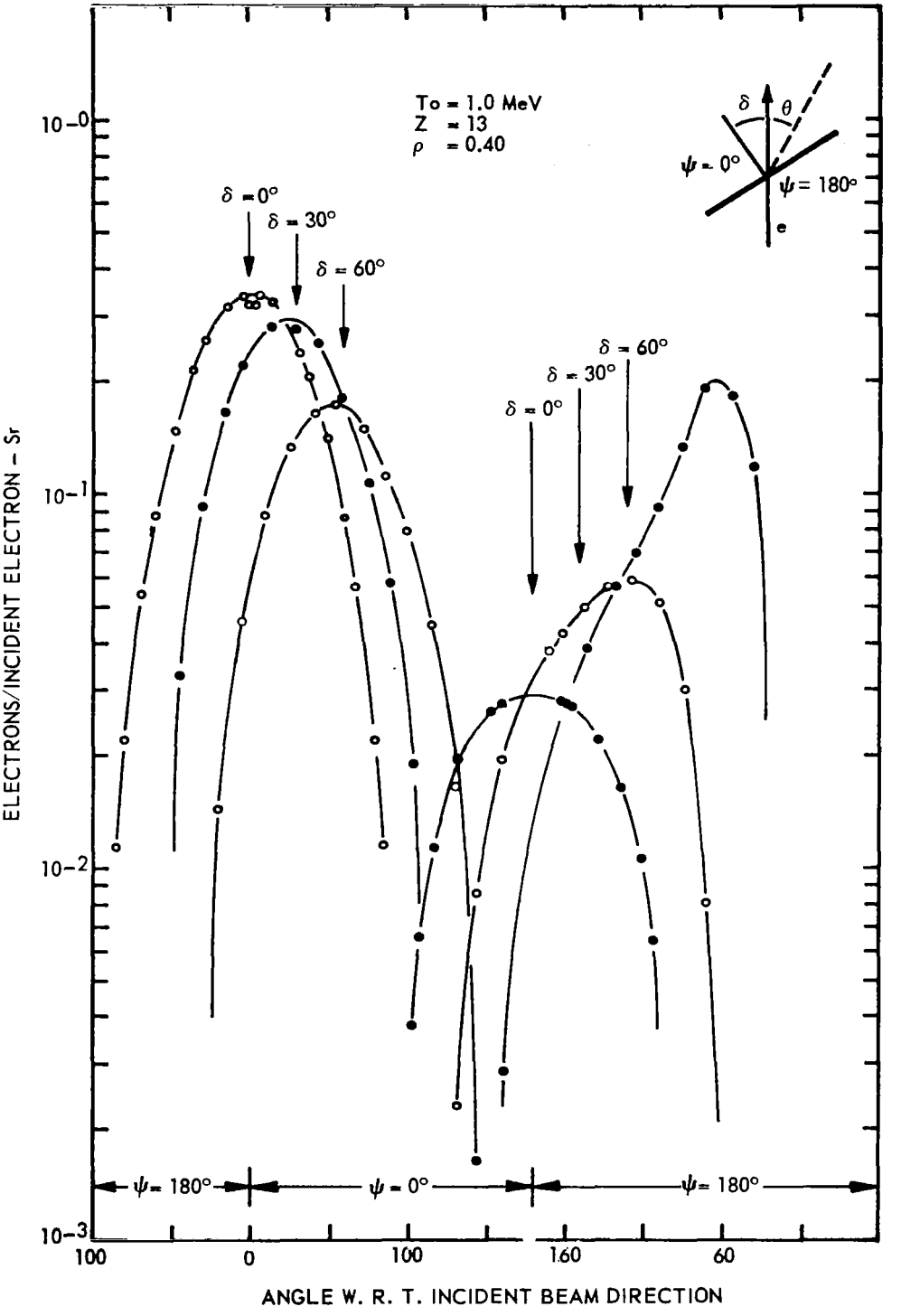
To = 1.0 MeV
Z = 13
ρ = 0.40
δ
θ
ψ = 0°
ψ = 180°
e
δ = 0°
δ = 30°
δ = 60°
δ = 60°
δ = 30°
δ = 0°
10−0
10−1
10−2
10−3
ELECTRONS/INCIDENT ELECTRON - Sr
ψ = 180°
ψ = 0°
ψ = 180°
100
0
100
160
60
ANGLE W. R. T. INCIDENT BEAM DIRECTION

FIGURE 33

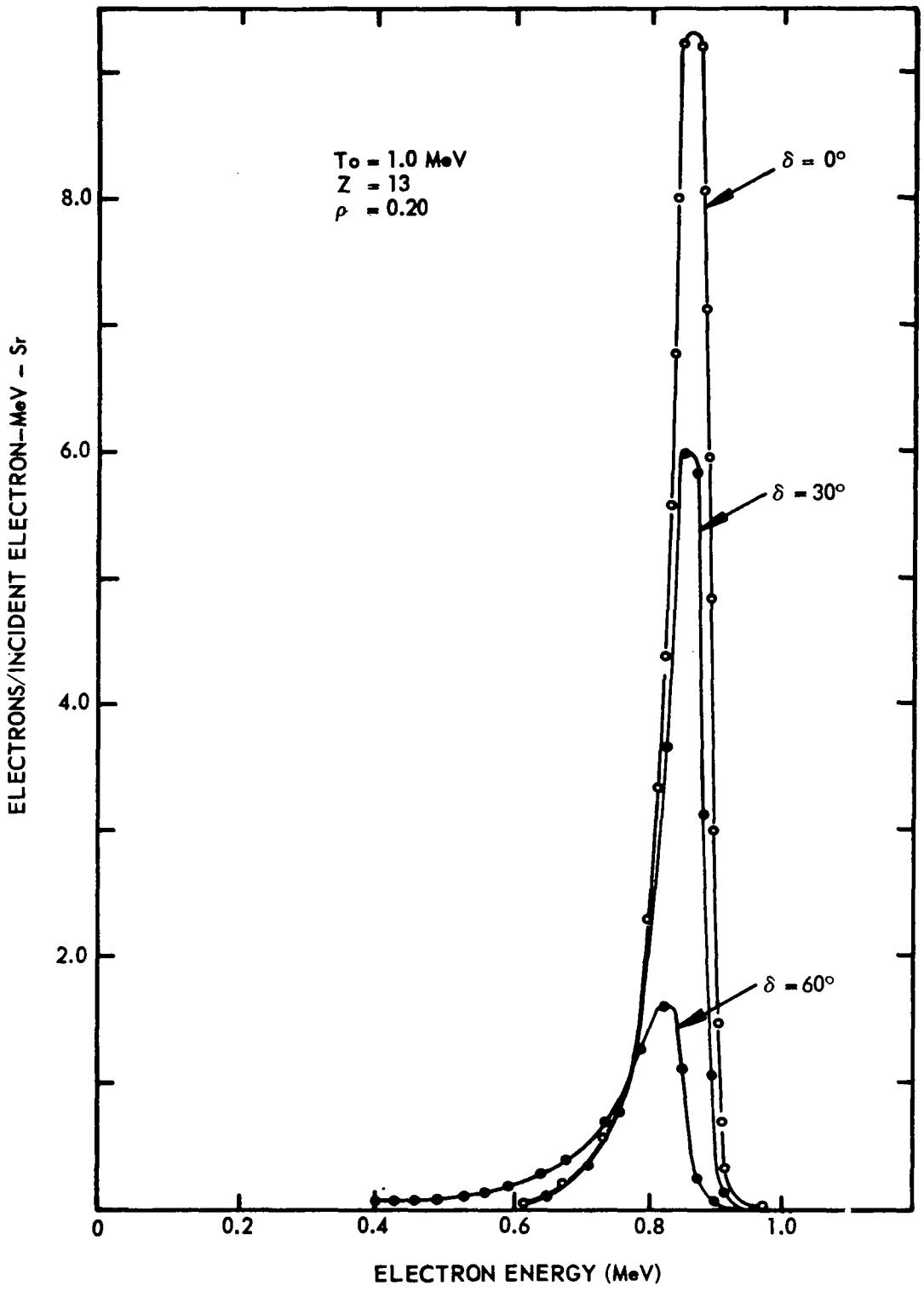
To = 1.0 MeV
Z = 13
ρ = 0.20
δ = 0°
δ = 30°
δ = 60°
8.0
6.0
4.0
2.0
0
0.2
0.4
0.6
0.8
1.0
ELECTRONS/INCIDENT ELECTRON-MeV - Sr
ELECTRON ENERGY (MeV)

FIGURE 34

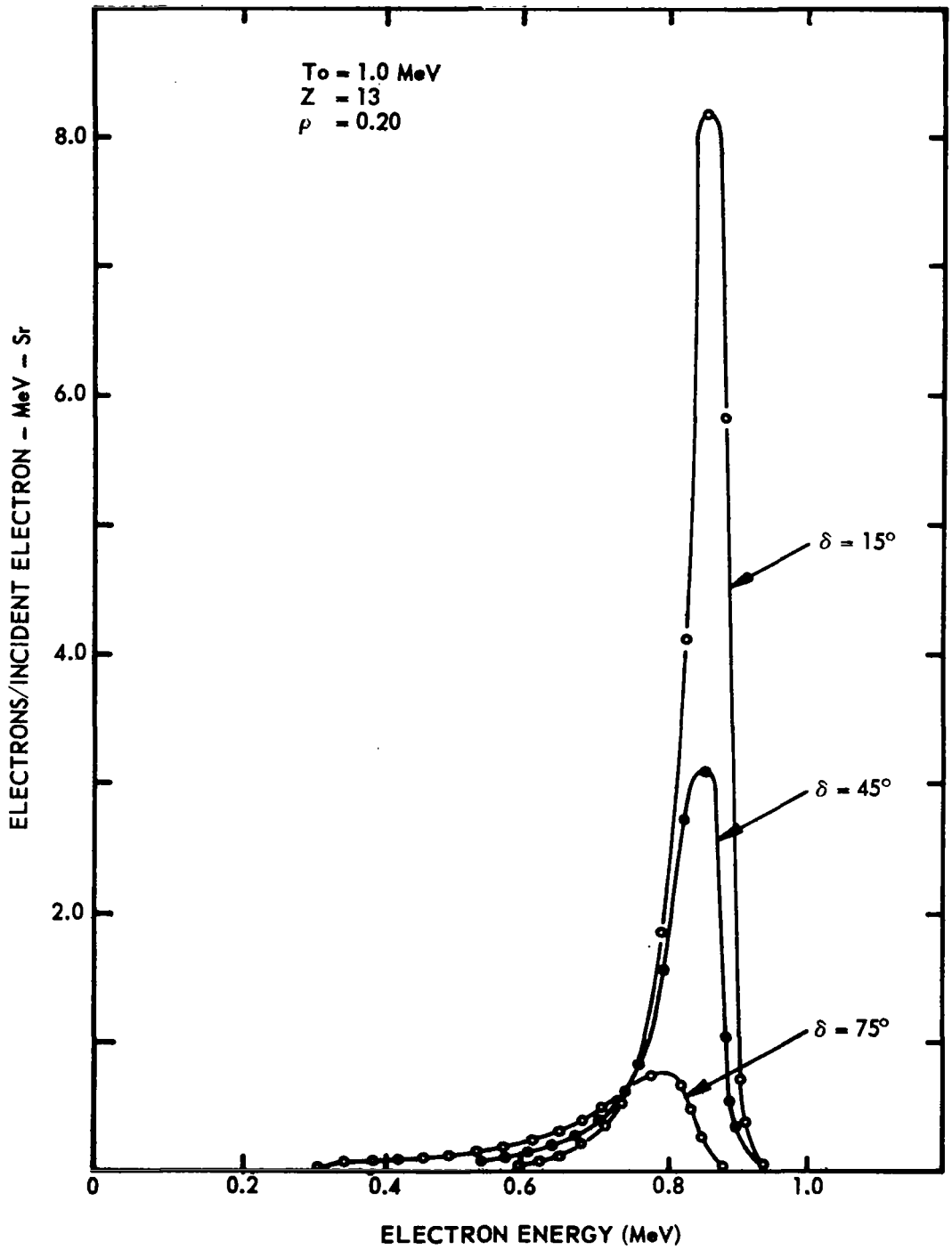
To = 1.0 MeV
Z = 13
ρ = 0.20
δ = 15°
δ = 45°
δ = 75°
8.0
6.0
4.0
2.0
0
0.2
0.4
0.6
0.8
1.0
ELECTRONS/INCIDENT ELECTRON - MeV - Sr
ELECTRON ENERGY (MeV)

FIGURE 35

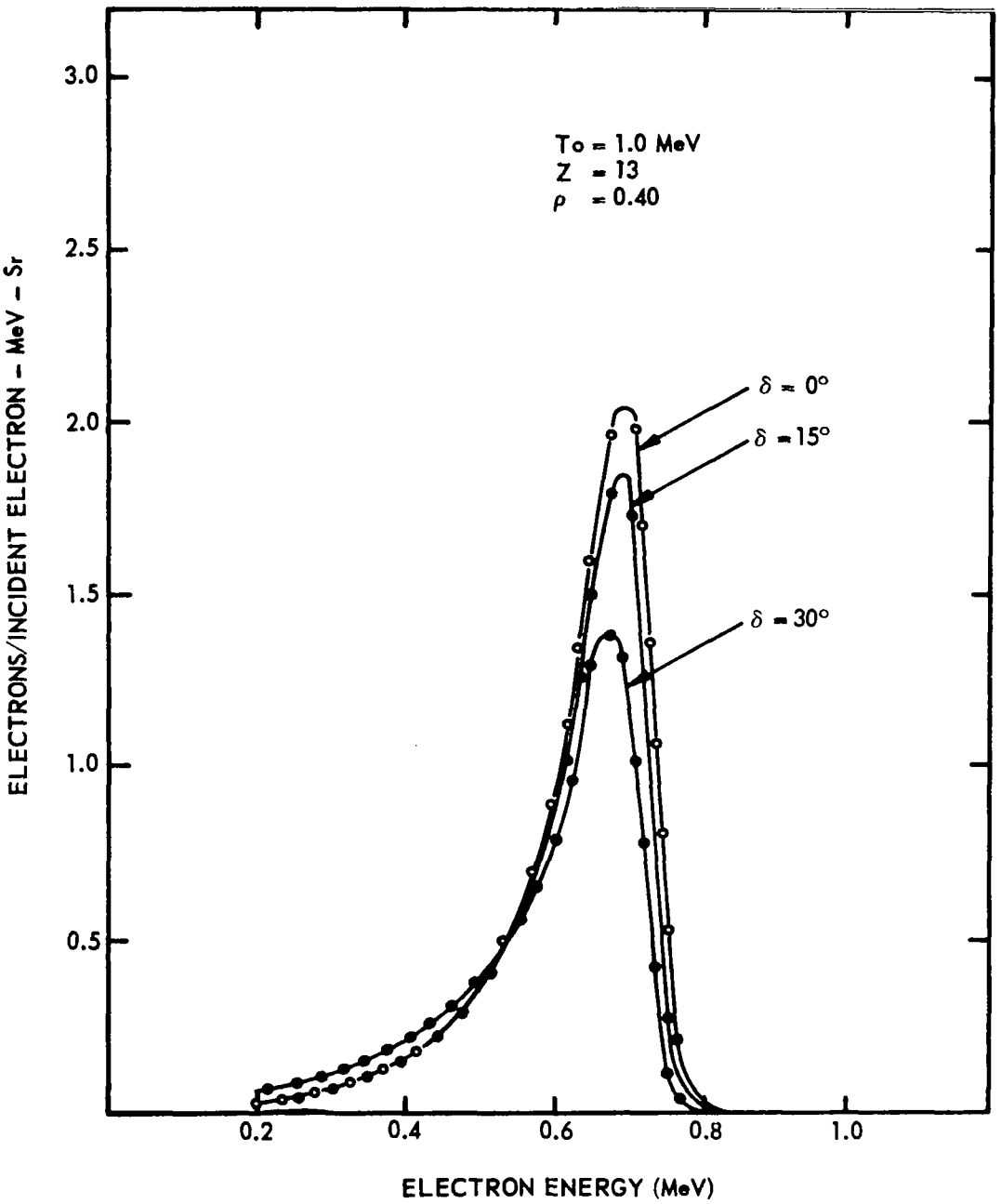
To = 1.0 MeV
Z = 13
ρ = 0.40
δ = 0°
δ = 15°
δ = 30°
ELECTRONS/INCIDENT ELECTRON - MeV - Sr
ELECTRON ENERGY (MeV)
3.0
2.5
2.0
1.5
1.0
0.5
0.2
0.4
0.6
0.8
1.0

FIGURE 36

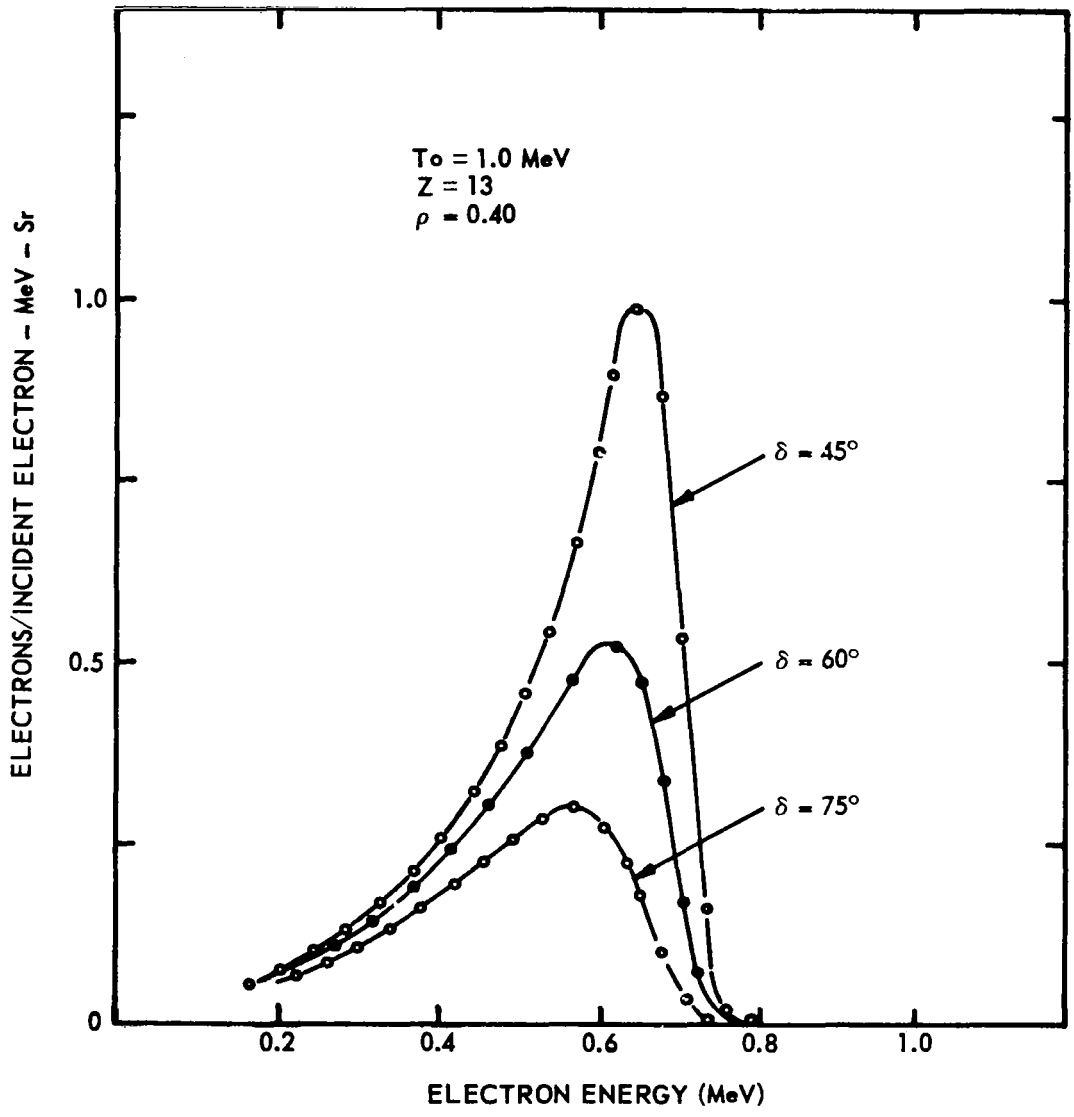
To = 1.0 MeV
Z = 13
ρ = 0.40
δ = 45°
δ = 60°
δ = 75°
ELECTRONS/INCIDENT ELECTRON - MeV - Sr
ELECTRON ENERGY (MeV)
0
0.5
1.0
0.2
0.4
0.6
0.8
1.0

FIGURE 37

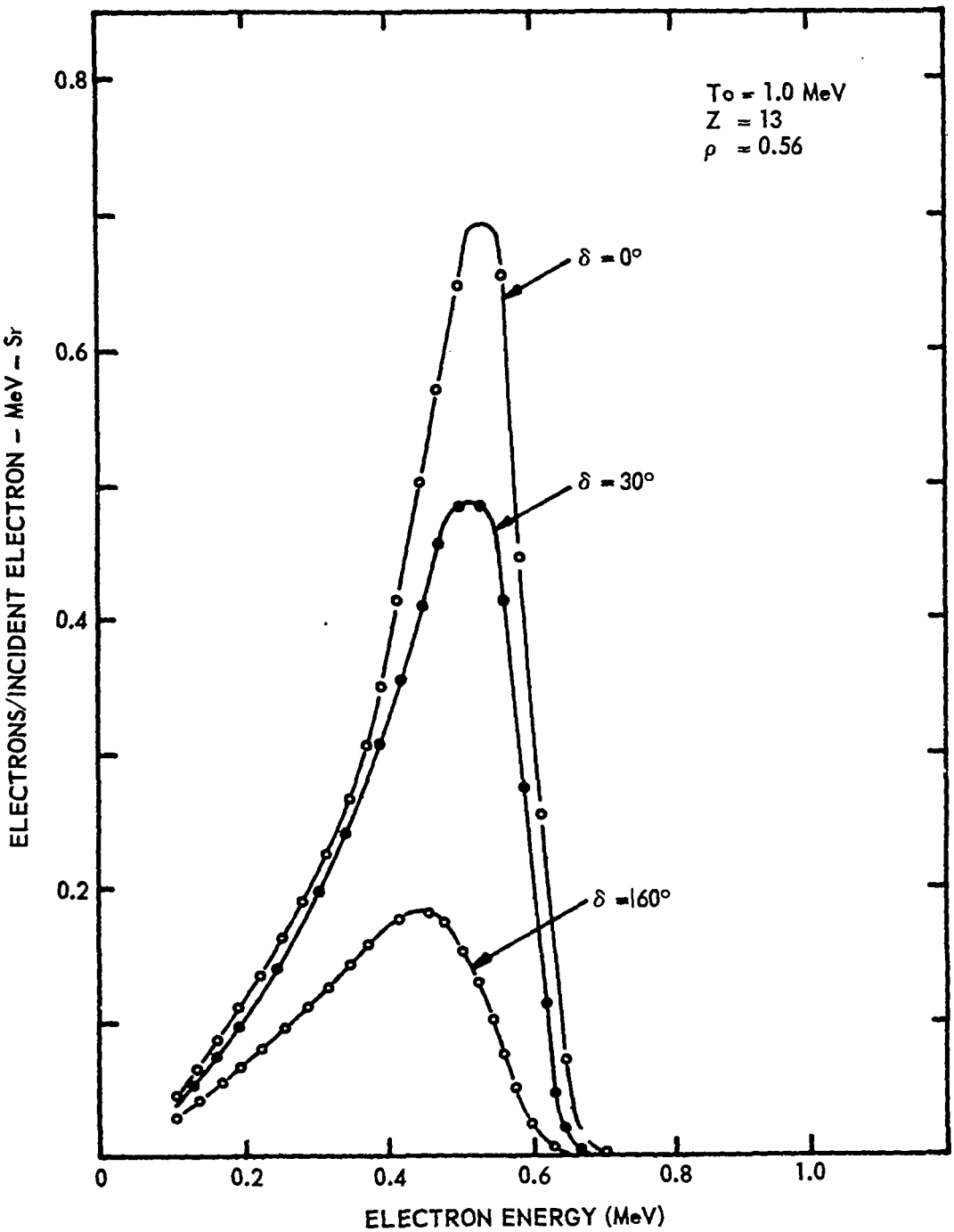
To = 1.0 MeV
Z = 13
ρ = 0.56
δ = 0°
δ = 30°
δ = 160°
ELECTRONS/INCIDENT ELECTRON – MeV – Sr
ELECTRON ENERGY (MeV)
0.8
0.6
0.4
0.2
0
0.2
0.4
0.6
0.8
1.0

FIGURE 38

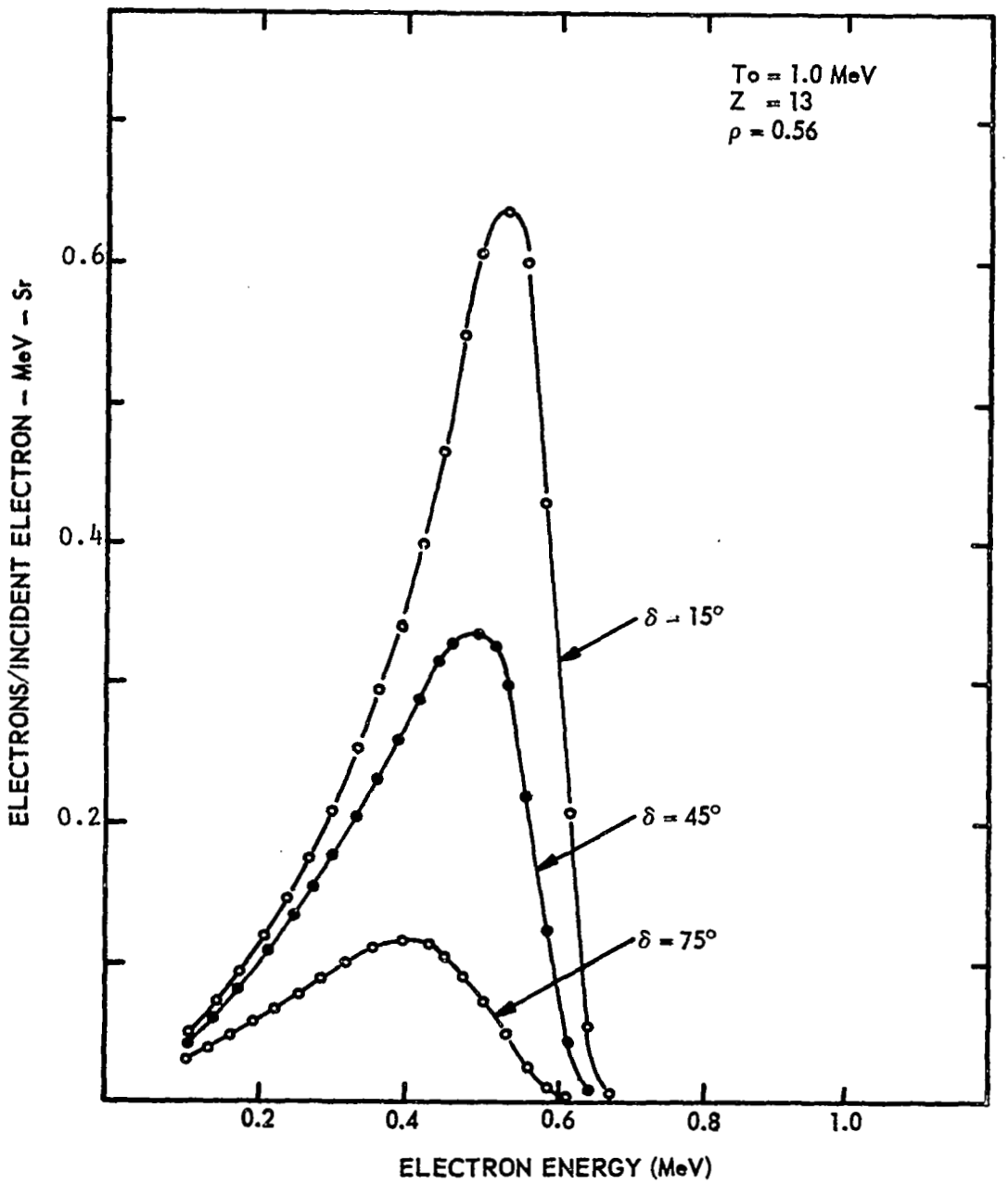
To = 1.0 MeV
Z = 13
ρ = 0.56
δ = 15°
δ = 45°
δ = 75°
0.6
0.4
0.2
0.2
0.4
0.6
0.8
1.0
ELECTRONS/INCIDENT ELECTRON - MeV - Sr
ELECTRON ENERGY (MeV)

FIGURE 39

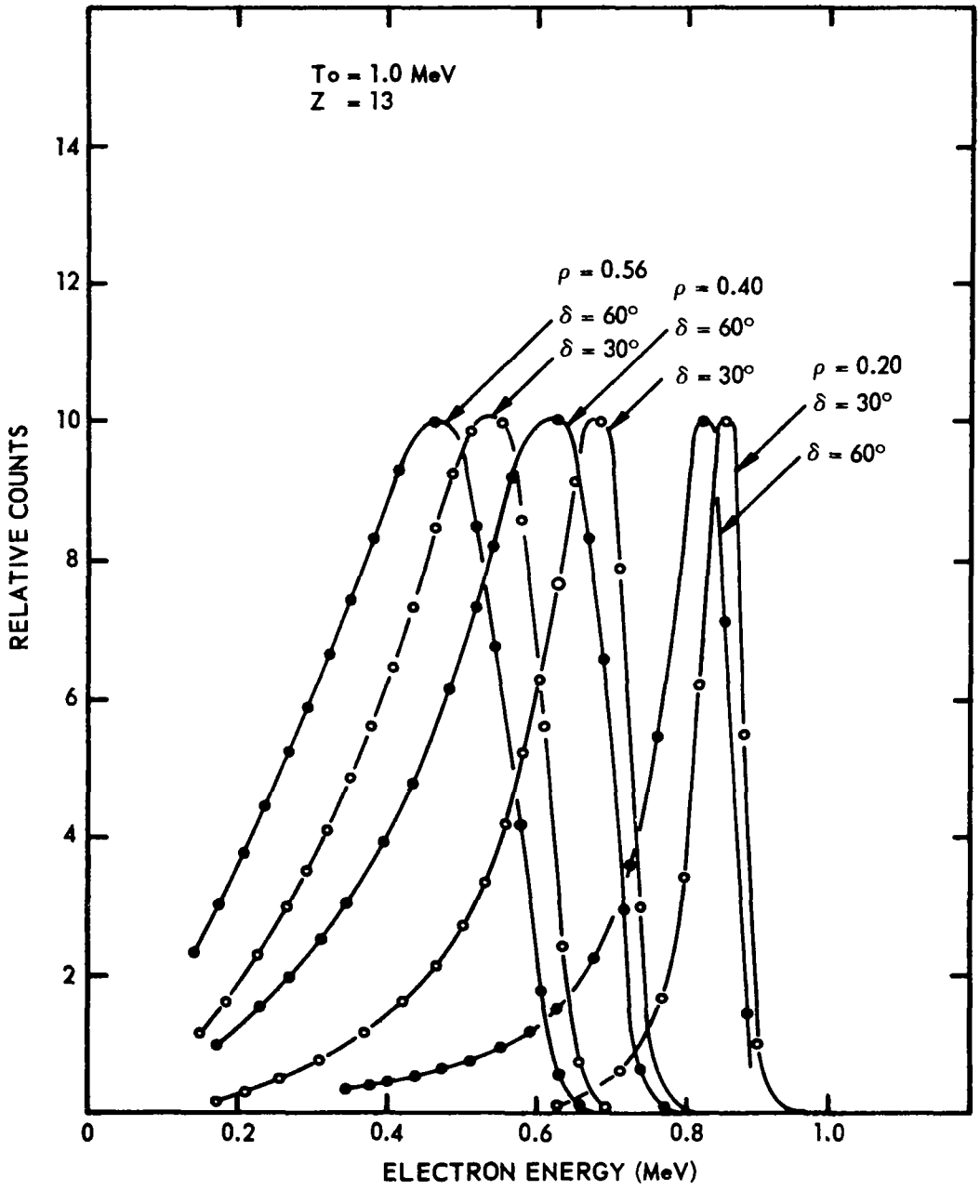
To = 1.0 MeV
Z = 13
ρ = 0.56
δ = 60°
δ = 30°
ρ = 0.40
δ = 60°
δ = 30°
ρ = 0.20
δ = 30°
δ = 60°
RELATIVE COUNTS
ELECTRON ENERGY (MeV)
0
2
4
6
8
10
12
14
0.2
0.4
0.6
0.8
1.0

FIGURE 40

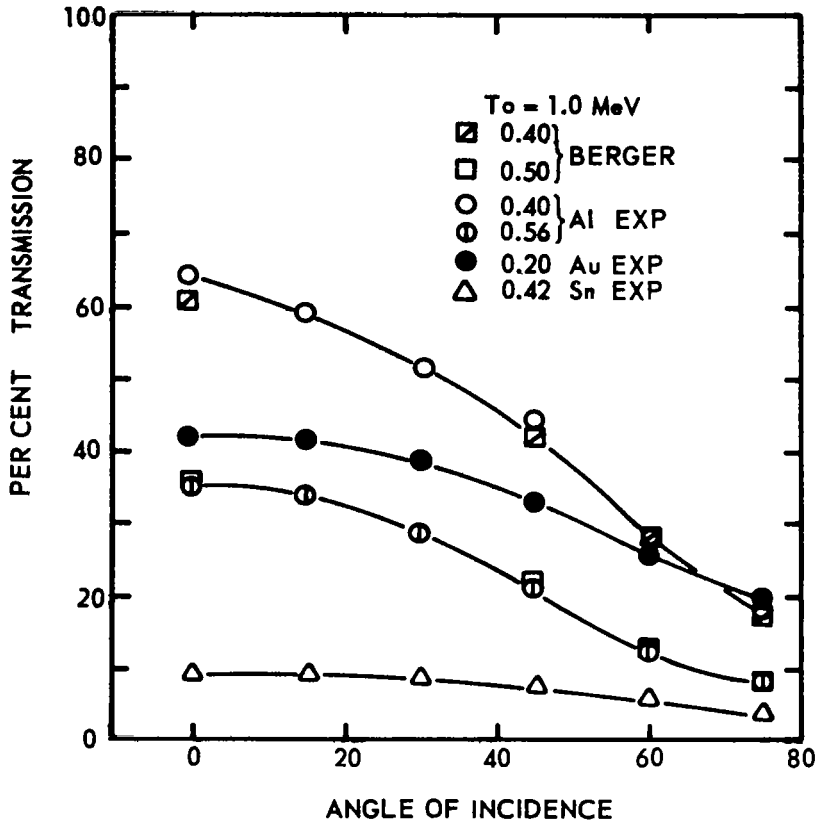
100
80
60
40
20
0
PER CENT TRANSMISSION
To = 1.0 MeV
0.40
0.50
BERGER
0.40
0.56
Al EXP
0.20 Au EXP
0.42 Sn EXP
0
20
40
60
80
ANGLE OF INCIDENCE

FIGURE 41

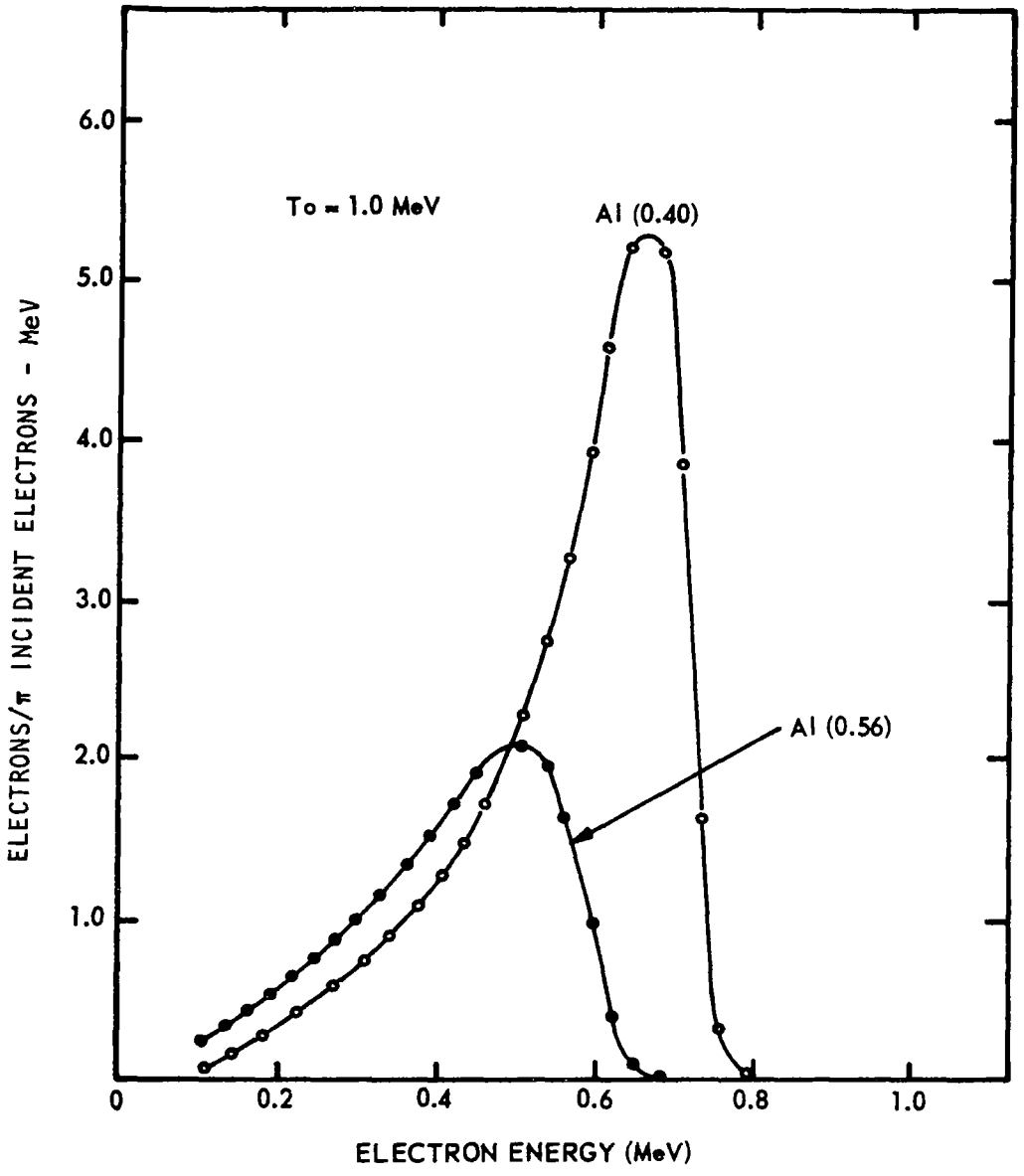
To = 1.0 MeV
Al (0.40)
Al (0.56)
ELECTRONS/π INCIDENT ELECTRONS - MeV
ELECTRON ENERGY (MeV)
6.0
5.0
4.0
3.0
2.0
1.0
0
0.2
0.4
0.6
0.8
1.0

FIGURE 42

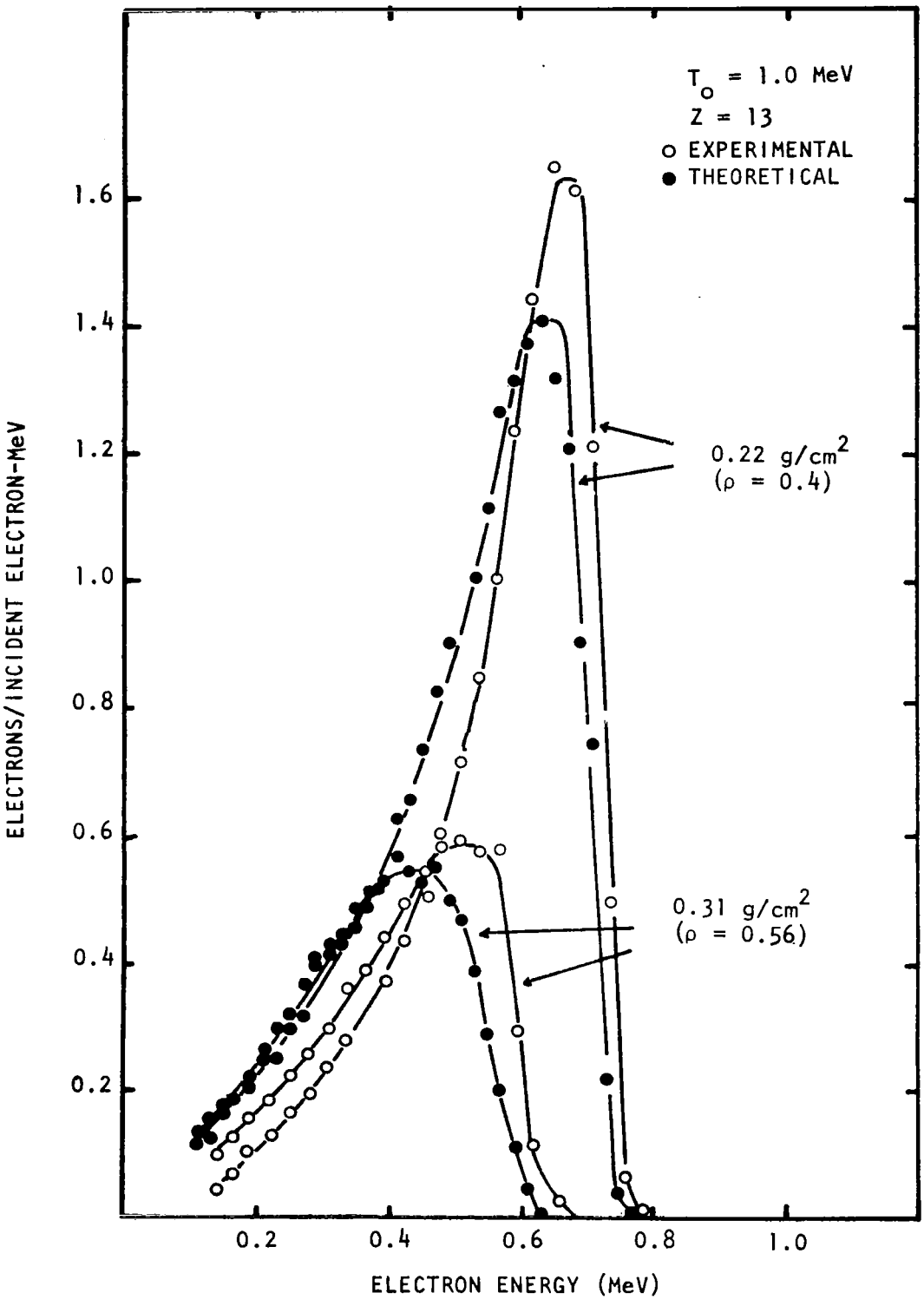
T_o = 1.0 MeV
Z = 13
o EXPERIMENTAL
● THEORETICAL
0.22 g/cm^2
(ρ = 0.4)
0.31 g/cm^2
(ρ = 0.56)
ELECTRONS/INCIDENT ELECTRON-MeV
ELECTRON ENERGY (MeV)
0.2
0.4
0.6
0.8
1.0
1.2
1.4
1.6

FIGURE 43

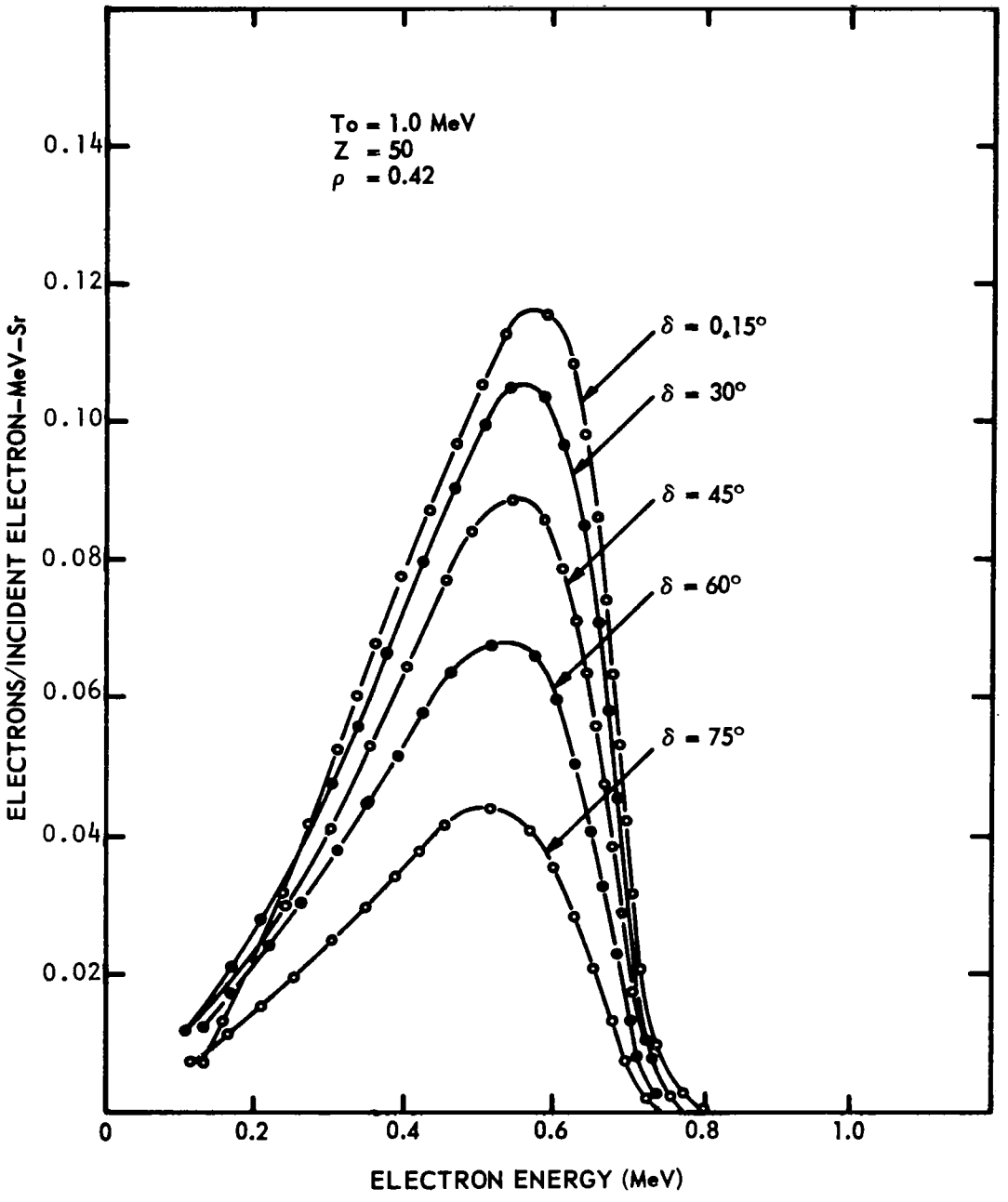
To = 1.0 MeV
Z = 50
ρ = 0.42
δ = 0.15°
δ = 30°
δ = 45°
δ = 60°
δ = 75°
ELECTRONS/INCIDENT ELECTRON-MeV-Sr
0.14
0.12
0.10
0.08
0.06
0.04
0.02
0
0.2
0.4
0.6
0.8
1.0
ELECTRON ENERGY (MeV)

FIGURE 44

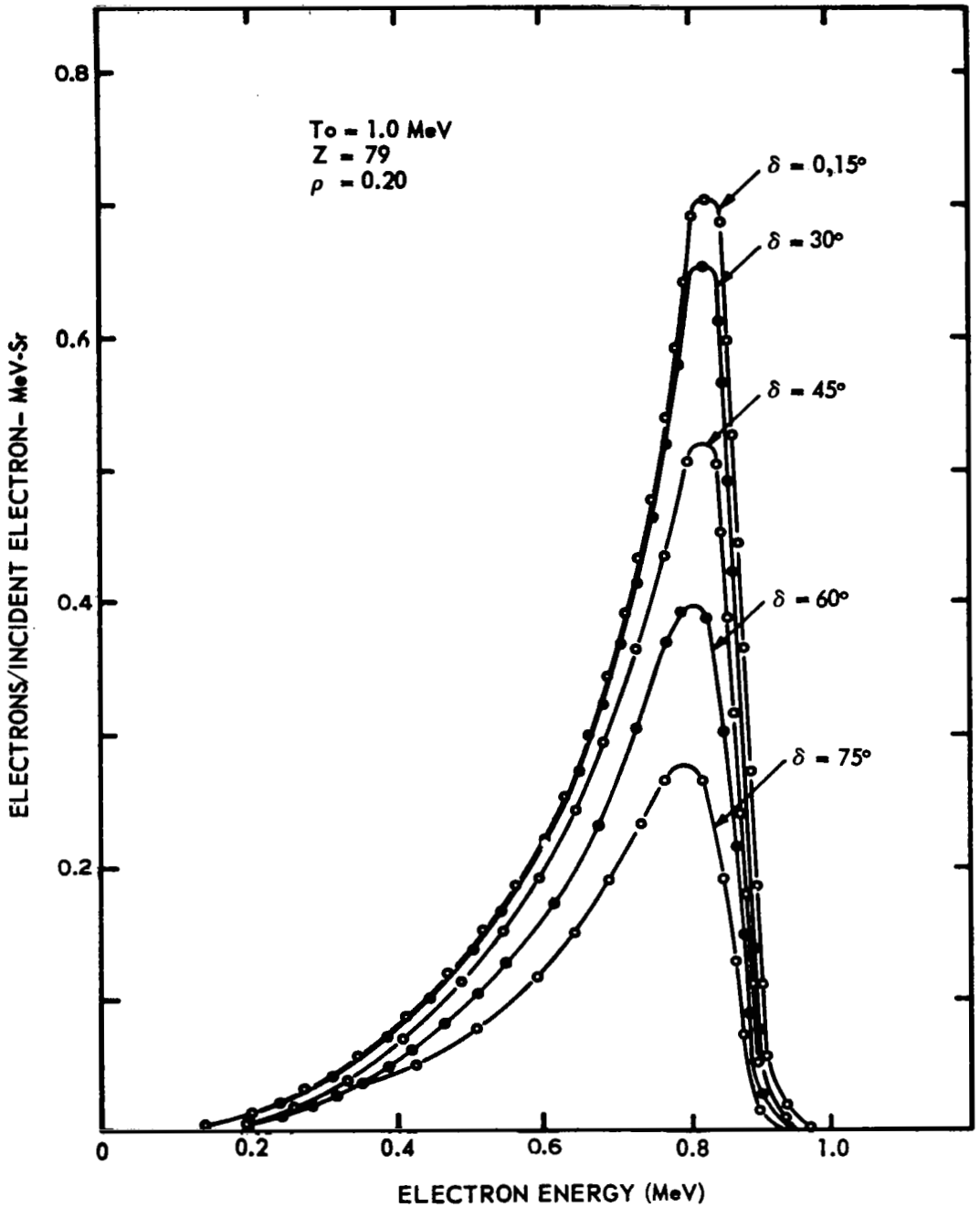
To = 1.0 MeV
Z = 79
ρ = 0.20
δ = 0,15°
δ = 30°
δ = 45°
δ = 60°
δ = 75°
ELECTRONS/INCIDENT ELECTRON- MeV-Sr
ELECTRON ENERGY (MeV)
0.8
0.6
0.4
0.2
0
0.2
0.4
0.6
0.8
1.0

FIGURE 45

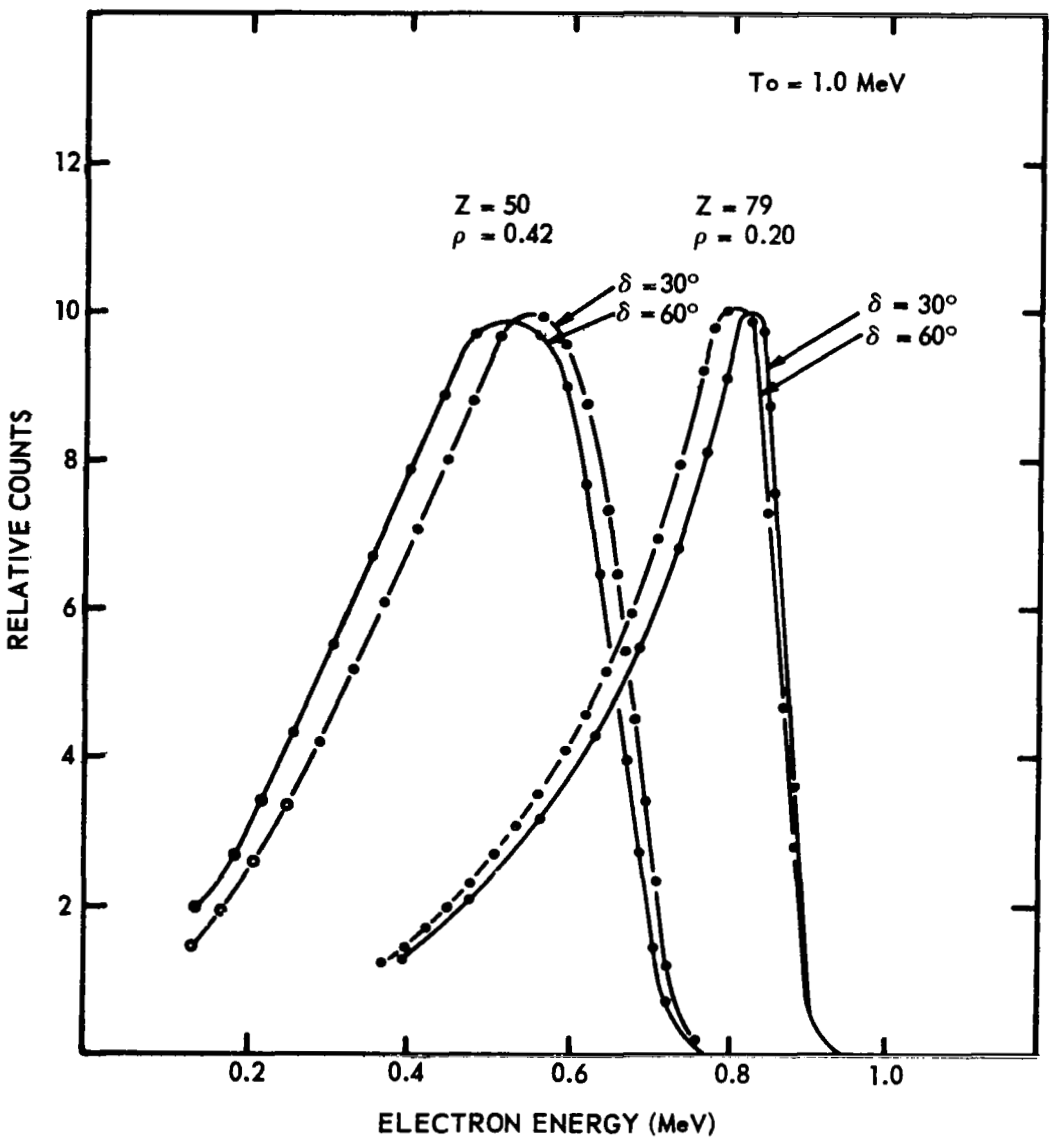
To = 1.0 MeV
Z = 50
ρ = 0.42
Z = 79
ρ = 0.20
δ = 30°
δ = 60°
δ = 30°
δ = 60°
RELATIVE COUNTS
ELECTRON ENERGY (MeV)
2
4
6
8
10
12
0.2
0.4
0.6
0.8
1.0

FIGURE 46

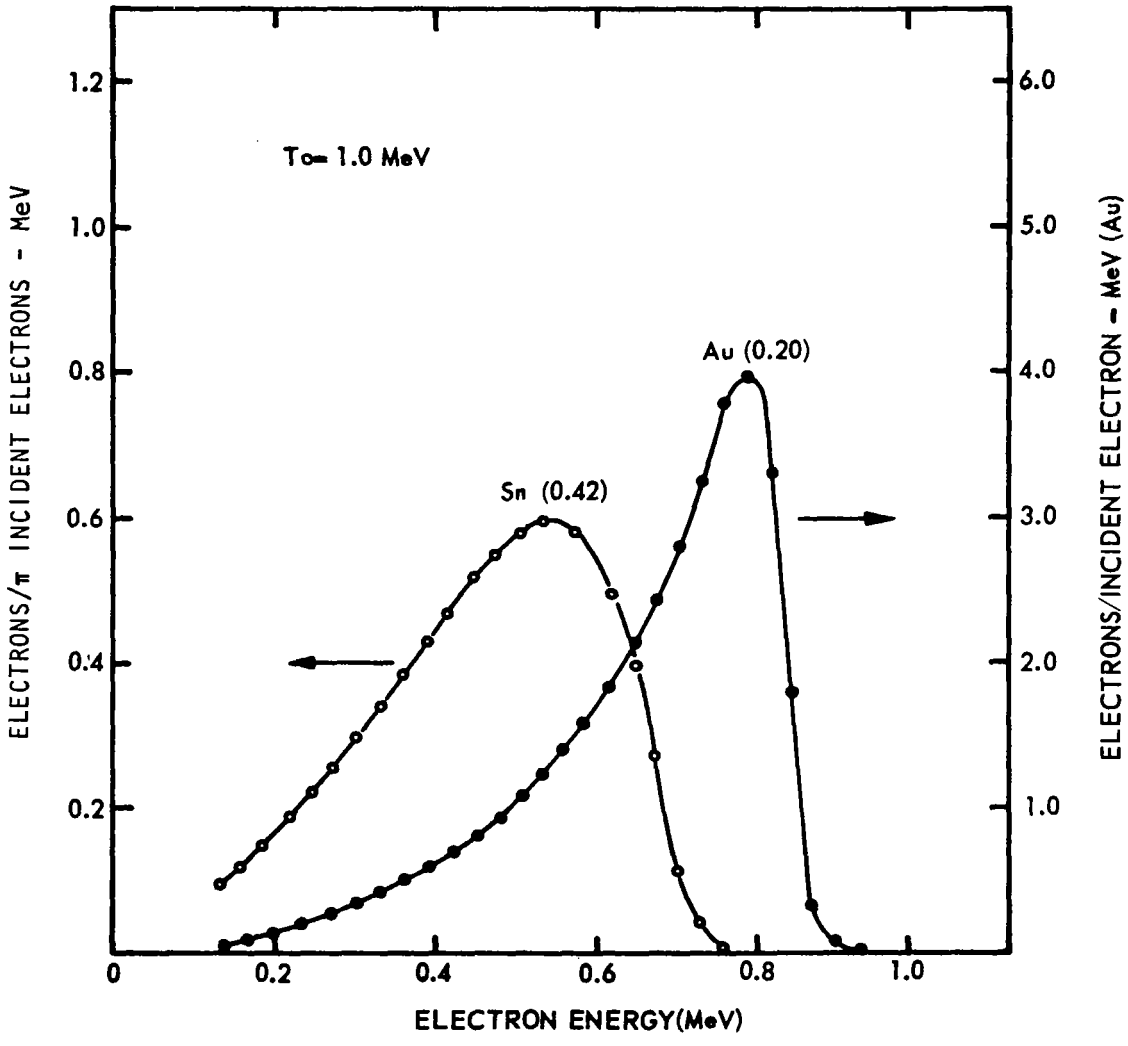
Tc= 1.0 MeV
Au (0.20)
Sn (0.42)
ELECTRONS/π INCIDENT ELECTRONS - MeV
ELECTRONS/INCIDENT ELECTRON - MeV (Au)
ELECTRON ENERGY(MeV)
1.2
1.0
0.8
0.6
0.4
0.2
0
0.2
0.4
0.6
0.8
1.0
6.0
5.0
4.0
3.0
2.0
1.0

FIGURE 47

ACKNOWLEDGMENTS

The author would like to acknowledge the assistance of Mr. W. J. Rainwater, Jr. in analyzing the electron spectra of this report and of Mr. A. Ruiz in operating the Van de Graaff facility during the accumulation of the data.

NASA-Langley, 1967 —— 24 CR-1383